Technologies for Multiphoton 3D Endomicroscopy Using MEMS Scanners

by

Mayur Bhushan Birla

A dissertation submitted in partial fulfillment
of the requirements for the degree of
Doctor of Philosophy
(Mechanical Engineering)
The University of Michigan
2021

Doctoral Committee:

Professor Kenn R. Oldham, Chair
Professor Karl Grosh
Professor Katsuo Kurabayashi
Professor Thomas D. Wang

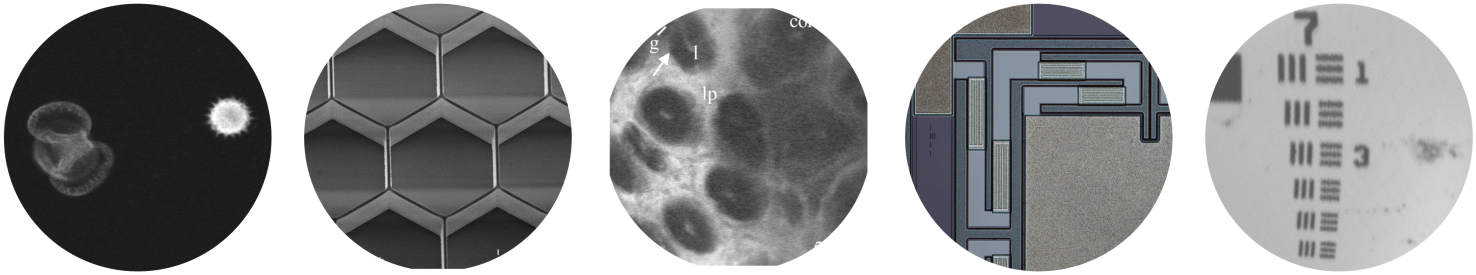

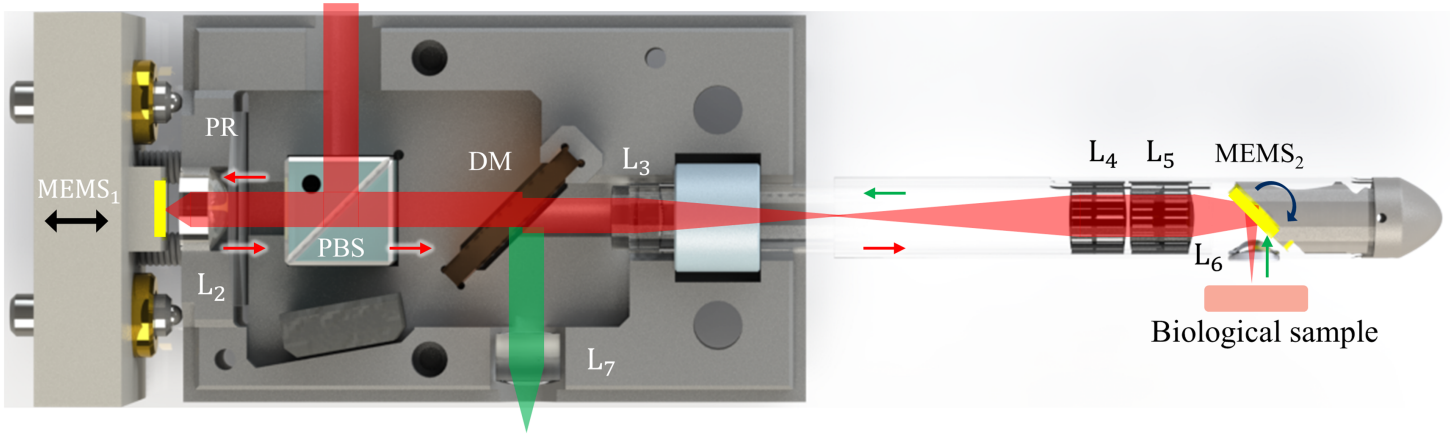
PR
DM
L_3
L_4
L_5
$MEMS_2$
$MEMS_1$
PBS
L_2
L_6
L_7
Biological sample

Mayur Bhushan Birla

mbirla@umich.edu

ORCID iD: 0000-0003-4687-6422

To humanity and beyond

ACKNOWLEDGEMENTS

I am grateful to my advisor Prof. Kenn R. Oldham for giving me the opportunity to work on the multiphoton endomicroscopy project. He has been a constant source of encouragement, motivation, guidance and I am thankful to him for supporting me in academic and personal ups and downs. I am thankful to our collaborator Prof. Thomas D. Wang for letting me work in his laboratories and providing valuable resources necessary for the success of this work. I would like to thank my other committee members Professor Karl Grosh and Professor Katsuo Kurbayashi for being on my committee and providing valuable feedback on my dissertation. It's been my privilege that Professor Oldham was my advisor and I learned a lot from him.

I am grateful to the National Institute of Health (NIH) for funding this project. I am also thankful to the Mechanical Engineering department for providing GSI opportunities and ensuring continuous funding.

I would like to thank my labmates from Prof. Oldham's group, Dr. Jongsoo Choi, Dr. Kendall Teichert, Dr. Jinhong Qu, Dr. Yi Chen, Dr. Lu Wang, Joonyoung Yu, Tayebeh, Zahra Afkhami, Ketul Patel, Ki Lee, Jiajie Qui, Jiwen Chen, and collaborators from Prof. Wang's group, Dr. Xiyu Duan, Miki Lee, Dr. Haijun Li, Tse-Shaoo, Ahmad, Tong Li, Dr. Gaoming Li, Ruoliu, Dr. Sangeeta Jaiswal, and bioteam members, for constructive technical discussions, and their support during my time at UM. Special thanks to Prof.Najafi's group and Dr. Sajal Singh for letting me borrow various instruments and having valuable brainstorming discussions.

Special thanks to Dr. Jongsoo Choi for training me on various micro-fabrication processes and providing valuable insights. I also thank staff and members of the Lurie Nanofabrication Facility at the University of Michigan for providing support during the fabrication and characterization of devices. I thank Prof. Evgueni Filipov and his group members Yi Zhu and Maria Redoutey for providing me an opportunity to collaborate on fascinating micro-origami projects.

I am grateful to my Ann Arbor friends Rohan, Anish, Nidhi, Pallav, Pooja, Sharang, Geethakrishna, Isha, Rohith, Nelson, Shruti, Amol,Sajal, Bikash, Neeharika, Karthik, Pratyush, Shiva, and Pranav for beautiful memories, fun times, cultural fes-

tival celebrations, and nostalgic trips around the US. I would especially like to thank Rohan for helping me settle in the United States during the initial time of my Ph.D. My distant relatives settled in Michigan made me feel like a family member and home in Michigan. I would like to thank Anish and Pallav for making me look forward to Friday nights and making them nostalgic which I would miss for life.

I would like to thank my childhood friend Nirav, and undergraduate friends Chirayu, Avinash, Bhavik, Sashank, Nikhil, Jaydeep, Shreya, who are/were in Michigan, for their help. I would cherish the beautiful memories of the time I spent with them.

I would like to thank my family and in-laws for always being there for me. My achievements wouldn't have been possible without enormous sacrifices by my parents and brother Sanjog at multiple levels to help me pursue my dreams and motivating, encouraging me in every step of my life. They have been my support pillars. Special thanks to my wife who left her job in India and came to the US to join me. She played a major role in supporting me during my Ph.D. My nephew Avyukt always brought happiness to me and even after the craziest day talking to him felt like mediation to me.

I thank all those whom I may have missed and who contributed directly or indirectly to the success of this dissertation.

TABLE OF CONTENTS

LIST OF FIGURES

Figure

LIST OF TABLES

Table

LIST OF APPENDICES

Appendix

ABSTRACT

Conventional endoscopic white light imaging permits acquisition of images only on the surface of biological tissue (XY-plane). These endoscopes lack the capability to take microscopic images within the epithelial layer, a thin layer of tissue that lines the outer or inner surface of hollow organs such as the colon. Moreover, it can be very advantageous to capture subcellular images of the vertical cross section (XZ- or YZ-plane) of the epithelial layer. Such subcellular images can offer insight about disease such as cancer in early stages of its development. A variety of laser-based imaging techniques such as confocal, multi-photon, and optical coherence tomography (OCT) have been developed which can acquire images at varying depths in optically thick biological samples with sub-cellular resolution. The multi-photon imaging technique has high spatial resolution and can be used to image either fluorescent biomarkers or certain endogenous fluorescent cells at depths of up to several hundred micrometers. These imaging modalities are single pixel imaging techniques and require a single or multiple scanners to steer the focal point in the lateral and/or axial directions. MEMS scanners are potentially well-suited to perform 3D laser focal point steering given stringent constraints on space in a typical endomicroscopy system.

A vertical cross section image can be acquired either by (a) stacking multiple XY images at different depths and reconstructing an XZ image along a line in the stacked images or (b) directly imaging along the XZ plane. The former method is slow and time consuming and often suffers from motion artifacts leading to poor imaging resolution. Direct imaging along the XZ plane is preferred, but to do this in an endoscopic imaging system, it is necessary to perform axial (Z-axis) translational scanning of the focal point of an ultra-fast laser, preferably at or near the distal optics of the endoscope.

Among a variety of transduction mechanisms, electrothermal scanners have demonstrated the largest total displacements and operate at low voltage, but are typically limited in speed by thermal response time and the amount of heat that can rapidly be dissipated in a small instrument. Electrothermal axial scanning can be complemented by other high-frequency scanning mirrors for full 2D- or 3D- imaging. Various beam steering patterns, such as raster, spiral, and Lissajous, can then be chosen depending

on the application and scanning actuator capabilities. Lissajous scanning is a popular choice in imaging applications as it can be easily implemented, and, unlike raster scanning, it does not require operating frequencies to be widely separated, simplifying MEMS design for multi-axis scanners. However, the resonant frequency of a scanner can drift by several degrees of phase angle due to environmental perturbations. This drift, in turn, produces a change in phase delay between mirror motion and the periodic input driving signal, adversely affecting the image quality.

In this work, we present (i) an electrothermal scanning micro-mirror design with an unusually short thermal time constant that enhances dynamic operation near resonance; (ii) an algorithm for high-accuracy mechanical phase estimation using an image based sharpness and blur metric; (iii) a two-photon 3D endomicroscopy instrument for imaging in small animals .

The electrothermal scanner uses a lattice-like honeycombed shaped silicon-dioxide support structure that results in extremely small mirror mass, both inertial and from a thermal capacity standpoint, with little increase in mirror curvature. The novel support structure also makes the complete mirror area usable which is often not possible in the design that relies on isotropic silicon etching to release the device. Though the actuator does not achieve the full range of displacement that has been previously demonstrated by electrothermal mirrors, it features an unusually short thermal time constant that enhances dynamic operation near resonance. We demonstrate sample 3D multi-photon images of pollen grains taken at varying depths by scanning the electrothermal mirror in a benchtop imaging system. We compare these images with the images taken by moving the specimen and holding the electrothermal scanner stationary.

We demonstrate an image sharpness-based variance metric and blur-based threshold metric are well-suited to the compensation of unknown phase perturbations in Lissajous scanning with MEMS mirrors, with some trade-offs between them for robustness of parameter selection versus computational efficiency. In addition, we will discuss how these phase estimation algorithms interact with other potential limitations of Lissajous scan design, such as fill factor versus frame rate and non-uniform scan density, and will suggest practical approaches for managing these trade-offs for the MEMS scanner. Sample images from a fluorescent confocal endomicroscope using a 2-axis parametrically-resonant micro-mirror are presented.

Motivated by the promising results from the benchtop system, we developed handheld two-photon 3D endomicroscope for small animal models of disease. Ray-trace simulations were performed to optimize the system performance and making design

trade-offs during the process. A robust mechanical design was developed for easy alignment and packaging of optical elements, and minimizing the effect of dimensional and alignment tolerance. We then verify the performance of packaged distal probe by capturing confocal reflectance images. Sample two-photon images taken using the miniature freespace coupled instrument is then presented. Finally, we discuss potential methods to increase the versatility of the instruments, for instance, integrating a fiber for light delivery into the probe.

CHAPTER I

Introduction

The overall aim of this study is to develop a multi-photon 3D imaging system capable of in-vivo cross-section imaging of thin epithelial tissue in a small animal like a mouse, and associated enabling technologies for small endomicroscopes.

1.1 Colorectal cancer

As per the American Cancer Society, colorectal cancer (CRC) is the fourth most common cancer in both males and females, with an incident rate of 39.3 (per 100,000 age-standardized population) for the years 2011-2015. The mortality rate of CRC has declined from 29 to 14.2 from the year 1980 to 2016 [1]. Zauber et al. in their study attributed 50% of the decline in the CRC mortality rate to an increase in CRC screening rate [2]. When CRC is found before it has spread outside the colon or rectum the survival rate is 90%, however, only 40% of cases are detected at this early stage of cancer. Some of the undetected cases can be attributed to the limitation of screening techniques. Thus, there is a scope to improve screening techniques in hollow organs like the colon.

The epithelial layer is a thin layer (typically 0.4-0.5 mm thick) of tissue that lines the outer or inner surface of hollow organs such as the colon. Many diseases, including cancer, originate in this layer of tissue and there is a need to develop high resolution, high frame-rate, in-vivo imaging techniques paving way for not only early stage cancer detection, but enabling sub-cellular resolution to study changes in tissue morphology, study the effects of drugs and treatment at a cellular level, etc.

1.2 Endomicroscope as a screening tool

The decline of 50% in the CRC mortality rate due to increased CRC screening rate [2] could be further improved with a point-of-care technique like endomicroscopy.

Conventional white light reflectance endoscopy is good at detecting well-developed lesions and polyps. However, it lacks the ability to distinguish between pre-cancerous and benign lesions [3], and often misses flat lesions. Real-time in-vivo imaging with sub-cellular resolution offers rapid diagnosis, increased affordability, and could eliminate biopsies that are often taken from multiple sites, more than required. Recently, a variety of instruments with a sub-cellular resolution capable of early detection of pre-cancerous tissue have been developed [4], [5]. However, these instruments are not compatible with thinner clinical endoscopes whose working channels are now 2.8 mm in diameter. MEMS scanners enable packaging in a compact footprint and have the potential to become a true point-of-care endomicroscopy technology [6]. However, a multi-axis MEMS scanner which sit at the heart of an endomicroscope often suffers from dynamic perturbations causing phase delays due to environmental changes during in-vivo imaging. The perturbations in motion dynamics lead to blurred images adversely affecting the image resolution. Already space-constrained applications like endomicroscopy can't afford space for on-chip sensing or temperature compensation mechanisms to correct for the dynamics changes. As one task in this dissertation research, we attempt to estimate the phase delays in a multi-axis scanner using an image processing approach which doesn't require any additional hardware to improve planar imaging during endomicroscopy.

1.3 Endomicroscope as a scientific tool

In addition to development of commercial screening instruments, there has been growing interest in developing endomicroscopy systems as scientific tools for in-vivo imaging in small animals like mice. Mice are widely used in scientific research due to the availability of a variety of mouse models resembling humans genetically and physiologically. Also, mice are easy to breed, grow, maintain, and have a short lifespan reducing the experiment cycle time. A well-designed endomicroscope for in-vivo imaging in mouse could be used in assessing drug efficacy [7] and study transient effects due to drug-inducing agents [8]. Early-stage disease development could be studied by investigating molecular changes that precede the morphological changes in tissue. In-vivo assessment of the targeted biomarkers expressed within a tissue plays a vital role in such studies. An imaging modality capable of targeted imaging is well suited for this application. A major goal of this dissertation research is to develop such a miniature hand-held system capable of targeted multi-photon 3D imaging in small animals.

1.4 Need for vertical-cross section or 3D imaging system

In humans or animal models, a normal tissue first develops the pre-malignant condition, dysplasia, before growing into a malignant polyp, or carcinoma. The dysplasia can be detected by observing the morphological changes in the epithelium through histology. These morphological changes take place within the tissue layer before proceeding to the tissue surface. Thus, histology images along a plane perpendicular to the tissue surface (vertical cross-section) provide early insights into disease progression. The existing screening method of taking biopsies from potential disease sites is likely to miss flat lesions or non-protruding polyps leading to false-negative reports. Recent advancement in endomicroscopy has made it possible to collect histology-like in-vivo images, but most of these instruments image in a plane parallel to tissue surface [9]–[20]. There is a need to develop instruments that can directly image in a vertical plane or acquire 3D images of tissue samples. A variety of imaging modalities such as magnetic resonance imaging, ultrasound, confocal, etc., provide opportunities to such perform deep tissue imaging. The following section provides a brief overview of these modalities.

1.5 Non-invasive deep tissue imaging modalities

1.5.1 Magnetic Resonance Imaging (MRI)

MRI is based on the nuclear magnetic resonance (NMR) phenomenon and it can capture three-dimensional images of the internal structure of a biological subject. In MRI, the object to be imaged develops magnetization upon being placed in a strong DC magnetic field which may have a predetermined magnetic field gradient. The voltage signal is received by the sensing coils on the application of a rotating radio frequency magnetic field which temporally tips the magnetization in a plane perpendicular to the original DC magnetic field. Researchers have achieved resolution as small as 150 µm, isotropic, while imaging the entire human brain at a magnetic field as high as 7 T [21]. Yet this resolution is a couple of orders of magnitude inferior to sub-cellular resolution. MRI has excellent penetration depth, but it is a slow and low-resolution imaging modality not suitable for the real-time endomicroscopy applications.

1.5.2 X-ray Computed Tomography (CT)

In an X-ray CT scan, projection X-ray signal is recorded from multiple angles and a computerized algorithm is used to generate the cross-section slice of the sample. Using a CT scan one can take an interior image of an object without cutting it. CT scan has excellent penetration depth as X-ray can pass through biological objects like tissues and bones and interacts with them sufficiently for imaging. Contemporary CT scanners have a spatial resolution ranging between 0.3-0.6 mm along all three dimensions [22]. The advancement in CT scanner technology including the dual-source CT has increased the temporal resolution paving the way for real-time imaging, however, this imaging modality is still not suitable for sub-cellular deep tissue imaging due to limited spatial resolution.

1.5.3 Ultrasound

Ultrasound, also known as sonography, is a real-time imaging technique and widely used in medical imaging to visualize the internal organs. A short pulse of sound at ultrasonic frequency (frequency higher than the human audible range) is passed through a biological sample and a pulse-echo is recorded. The time delay in the received signal provides the depth information while the image contrast comes from different reflection properties in the imaging sample. Ultrasound can easily image several inches deep inside the biological sample. The signal attenuation increases with an increase in sound frequency. One can use low frequency to image deeper, however, the axial resolution gets worse at low frequency. The signal can't be increased beyond a certain point as peak pulse power is limited by cavitation and tissue heating. The lateral resolution depends on the frequency and aperture of the array of the transducer. A high-resolution ultrasound biomicroscopy (UBM) technique has been developed recently with a lateral and axial resolution of 60 µm and 30 µm [23]. Overall, the spatial resolution is still not enough for the sub-cellular resolution needed for endomicroscopy.

1.5.4 Photoacoustic

In photoacoustic imaging a biological sample is illuminated with a pulse laser. A fraction of the incident light energy is converted to heat through the non-radiative decay process inside the sample. Due to the thermoelastic effect, the heat expands and contracts the tissue producing ultrasound waves. A transducer is used to sense and construct the image by the ultrasound waves so generated. Various physiological properties dictate the optical absorption, thereby producing sound waves at different

Table 1.1: Qualitative comparison of typical spatial resolution in bio-medical imaging modalities

Imaging modality	Speed	Spatial resolution		Imaging depth	Targeted imaging
		Axial	Lateral		
MRI [27]	slowest	1-2 mm	1-2 mm	Excellent	Yes
X-ray CT [27]	slow	0.5 mm	0.5 mm	Excellent	limited
Ultrasound	real time	50 µm	100 µm	Good (>10 mm)	limited
Photoacoustic	real time	3 µm	100 µm	Poor (<1 mm)	limited
Optical*	real time	3 µm	1 µm	Poor (<1 mm)	Yes

*excluding super-resolution techniques

intensity providing contrast in the image. The penetration depth is on the order of <1 mm and limited by optical scattering in the tissue. The lateral resolution is determined by the acoustic signal similar to ultrasound imaging, whereas the axial resolution depends on the optical focal volume [24]. In general axial resolution is an order of magnitude smaller than lateral resolution. The frame rate depends on the SNR, however, researchers have demonstrated real-time imaging at 50 Hz with a reasonable image quality [25].

1.5.5 Optical

Optical imaging is the most conventional form of imaging where light (ultraviolet to near-infrared) is used to image the biological sample. Various optical imaging modalities have been developed such as wide-field, confocal, dual axes, multi-photon, etc., but still, this is an active area of research. Optical images offer the highest possible resolution among any other modality and carefully engineered instruments are often diffraction limited. Recently, researchers have developed super-resolution imaging with numerous variations that beats the fundamental limit of resolution (diffraction-limited). A typical resolution of 50 nm is achieved with commercial stimulated emission depletion microscopy, and advance labs can go much smaller [26]. In optical imaging longer wavelengths (near-infrared) are used for deeper penetration, however, the signal attenuates rapidly beyond 1 mm depth. Optical imaging techniques are real-time and safe as they don't use an ionized beam, unlike CT scans.

1.5.5.1 Widefield

Widefield microscopy is the conventional imaging technique in which the entire field of view on the specimen is illuminated and the image is seen through the eyepiece or recorded using a camera. The image can be rendered from either the reflected light or fluorescence light emitted by the sample upon illumination.

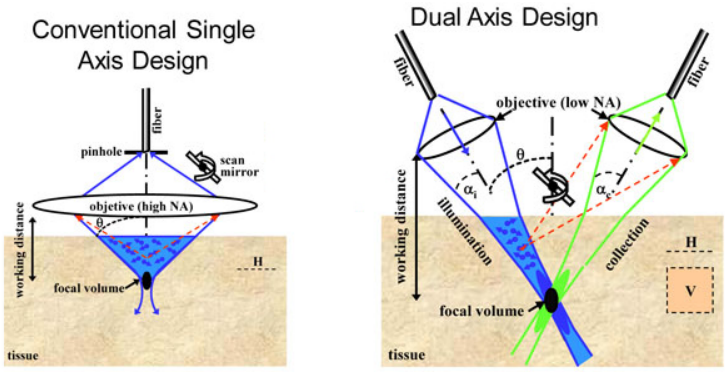

Figure 1.1: Confocal imaging: single and dual axis configuration

1.5.5.2 Confocal

In confocal microscopy, a small volume of the specimen is illuminated using a laser light source. The emitted light is passed through a pinhole to eliminate any signal that originates outside of the focal volume. An image can be constructed by scanning the focal point on the specimen and recording the signal point by point. This imaging technique is comparatively slow as light intensity corresponding to each pixel is recorded one by one as opposed to conventional widefield where all pixels are captured at the same time. The image resolution is directly proportional to objective lens NA. Factors that increase lens NA, such as large aperture or short focal length, increase the image resolution.

Confocal microscopy is used in two popular configurations, single-axis, and dual-axis as shown in the fig 1.1. In single-axis, light is illuminated and collected from the same fiber which is placed normal to specimen surface and the fiber core diameter acts as a pinhole. In single-axis, the penetration depth is reduced by using higher NA to get high resolution, for a fixed wavelength, and lens diameter. In dual-axis, the illumination and collection paths are placed at an angle as shown in fig. 1.1. A smaller NA lens can produce high-resolution images by reducing the overlapping focal volume. However, aligning the light paths to make them intersect at the focal point is challenging.

1.5.5.3 Two-photon

In this imaging technique, two photons of a longer wavelength are absorbed by the specimen and a fluorescence signal at a shorter wavelength is emitted. The optical transition probability from the ground state to a high energy state is proportional to the square of the light intensity in the two-photon absorption phenomenon. At

very high intensity, the two-photon effect dominates the linear absorption. Such a high intensity can be achieved by focusing light, both spatially and temporally, in a small volume using high NA objective and ultra-fast high-power femtosecond laser. As a consequence, a fluorescence signal is generated only from a tight focal spot reducing scattering and photobleaching compared to confocal imaging. This substantially reduces the background noise and longer wavelength excitation enables greater penetration depth and improved SNR [28]. Recently, Kobat *et al.* captured in-vivo images in mouse cortex up to 1.6 mm deep [29]. Despite numerous advantages, multi-photon microscopy requires a large and expensive high power laser limiting its ability for system-level miniaturization and affordability.

1.5.5.4 Optical coherence tomography (OCT)

In OCT, a low coherence light is split into two beams where one beam is used for sample illumination and the other acts as a reference. The reflected light from the sample is then combined with the reference beam forming an interference pattern detected using a light sensor (camera). The light will form interference patterns only if the difference in the distance traveled by both is beams is less than the coherence length. The coherence length is usually chosen in micrometers so that light undergoing multiple scattering will not contribute to the interference pattern. The imaging is limited to 1-2 mm below the tissue surface as beyond that scattering is prominent [30]. The resolution is lower than other optical imaging techniques such as confocal, dual axes, and multiphoton. Miniaturization of OCT to make it compatible with endoscope channels is challenging due to the bulky interferometer, and limited by the resolution [31]

1.6 MEMS scanners in miniaturized endomicroscopy

Among the medical imaging modalities discussed above, optical imaging is a popular choice for deep tissue imaging of hollow organs, such as the colon, because it offers the best spatial resolution and because a wide selection of biomarkers responding to optical stimulus are available for targeted imaging. Miniaturization of endoscopy systems based on optical imaging requires a compact scanning mechanism to move the focal point of a laser through tissue. A scanning mechanism can be placed at the distal (away from a user) and/or proximal location (near a user) depending on optics, instrument requirements such as side view or front view, field of view, and packaging constraints. A variety of devices such as galvo mirrors, fiber scanning using

a piezo-tube or piezo-strips, and MEMS scanners have been developed for focal point steering. For instance, a commercially available endomicroscopy system, Cellvizio by Mauna Kea Technologies, consists of a fiber bundle and a scanner placed at its proximal end enabling recording of fluorescence signal from individual fibers in the bundle. Researchers also developed miniature probes in various configurations using MEMS scanners, or fiber scanning using piezo-tubes/strips [9]–[20].

MEMS scanners are well suited for endomicroscopy as they offer substantical flexibility relative to other mechanisms. MEMS scanners are easy to customize, possess multi-axes scanning capability, and can be designed to have a large bandwidth for high frame rate applications. Moreover, MEMS devices are reliable, consume low power, and are affordable due to batch production. These scanners operate on a number of transduction methods such as electrostatic, electrothermal, electromagnetic, and piezoelectric. A brief overview of these methods and their relative advantages and disadvantages is provided below.

1.6.1 Electrothermal

Electrothermal actuators, as their name suggests, are based on the electrical and thermal physical domains. Electrical current (I) is passed through the actuators by applying a suitable voltage (V), causing Joule heating (P) due to electrical resistance of the actuator structure. The heating causes thermal expansion of the actuator beams according to eq. (1.2). There are various configurations through which the thermal expansion of beams can be used in achieving translational or rotational displacement along different axes. For instance, U-shaped actuators shown in fig. 1.2(b) have two legs with the same length, but one leg is made wider than other resulting in different effective resistance of each leg. On passing current, the narrower leg heats up more due to its higher resistance compared to the wider leg, and thus expands more. This produces net lateral displacement. In bimorph actuators fig. 1.2(a), two layers of materials have a widely different co-efficient of thermal expansion and upon heating these layers expand differently, leading to curling towards the material with lower thermal expansion coefficient. There are also V-shaped structures (fig. 1.2(c)) which take advantage of thermal expansion of hot beams to produce net displacement.

$$P = I^2R = VI \tag{1.1}$$

$$\Delta L = \alpha L \Delta T \tag{1.2}$$

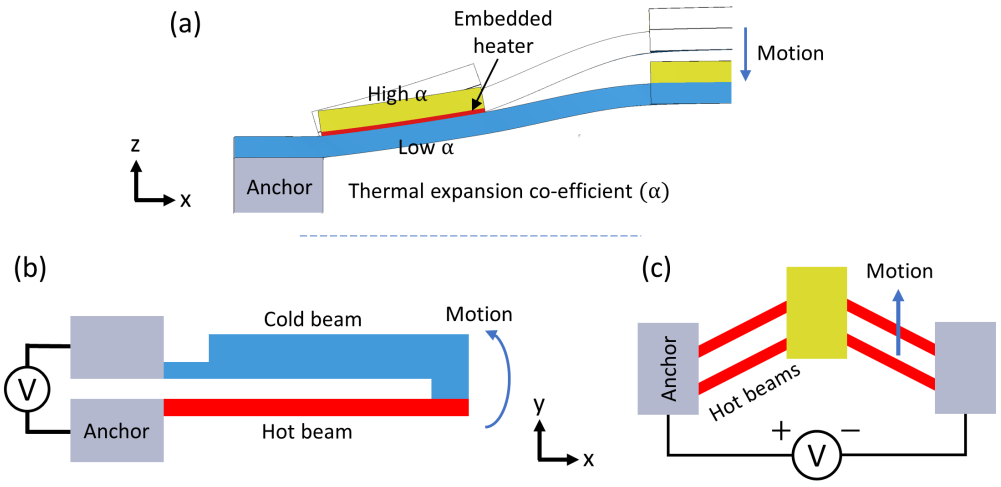

Figure 1.2: Types of MEMS electrothermal actuators and their working principle

Advantages and disadvantages: Electrothermal actuators are easy to fabricate, can produce large forces and large displacement. However, the power requirement of electrothermal devices is large (typically >100 mW) and most of the input power is used in joule heating which is dissipated to the surroundings. In some temperature sensitive applications, heat dissipation itself could lead to undesired temperature fluctuations in the surroundings. The electrothermal actuators are also slow as the time response of the actuation mechanism is governed by the speed of heat dissipation which is typically on the order of tens of milliseconds in MEMS devices [32]–[34]. In applications requiring vacuum packaging, for instance, to achieve high quality factor by reducing the viscous damping by air, heat can't be dissipated by convection making the actuators slower. In such cases, there is a trade-off between high quality factor and high speed.

1.6.2 Electrostatic

Electrostatic actuators are based on the force of attraction between two conductors separated by a distance and held at different electric potentials. The most common configuration is when two flat conductors are placed parallel to one another forming a capacitor, with one conductor held stationary (fixed) and other free to move. The energy stored in the capacitor as a function of its configuration is given by [35]

$$E(\eta) = \frac{1}{2}C(\eta)V^2, \tag{1.3}$$

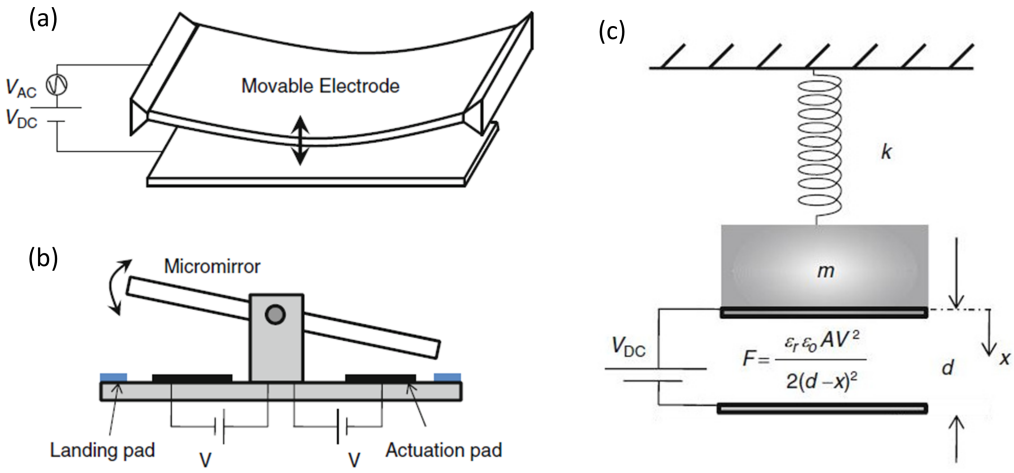

Figure 1.3: (a) out of plane translation motion, (b) in-plane rotational motion achieved using electrostatic base actuation. (c) Simple lumped mechanical model for base actuation (Figures credits: [35]).

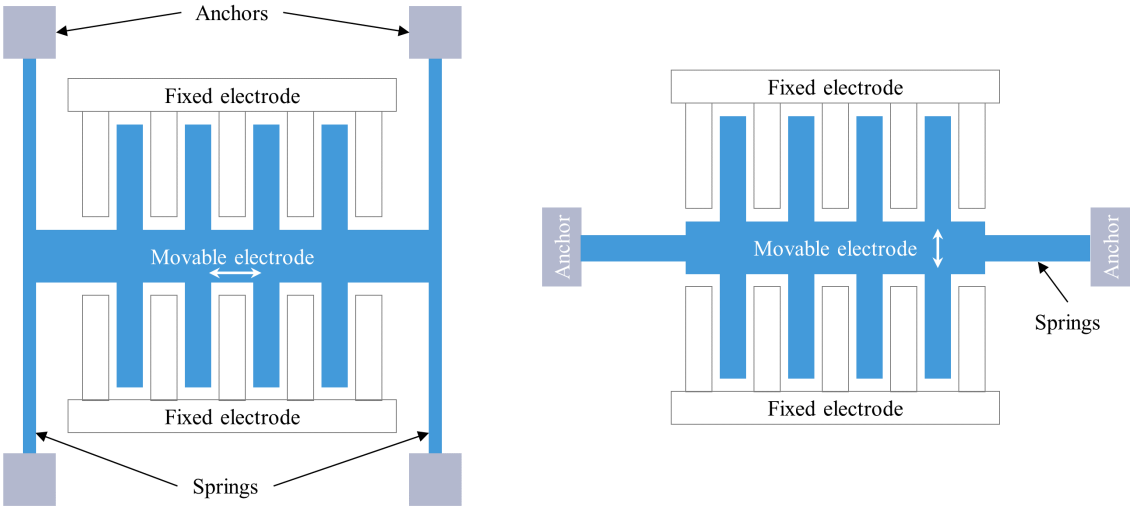

Figure 1.4: Electrostatic actuation using comb drive.

where, η represents spatial degree of freedom depending on the capacitor's configuration, C is capacitance and V is electric potential difference between the two conductors. The magnitude of attractive force is given by

$$F = \frac{-\partial E(\eta)}{\partial \eta} = \frac{1}{2}\frac{\partial C(\eta)}{\partial \eta}V^2. \tag{1.4}$$

The electrostatic force is always attractive, and the direction of force is towards the other electrode. The above equation is a lumped model version and for more sophisticated geometries a standard FEA package can be used to calculate force. The electrostatic actuators can be further classified in two broad categories namely, a) base, and b) comb drive actuation.

a) In this type, the movable electrode is fixed to a stationary electrode via a compliant structure usually made up of slender beams. These beams act often act as a spring and the expression for force of attraction obtained by the lumped model is shown in fig. 1.3(c). An out-of-plane translational motion or in-plane rotational motion can be achieved by exploiting different spring and electrode arrangements as shown in fig. 1.3.

b) In this type, there are two comb-shaped, interdigitated electrodes as shown in fig. 1.4 with one fixed and other moveable and supported using compliant structures. In most of these applications, the movable electrode is displaced in any of the in-plane directions using electrostatic forces to obtain in-plane translation and/or out-of-plane rotational motion. However, researchers have also demonstrated in-plane rotational, and out-of-plane translational devices [36], [37].

Advantages and disadvantages: Electrostatic actuators are easy to fabricate, can be actuated at high frequency, and are best suited for low power applications. The actuators can also be structurally robust and can produce large displacements if actuated near mechanical resonance. However, achieving a large displacement in DC mode is yet challenging and often limited by the pull-in phenomenon. These actuators require large actuation voltage (>30V) and suffer from a non-linear relationship between the displacement and input voltage as evident from equation shown in fig. 1.3(c).

1.6.3 Piezoelectric

Piezoelectricity was first reported by Pierre and Jacques Curie [38] and the term piezoelectricity was later coined after the discovery, where suffix *piezo* in Greek means

'to press'. The direct piezoelectric effect is a phenomenon of producing electric charge on the surface of a poled piezoelectric ceramic when it is mechanically strained (or stressed). Conversely, on application of electric field the piezoelectric material develops electric polarization and becomes mechanically strained. This converse piezoelectric effect was predicted by Lippmann in 1881 from fundamental laws of thermodynamics [39].

Lead-zirconate-titanate (PZT) is a widely used piezoelectric material in MEMS actuators as it shows strong coupling between electrical and mechanical domain. Actuators based on bulk and thin-film PZT have been developed in the past [40], [41]. Of these, thin-film PZT-based actuators can achieve larger displacement with relatively small actuation voltage owing to large piezoelectric strain constants (d31, d33) and high electric fields. For instance, the thin-film PZT will develop a compressive strain when external voltage is applied along the poling direction (axis 3). In MEMS devices, PZT material is rarely used stand-alone and is usually put on a compliant structure such as beam or membrane. The thickness of different layers is adjusted to ensure that the neutral axis is away from the midplane of the PZT. By wisely engineering the actuator beams one can achieve motion along different axes such as in-plane rotation and/or out-of-plane translation.

Advantages and disadvantages: Thin-film PZT-based actuators achieve large displacement both in DC and resonant mode with very low power input. To do so, a compliant structure is needed, making the actuators less robust. PZT is brittle, being a ceramic material, and extra care is required during handling. The fabrication process is complex as it involves more lithography masks compared to electrostatic devices. As PZT ceases to be a piezoelectric material above Curie temperature, it faces limits in high temperature applications.

1.6.4 Electromagnetic

In electromagnetic actuation, a magnetic field is manipulated using electricity, in contrast to magnetic actuation where permanent magnets or electromagnets are used to obtain motion. MEMS electromagnetic actuators takes advantage of Lorentz force as described by (1.5) to maneuver the actuators

$$F = qE + qv \times B \tag{1.5}$$

where, F is Lorentz force, E is electric field, q is electric charge, v is velocity of electric charge, and B is strength of magnetic field. There are two ways by which

these actuators can be realized:

a) A ferromagnetic material is deposited on a compliant structure and an external magnetic field that can be varied is used to move the actuator

b) A compliant structure is deposited with thin wires and placed in an external magnetic field (usually permanent). A desired motion is achieved by changing the current amplitude and direction.

Advantages and disadvantages: Electromagnetic actuators have intermediate fabrication complexity and can achieve large displacement and force (and moments) with low voltage. However, they may consume more power when the magnetic field is created using electric current. In other cases, they require a bulky external magnets or coils, limiting their use in space constraint applications.

Table 1.2: Comparison of large displacement MEMS scanners with different working principles

Actuation mechanism	Electrostatic	Electrothermal	Piezoelectric	Electromagnetic
Reference	[36], [37]	[33], [42]	[40], [41]	[43], [44]
Fabrication	Simple	Simple	Complex	Intermediate
Integration complexity	Easy	Moderate*	Easy	Complex**
Robustness	Robust	Delicate	Delicate	Robust
Operation mode	Resonant	Resonant/DC	Resonant/DC	Resonant/DC
Bandwidth	High	<200 Hz	>1 kHz	>1 kHz
Voltage	High (>30 V)	Low	Low	Low
Power	Low	High	High	High
Cross-axis coupling	Low	moderate	moderate	moderate

* requires heat dissipation mechanism; ** requires external/internal magnetic field

1.7 Existing multi-photon in-vivo imaging systems

Numerous multi-photon endomicroscopy probes have been developed recently and summarized in the table 1.3. Most of the probes are designed to capture 2D images while two of them are capable of 3D imaging [20], [45]. The majority of these probes use either fiber (piezo tubes/strip) and MEMS scanners for 2D imaging. In all these works, the probe diameter is restricted to 10 mm, with one exception of 40 mm. The lateral FOV varies from 70 × 70 µm^2 to a maximum of 450 × 450 µm^2 for different probes. The maximum reported frame rate is 15 µm.

In the 3D imaging system, for instance, Dilipkumar *et al.*'s system [45] is free space coupled and uses an electrically tunable lens (ETL) for achieving axial scanning. The imaging speed of their prototype is limited by the response of ETL and the frame rate was less than 2 Hz. The overall prototype dimensions are big due to a bulky coupling objective lens. On the other hand, a piezo stage was used for axial scanning in Ang Li *et al.*'s prototype [20], making the overall footprint of the handheld part even larger.

Table 1.3: Summary of recently developed multi-photon endomicroscopy probes

Reference, year	Scanning mechanism Lateral	Axial	Probe OD (mm)	Resolution $\Delta x \times \Delta z$ (µm)	FOV (µm^2)	Frame rate (Hz)
[9], 2010	Piezo tube	no	2.8	1.5 × 9.2	150 × 150	1.1
[10], 2011	Piezo strips	no	3.0	0.8 × 10	110 × 110	4.1
[11], 2011	MEMS	no	9.6	1.27 × 13.5	130 × 100	7
[12], 2012	Piezo tube	no	2.0	0.69 × 6.15	110 × 110	2.7
[13], 2013	MEMS	no	3.0	1 × 24	70 × 70	N.R.
[14], 2013	MEMS	no	N.R.	0.6-2 × N.R.	178 × 280	34
[15], 2014	Piezo tube	no	3.5	0.67 × 3.1	100 × 100	N.R.
[16], 2015	MEMS	no	3.4	2 × 9	300 × 300	5-10
[17], 2015	Piezo tube	no	2.2	0.8 × 2	450 × 450	8
[18], 2016	MEMS	no	40	1.3 × N.R.	151 × 236	0.4
[19], 2016	Piezo strips	no	3.5	2.2 × 9.1	200 × 200	1.25
[20], 2017	Pizeo tube	no	2	0.7 × 6.5	N.R.	3
[46], 2018	MEMS	Piezo stage	1.75	0.83 × 6.1	120 × 120	10
[5], 2018	Piezo tube	no	5	2.2 × 12.7	400 × 400	15
[45], 2019	Galvo	ETL*	1.4	2.2-2.5 × 30-60	290 × 290	0.5-2
[47], 2019	Piezo tube	no	2.6	0.7 × 7.6	200 × 200	5
[48], 2020	Piezo tube	no	N.R.	0.6 × N.R.	300 × 300	6

*ETL - Electrically tunable lens

1.8 Specific aims & thesis overview

The overall goal of this research is to advance endomicroscopy techniques serving as both screening and scientific tools by solving associated problems with MEMS scanners and instrument operation. Ultimately, these techniques are to be integrated to develop a hand-held in-vivo imaging system enabling multi-photon 3D imaging of an epithelium layer of a colon tissue in a mouse model. The instrument should be capable of collecting images with a lateral FOV measuring 150x150 μm^2, and axial depth of up to 200 µm. The frame rate of lateral images should be more than 5 Hz and the size of handheld part less than 10 cm^3. Specific aims:

1. To design and develop a miniature hand-held multi-photon 3D imaging system for small animal in-vivo imaging.

2. To compensate the phase delays in a multi-axis scanner caused due to environmental perturbation during in-vivo imaging.

3. To develop a fast electrothermal scanner for proximal axial scanning in an endomicroscopy system.

4. To design and develop a piezoelectric scanner with reduced coupling between its degree of freedom.

Motivated by the discussions in this chapter, we first present a low thermal and inertial mass electrothermal scanner with increased bandwidth near resonance in chapter II. The reduced mass was achieved using a novel honeycombed shaped support structure in place of more conventional approach of using 20-40 µm thick solid silicon layer to minimize the curvature due to residual stress. These fast scanner are well suited for real-time endomicroscopy, due to low power consumption and large displacement. A sample multi-photon images of pollen grains on benchtop imaging system are presented.

In chapter III, we present piezoelectric MEMS scanner designed to minimize coupling between its various degrees of freedom. The design makes use of independent inner and outer actuation legs, anti-roll bar, and torsional spring to substantially reduce the coupling.

In chapter IV, we propose an algorithm to compensate for the phase delay in the compact multi-axis MEMS scanner using an image processing-based metric. We present a spatial variance metric and a threshold metric inspired from auto focusing

techniques, used here in compensating phase delay in single pixel imaging applications. We demonstrate a significant improvement in in-vivo images quality using this phase correction algorithm.

Chapter V first introduces an optical design for miniaturized handheld endomicroscopy instrument capable of taking 3D multi-photon. We then discuss the instrument assembly techniques to package the optical elements and MEMS scanner with high precision. Finally we demonstrate confocal reflectance images and a sample two-photon image taken using the handheld probe.

Chapter VI provides a summary of the research and briefly describes the future work.

CHAPTER II

Low Thermal and Inertial Mass Electrothermal MEMS Scanner

In this chapter, design and testing of a low-mass electrothermal vertical scanning mirror for fast axial scanning during multi-photon microscopy is presented. The mirror makes use of a novel honeycomb mechanical support structure to substantially reduce both thermal and inertial mass relative to mirror size. At the same time, undesirable mirror curvature due to residual thermal stress is controlled without adversely affecting the image quality. In addition, the support structure makes the complete mirror area usable which otherwise is not possible in devices that rely on isotropic silicon etching. A high actuator efficiency with static displacement per unit power of 2.08 µm/mW was achieved due to the reduced thermal capacitance at the actuator legs, when using a 700 nm thin structural layer of SiO_2. The resulting scanning mirror achieves open loop time constant as small as 3.42 ms with both thermal and mechanical bandwidths exceeding 100 Hz. Mirror surface non-idealities related to the mirror structure and their influence on image quality are discussed. Sample 3D multi-photon images captured by performing remote scanning in both lateral and axial direction on a benchtop testbed are presented. The efficacy of remote axial scan is ascertained by comparisons with images obtained by moving specimens relative to the objective.

2.1 Introduction

Conventional endoscopic white light imaging permits acquisition of images only on the surface of biological tissue (XY plane). These endoscopes lack the capability to take microscopic images within the epithelial layer, a thin layer of tissue that lines the outer or inner surface of hollow organs such as the colon. However, it can be very advantageous to capture sub-cellular images of the vertical cross section (referred to as the XZ- or YZ-plane in this paper) of the epithelial layer. Such sub-cellular images can offer insight about disease such as cancer in early stages of its development.

A variety of laser-based imaging techniques such as confocal [6], multi-photon [49], and optical coherence tomography (OCT) [50] have been developed which can acquire images at varying depths in optically thick biological samples. The multi-photon imaging technique has high spatial resolution and can be used to image either fluorescent biomarkers or certain endogenous fluorescent cells at depths of up to several hundred microns [51]. A vertical cross section image can be acquired either by a) stacking multiple XY images at different depths and reconstructing an XZ image along a line in the stacked images or b) directly imaging along the XZ plane. The former method is slow and time consuming and often suffers from motion artifacts leading to poor imaging resolution. Direct imaging along XZ plane is preferred, but to do this in an endoscopic multi-photon imaging system, it is necessary to perform axial (Z-axis) translational scanning of the focal point of an ultra-fast laser, preferably at or near the distal optics of the endoscope. MEMS scanners are potentially well-suited to perform this scanning due stringent constraints on space in a typical endomicroscopy system.

A variety of transduction mechanisms for MEMS scanners have been proposed for axial laser scanning in endomicroscopy, including electrostatic [36], piezoelectric [41], electromagnetic [44] and electrothermal [52] actuation. Among these, electrothermal scanning has demonstrated the largest total displacements and operates at low voltage, but is typically limited in speed by thermal response time and the amount of heat that can rapidly be dissipated in a small instrument. One way to increase the overall time constant (both thermal and mechanical) of the scanner is by reducing the mass of actuators and mirror. Typically, a micro-mirror is supported by a thick Si or other substrate layer to increase rigidity and improve mirror flatness [32], [33], [42], [53], [54]. Sometimes, the same Si layer is often retained under the passive sections of an actuator to leverage the displacement generated at the location of electromechanical transduction [32]–[34]. This further adds to thermal capacitance and a comparatively slow response time. In previous work, Zhang *et al.*[42] boosted the thermal response by using a composite layer of Cu/W/Cu at the leg instead of thick Si, however, the overall dynamic response was still limited by the mass of the mirror. Meanwhile, a strategy of reducing mirror mass typically results in a curved mirror surface due to residual stress and stress gradients induced in the layers of material during the fabrication process. The flatness of a mirror directly affects the image quality and thus there exist a trade-off between the scanner speed vs mirror flatness. In addition, in applications involving large mirror size, the requirements on both actuation speed and mirror flatness often do not scale proportionately, adding another dimension to

this trade-off.

In this paper, we present a scanning micro-mirror design that uses a lattice-like honeycombed shaped silicon-dioxide support structure that results in extremely small mirror mass, both inertial and from a thermal capacity standpoint, with little increase in mirror curvature. The novel support structure also makes the complete mirror area usable which is often not possible in the design that relies on isotropic Si etching to release the device [42]. Through finite element simulation we assess the efficacy of different support structures in reducing mirror curvature due to inevitable residual stress and stress gradients. We demonstrate the advantages of reducing the thermal capacitance both at the legs, and mirror using an equivalent electrical model. We also utilize a star configuration as an electrical circuit for connecting the four heaters, and discuss its advantages and disadvantages. We demonstrate 3D multi-photon imaging by remotely scanning in both lateral and axial directions using electrostatic and electrothermal MEMS scanner.

This paper is organised as follows. First, the mechanical construction of the device using S-shaped legs and realization of embedded heaters using thin Pt wires is presented. A trade-off between increasing rigidity and reduced thermal and inertial mass is discussed. Then, we present electrical connection in star configuration, and lumped model for thermal simulations. In section 2.3, we describe in detail the MEMS testing set-up, optical schematic, and MEMS fabrication process. Then, we present the fast mechanical response of the our electrothermal device. Though the actuator does not achieve the full range of displacement that has been previously demonstrated by electrothermal mirrors [32], [33], [42], [54], it features an unusually short thermal time constant that enhances dynamic operation near resonance. We then present multi-photon images of a sample pollen grain taken at varying depths by scanning the electrothermal mirror in a benchtop imaging system. We compare these images with the images taken by moving the specimen and holding the electrothermal scanner stationary. The axial resolution of our imaging system is estimated by measuring the light intensity at different depths.

2.2 MEMS Design

2.2.1 Mechanical Design

The electrothermal scanning mirror is designed to have a fast and large piston motion (z-axis), and in-plane rotation motion along x-axis (pitch), while minimizing coupling from rotation along the y-axis (roll). The top view schematic of the design is

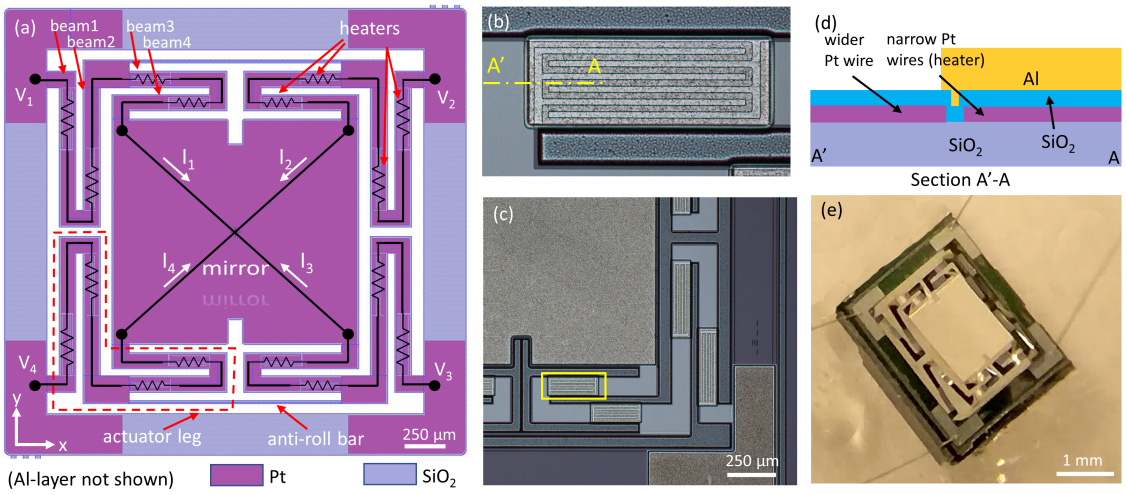

Figure 2.1: (a) Schematic of the electrothermal scanner in which the mirror is located at the center supported by four legs each having inner and outer folded U-shaped actuators. Each leg has four heaters connected in series made-up of thin Pt wires. This equivalent resistance for each legs are connected in star configuration. (b) Microscopic image of the individual heater showing 150 nm thick Pt wires 6 µm wide. (c) Device image during fabrication process. (d) Cross section A'-A of the actuator leg showing active heating and passive portion. (e) Image of released device wire bonded to a dual in-line package (DIP) chip.

shown in fig. 2.1(a). The mirror is located at the center of the device and supported by four actuator legs. As seen from fig. 2.1(a), each leg is composed of two folded U-shape actuators placed perpendicular to each other, referred to as outer and inner actuators in further discussion. In this design, the folded U-shaped actuators are used to minimize the potential lateral shift that occurs during the actuation of the legs. The left and right outer actuators are connected with each other by an anti-roll bar to reduce coupling of the y-axis rotation (or roll, defined in the plane of the mirror) when driving the MEMS in x-axis rotation. Comsol simulation has shown up to 40% reduction in roll upon asymmetric actuation in a design with anti-roll bars.

Each beam has an active section, with embedded heaters, and a passive section not intended to have internal heat generation. In each active section, embedded Pt heaters are sandwiched between 1 µm thick Al layer on top and 700 nm thick SiO_2 layer at the bottom. A thin insulation layer of 100 nm SiO_2 is deposited between the Pt heater and Al layer to avoid a short circuit. The Pt resistors are arranged in a serpentine shape with 7-10 passes as shown in fig. 2.1(b), each 6 µm wide and 150 nm thick. The overall stack sequence for the active segment from top to bottom is $Al/SiO_2/Pt/SiO_2$. The passive segment has a similar stack except without the Al layer and has a wide and uniform Pt layer, for low electrical resistance between active regions. The actuator beams can be considered as a bimorph and deform on heating

Table 2.1: Candidate support structures for FEA simulation

Candidate design	Parameter	value (µm)
Bulk silicon	device layer thickness	4, 10, 20, 30, 40
Concentric circles	pitch*	20, 30, 40, 50, 60
Honeycomb	hexagon side	20, 30, 40, 50, 60
Concentric squares	pitch*	20, 30, 40, 50, 60
Square grid	square side	40, 60, 80, 100

*distance between adjacent circles or squares

due to unequal thermal expansion coefficient of the material layers. The electrothermal actuators so constructed deform preferentially in one out-of-plane direction (Z, into the handle layer). The active section is primarily responsible for the deformation, however, the passive section also adds to displacement being a bimorph itself (SiO_2/Pt/SiO_2). Piston motion can be achieved by applying equal voltage across top and bottom legs. While, for pitch motion, the top and bottom two legs are actuated alternately.

It is desirable to have actuators curled out-of-plane upon fabrication. Nominally curled actuators can be realized by taking advantage of anticipated residual stress and stress gradients induced in the structure during fabrication. Typically, tensile and compressive stresses are observed in Al and SiO_2 layer, respectively, such that the actuator stacks curl upwards at room temperature. These residual stresses also deforms the mirror surface which is otherwise required to be flat for better quality imaging.

2.2.2 Support structure

Conventionally, the bending of a MEMS mirror due to residual stress is minimized by using a thick Si layer (∼20-40 µm) beneath the mirror surface to increase its rigidity [32], [33], [42], [53]–[55]. However, the thick Si layer also increase the inertial and thermal mass of the mirror reducing the natural vibration frequency and increasing the thermal time constant. In a high frame rate imaging system like an endomicroscope, it is often desired to have a fast scanning mirror (in this case, substantially faster than motion artifacts from phenomena such as breathing or heartbeats). In our design, we hypothesize faster mirror performance can be achieved by using a honeycomb-shaped support structure instead of a solid Si layer beneath the mirror, thereby increasing the mirror rigidity without addition of much inertial or thermal mass. The walls of the hexagon cells in the honeycomb structure are made of silicon-dioxide (TEOS) measuring 2 µm wide and around 40 µm deep.

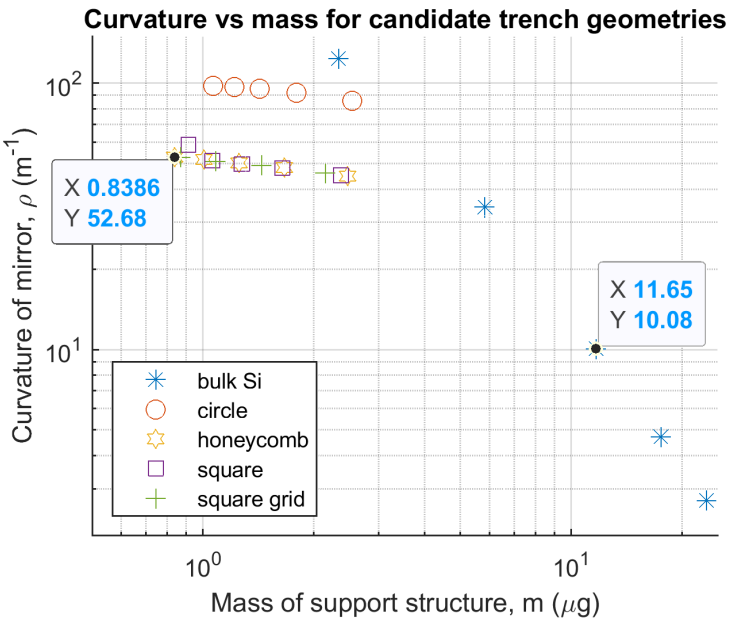

Figure 2.2: Comparison of mirror's curvature, predicted by FEA simulations under a representative residual stress, for candidate support structure geometries with varying parameter. x-axis represents the mass of each support structure.

The effectiveness of support structure placed below the mirror surface to reduce the bowing caused by residual stresses was studied qualitatively by running Finite Element Analysis (FEA). The FEA model (Comsol V5.4) involves a mirror of size 500x500 µm^2 made up of 1 µm thick Al on top of 0.8 µm thick SiO_2 layer supported by different candidate structures shown in fig. 2.3. The geometries considered in this study are a honeycomb, square grid, concentric circles, and concentric square with varying geometrical parameters as mentioned in table 2.1. The mirror was fixed at the center and a compressive pre-stress $\sigma^0_{xx} = \sigma^0_{yy} = -200$ MPa was applied on the SiO_2 layer. The mirror bows due to stress relaxation and the curvature was estimated by fitting a circle to the deformed surface profile. Figure 2.2 shows a plot of estimated curvature (ρ) measured along the x-axis, vs the normalized mass for the candidate design for various value of parameters as given in the table 2.1. As expected, the curvature is smallest (a more flat mirror) for the densely packed structure with little increase in mass. For instance, honeycomb structures with hexagon sides of 60 µm, compared to a mirror supported by a 20 µm thick bulk Si layer, has curvature of 52.68 m^{-1} versus 10.08 m^{-1}, and their masses measure 0.84 µg versus 11.65 µg respectively. In other words, by using the novel support structures, the mirror mass is reduced by a factor of 13.9 while the increase in curvature value is limited to 5.3 times the conventional design.

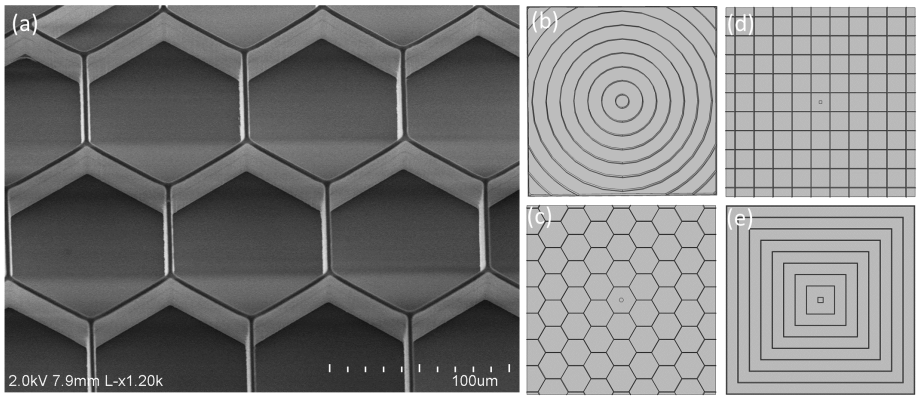

Figure 2.3: (a) SEM image of backside of a scanning mirror supported by honeycomb-shaped structure made from 2 µm wide, and around 40 µm high SiO_2 walls; (b)-(e) CAD of candidate support structure geometries.

Figure 2.2 suggests that the curvature does not changes rapidly, for a given class of design, as one move from sparse to densely packed structures. The honeycomb, concentric squares and grid like structure shows similar performance compared to concentric circles. We do note that structures that are not radially symmetric about the z-axis exhibit different curvature when measured along radial lines lying on the xy-plane. However, through simulation we have observed that variation in the curvature along a given radial line is not significant as one moves away from the center of the mirror. For radial symmetric design such as fig. 2.3(b), curvature is observed to be constant along all directions of measurement.

2.2.3 Trench refill

The support structure is realized by making trenches in single crystal silicon and subsequently filling them with TEOS oxide. The complete refill of trenches is vital to ensuring robust structure with good rigidity. The support structure wall thickness is limited by the TEOS process which tends to develop cracks at higher thickness. We did refill experiments with varying trench width from 2 to 6 µm size and found that 2 µm trench is optimum considering the other trade-offs. The DRIE etch creates a wider opening at the nodal location of lattice structure due to edge rounding. This makes it difficult to completely refill the trench and requires iterative TEOS and CMP steps. For instance, hexagonal, and square lattice and zoomed images of nodal points are shown in the fig. 2.4. Both geometries are not filled completely by a single step of 2 µm thick TEOS deposition. However, the nodal points on hexagonal lattice are easier to refill compared to those of a square trench, as the former involves only 3 lines meeting at nodes compared to 4 lines in later case. Ideally, a node-free support

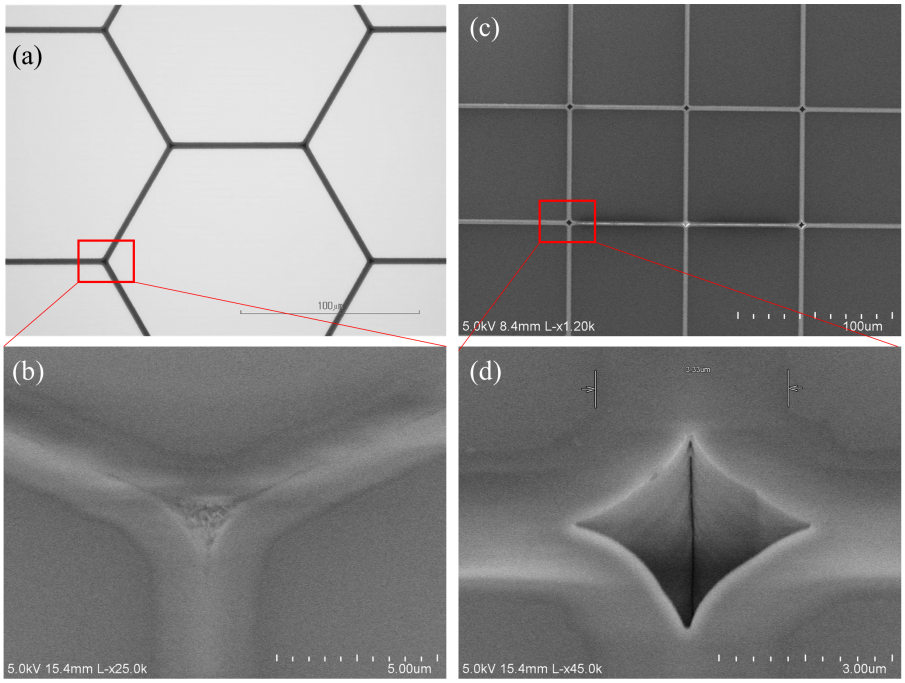

Figure 2.4: Comparison of trench refill for support structure geometries with three and four intersecting lines, (a)-(b) hexagonal lattice, and (c)-(d) square grid.

structural geometry, for example fig. 2.3(b) and (d), can be explored .

2.2.4 Electrical design

The legs are actuated by passing electrical current through the thin and narrow Pt wire which acts as a resistor and heats up due to Joule heating. Each leg has four heating elements connected in series as shown in fig. 2.1(a). These resistors along with the relatively wider Pt wires on the passive portions of the beams form an equivalent resistor R_i (where i=1, 2, 3, 4) corresponding to each leg. These equivalent resistors are connected in a star configuration as shown in fig. 2.1(a) to reduce the total number of independent electrical inputs to 4. Not all legs can be actuated independently using star configuration, but this is not required for achieving piston or pitch motion, so long R_i's values are close to each other. It is unlikely that all four resistors would be equal due to numerous uncertainties involved during fabrication process. A criterion on resistor values suitable for achieving ideal piston motion is derived in the appendix A. A mirror can be actuated along z-axis with an acceptable coupling in other direction even if the criterion is not satisfied.

Another configuration where each leg can be actuated independently could be realized by providing two terminals to each leg. A return electrical path on each leg

may reduce the overall reliability of the device and it will increase the total bond pads to 8. One might connect all four ground terminals with each other to reduce the number of bond pads (and electrical inputs) to 5. However, shorting the ground terminal of each leg requires routing the wires on the device frame. In severely space constraint application like endomicroscope probe, the device frame is designed with minimum width and routing additional wires may further reduce the fabrication yield and/or device reliability.

2.2.5 Thermal design: Static and dynamic simulations using circuit model

A lumped parameter circuit model was used to model the thermal behaviour of the actuator, as this approach consumes less computational resources, enables quick parametric studies, and offers rapid physical insights compared to various finite elements method (FEM) packages, such as Comsol, which can perform more detailed analysis. In the circuit model, we use only a quarter of the scanner, with appropriate symmetric boundary condition (BC), as the scanner design is symmetric about X and Y axes. The quarter portion includes one leg (consisting of four beams) and a quarter of a mirror. Modeling start by discretizing the active and passive sections of the thermal actuator beam into N elements, each of equal length. 1D heat balance equation for each element given by

$$C_n \frac{dT_n}{dt} = q_n + \frac{(T_{n-1} - T_n)}{R_n} - \frac{(T_n - T_\infty)}{R_h} - \frac{(T_n - T_{n+1})}{R_{n+1}}, \tag{2.1}$$

where C_n is the heat capacity, q_n is the heat source because of joule heating, R_n and R_h are conductive and convective resistance, respectively. In the above equation, we neglected the heat loss because of radiation as it is not the dominant source of heat dissipation. A total of $2N$ elements of the active and passive section are connected in series to model a single beam, which is repeated four times to represent an actuator leg as shown in fig. 2.5. The mirror is discretized in M elements and a symmetric BC is applied at the end. Though the mirror can conceptually be modeled more accurately with 2D (or 3D) heat equations, we also use a 1D heat flow approximation for the mirror for simplicity.

Note: During the repetition of discretized blocks shown in fig. 2.5, the parameters such as R_a, R_b, R_h, q_{gen}, etc., may take different absolute values for each beam due to differing length. For better visuals, subscripts representing beam number are not explicitly included here. Moreover, each R_n in eq. (2.1) takes a respective value of beam's $2R_a, 2R_p, 2R_m$ or combinations of them depending on whether it is in the

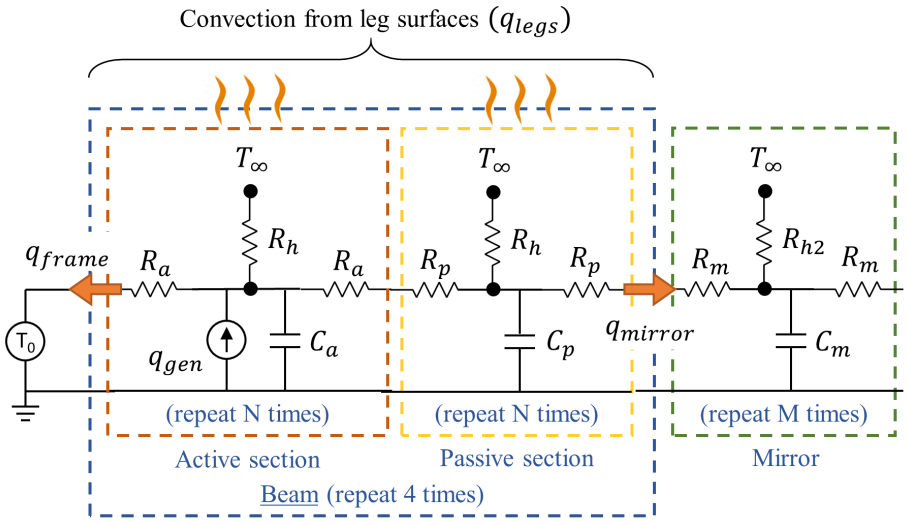

Figure 2.5: Lumped parameter circuit model for studying thermal behaviour of the MEMS device. A quarter of device is modeled with appropriate symmetric BC. Each active or passive section, and the mirror is discretized in N elements of equal lengths. These elements are highlighted by orange, yellow, and green color dotted box respectively.

Table 2.2: Heat dissipation mechanisms

heat dissipation mechanism		with 20 µm Si	without Si
convection from legs	q_{legs}	36.32%	68.04%
conduction to frame	q_{frame}	37.35%	28.72%
conduction to mirror	q_{mirror}	26.33%	03.24%

active, passive, or mirror section, or at their junction.

A fixed temperature (T_0) BC is used at the junction of frame and first active section because the MEMS frame acts as a heat sink and is assumed to remain at near constant temperature due to its relatively large surface area and high thermal conductivity. With some algebraic manipulation of eq. (2.1), the complete thermal model of the system involving all temperature variables can be written as

$$\boldsymbol{C}\dot{\boldsymbol{T}} + \boldsymbol{A}\boldsymbol{T} = \boldsymbol{q}, \tag{2.2}$$

where $\boldsymbol{C}$ is a diagonal matrix with heat capacity terms C_n, the matrix $\boldsymbol{A}$ is made of thermal conductance ($1/R$), and vector $\boldsymbol{q}$ represents heat source.

Among the class of out-of-plane electrothermal scanners that works by taking advantage of differences in thermal expansion co-efficient of layers, non-heating (passive) sections and the mirror itself are typically supported by a thick silicon layer ranging from 20-40 µm. The silicon layer may be used for various reasons such as increasing rigidity, improving mirror flatness, and/or adding mechanical amplification, [32]–[34],

Table 2.3: Material properties

Material	Thermal Conductivity (k) W/(m-K)	density (ρ) kg/m^3	Specific Heat Capacity (c_p) J/(kg-K)
Aluminum	237	2700	904
Silicon dioxide	1.4	2200	730
Platinum	71.6	21450	133
Silicon	130	2330	700

Table 2.4: Geometrical and other parameters used in simulation

parameters	symbol	value
Length of inner, and outer beams	L_i, L_o	740 µm, 470 µm
Active, passive section length ratio	$L_a : L_p$	1:1
Width of inner or outer beams	w	100 µm
Mirror width, and height	w_m, h_m	1440 µm, 1360 µm
Aluminium layer thickness	t_{Al}	1 µm
Silicon-dioxide layer thickness	t_{SiO_2}	0.8 µm
Silicon layer thickness	t_{Si}	20 µm
Frame temperature	T_0	25 deg C
Ambient temperature	T_∞	25 deg C
Total input power	Q_{gen}	10 mW
Convective heat transfer co-efficient	h	200 W/(m^{2}C)

[42], [53], [54], at the cost of increased thermal and inertial mass. Here, we compare,

(i) conventional design with thick Si layer beneath passive section and mirror;

(ii) proposed design without any silicon backing layer.

The material properties, geometry, and other parameters used for the simulation are given in table 2.3 and table 2.4. The lumped parameter model is given by eq. (2.2) was solved using Matlab and validated for select designs using a complete Comsol model that solves full 3D heat transfer equations by the finite element method. In Comsol simulation, the folded S-shaped leg was unfolded into a straight line for one-to-one comparison with the lumped model. In the solutions using either method, convection from the support structure walls was not considered for design (ii) as the SiO_2 is a poor conductor and little heat is conducted compared to the conductivity of the mirror layer. The steady-state temperature profiles from both methods are compared in fig. 2.6(a) for both designs (i) and (ii). The x-axis represents the path along the length of the actuator legs. The mirror, active, and passive sections are highlighted by green, orange, and blue respectively in fig. 2.6(a). We note that the lumped approximation fails at a relatively large value of Biot number, causing a minor discrepancy in temperature profile for the design with a Si layer, but otherwise there is close agreement between 1D and FEA modeling.

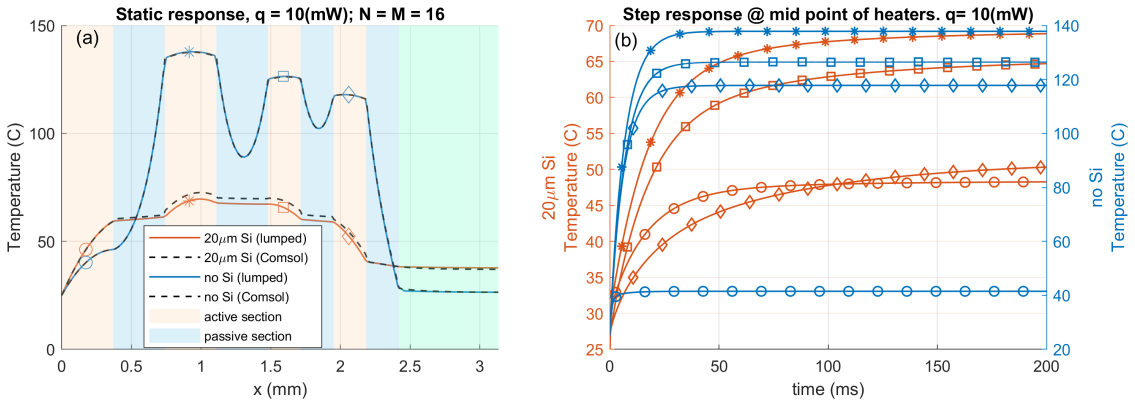

Figure 2.6: (a) Static analysis of thermal system using lumped model and Comsol, (b) step response of a thermal system obtained using a lumped model.

The temperature distribution in a passive section of design (i) is uniform compared to (ii). The silicon mass under the passive section of the beam acts as a heat sink/source depending on the heating/cooling cycle. Silicon being a good conductor of heat, the temperature distribution remains fairly uniform throughout its volume in the passive section. The non-uniform temperature distribution in the passive section without any silicon underneath is dictated by the temperature boundary condition coming from the active sections attached on either end. However, both designs shows a uniform temperature distribution on the active section which is desirable for uniform curling of the beams.

The heat generated by Joule heating is dissipated by a combination of the mirror, frame, and convection from the leg, and these relative proportions are tabulated in table 2.2 for both architectures. In the design (i), most of the heat is conducted to the mirror and frame resulting in lower temperature at the actuator and poor thermal efficiency compared to a design without a Si layer. One might improve the design (i) by inserting a thermal resistance at the ends connecting to the mirror and frame, but this may weaken the mechanical structure and reduce the overall reliability, while adding fabrication complexity.

For a step input, temperature as a function of time at the midpoints of each active section (labeled with different markers) is plotted in fig. 2.6(b). The left and the right y-axes show the modeled temperature for designs (i) and (ii) respectively. As seen from fig. 2.6(b), an actuator attached to the frame is fastest among all four actuators and overall thermal response is dictated by the time constants of the other three actuators. On average, 90% of the steady-state value is reached in less than 20 ms for the design without a Si layer, while it takes more than 100 ms for the other design. Thus, an electrothermal MEMS scanner without a thick silicon layer can achieve (a)

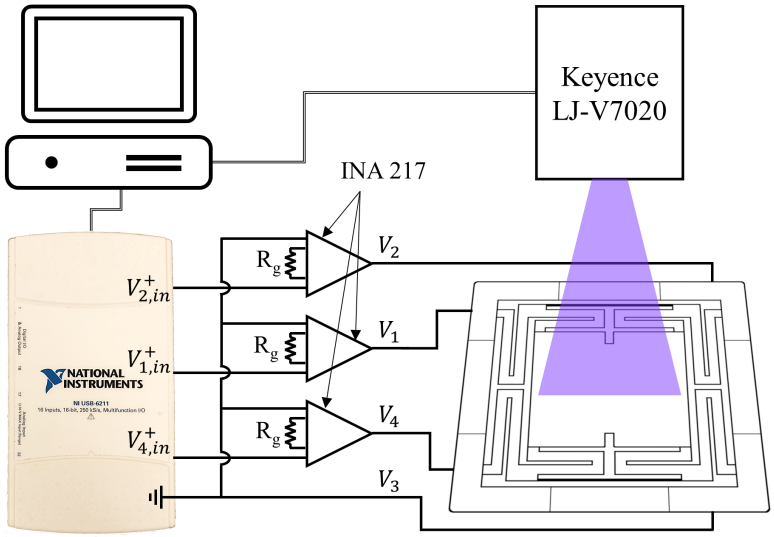

Figure 2.7: Schematic of mechanical characterization setup.

higher thermal efficiency; (b) faster dynamic response (more in section 2.4.2).

2.3 Methods

2.3.1 MEMS characterization set-up

The fabricated devices were mounted on DIP-chip and wire bonded. The chip carrier was plugged in a breadboard and powered using a DAQ (NI USB-6211) via an instrumentation amplifier (INA 217). The non-inverting terminals (V^+_{in}) of INA 217's were connected to the analog output of DAQ and inverting terminals (V^-_{in}) were grounded. A gain resistor $R_g = 560\ \Omega$ was used making the overall gain of the circuit to be 18.85. A LabVIEW code was developed to control the board and provide analog actuation voltage to the device. Keyence laser profiler LJ-V7020 was used to measure the translation and angular displacement of the device under test. The data from the profiler was processed using a Matlab script that extracted the displacement at required x-location and removed a DC offset. The schematic of the set-up is shown is fig. 2.7.

2.3.2 Imaging set-up

The schematic of the benchtop imaging system is shown in fig. 2.8. A short excitation pulse of ∼100 fs at 785 nm and 700 mW at the repetition rate of 80 MHz is generated using a mode-locked Ti-sapphire laser (Mai Tai DeepSee HP DS, Spectra-

Physics). The laser has a tunable spectral range of 690-1040 nm and comes with a dispersion compensation unit in-build to shorten the pulse width. A half-wave plate (HWP) and linear polarizer (LP) are placed after the laser to control the intensity and polarization state of the laser beam. The P-polarized light is then passed through a polarization beam splitter (PBS, PBS252, Thorlabs) and normally incident on lateral scanning electrostatic MEMS M1 previously developed [36]. The scanning mirror M1 reflects the beam and steers it in a Lissajous pattern. A quarter-wave plate (QWP, WPQ10M-780, Thorlabs) place between PBS and M1 changes the polarization state of light to S, and PBS reflects the beam towards lens L1 (f=30.0 mm, AC254-030-B, Thorlabs). The beam is expanded using a telescopic arrangement using lens L1 and L2 (f=150.0 mm, AC508-150-B, Thorlabs) to match the back aperture of the objective 1 (NA = 0.65, PLN 40X, Olympus).

The S-polarized light is then reflected by another PBS and passes through QWP and objective, and is reflected normally off the electrothermal MEMS mirror M2. M2 is moved in the axial direction to scan the focal point in a vertical plane similar to [49]. The polarization is changed back to P by the QWP and the beam is passed through the PBS. Another telescopic system, formed by L3 (f=75.0 mm, AC508-075-B, Thorlabs) and L4 (f=200.0 mm, AC508-200-B, Thorlabs), is used to match the aperture of the water immersed objective 2 (NA=0.95w, XLUM PLN FL 20X, Olympus). The specimen under objective 2 produces a fluorescence signal at more than half the wavelength of excitation light due to the non-linear multi-photon phenomenon. The fluorescence signal (green) is reflected by the long pass dichroic filter (DM, FF605-Di02, Semrock) towards a telescopic system L5 and L6. The fluorescence signal is measured using a photomultiplier tube (PMT, H7422-40, Hamamatsu) and a bandpass filter (BPF, FGB39, Thorlabs) is placed before the PMT to suppress the background noise. A high-speed current amplifier (59-178, Edmund Optics) is used to amplify PMT current. The amplified signal is digitized by a high-speed data acquisition board (National Instruments (NI), PCI-6115). Both the electrostatic and electrothermal MEMS mirrors were actuated using another data board (NI, PCI-6711). LabVIEW software was developed to control the boards and reconstruct the image from the digital signal.

2.3.3 Fabrication

We start by ethching silicon dioxide trenches for the support structure framework into a silicon wafer using deep reactive-ion etching (DRIE). These high aspect-ratio trenches are filled by tetraethyl orthosilicate (TEOS) silicon dioxide and the top

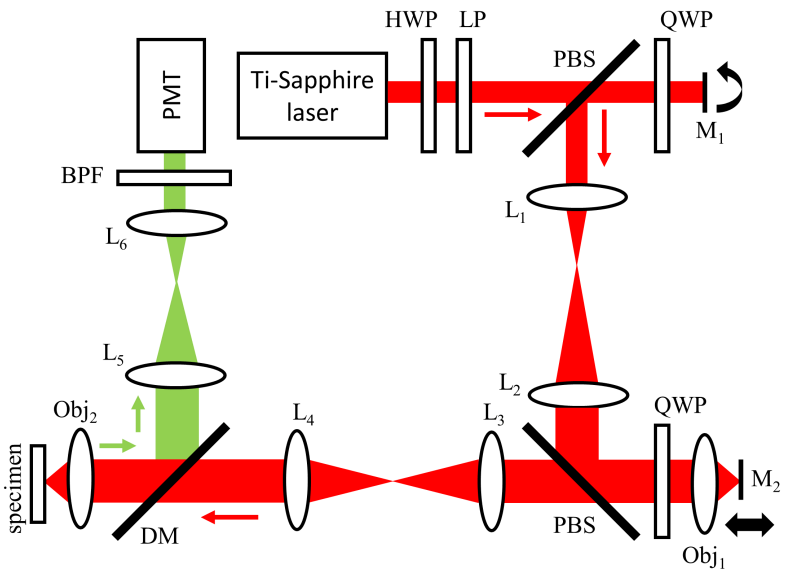

Figure 2.8: Optical schematic of a benchtop multi-photon imaging system.

surface is planarized by chemical mechanical polishing (CMP). If required, the TEOS deposition and CMP are done repeatedly till the trenches are filled completely. A structural layer of 700 nm thick SiO_2 is deposited by a low-pressure chemical vapor deposition (LPCVD) process on top of the planarized wafer. Pt heaters are realized by depositing 150 nm thick and 6 µm wide Pt wires with a thin layer of Ti as an adhesion promoter using e-beam evaporation, followed by lift-off. A thin insulation layer of 100 nm SiO_2 is deposited by a plasma-enhanced CVD process and patterned at the contact pad to reduce the contact resistance. 1 µm thick Al is sputtered using physical vapor deposition (PVD) followed by lift-off to form the mirror surface, active sections of the legs, and bond pads. It is observed that the thicker the Al layer, the lower the mirror quality, however to reduce the fabrication complexity we deposited Al for the mirror and structural layer in the same step. Alternately, a second lithography step could be used to customize mirror thickness. The mirror, actuator legs, and frame geometry are patterned by RIE of SiO_2 followed by a shallow DRIE of Si. Finally, the backside Si is etched by patterning oxide layer, which serves as a hard mask, followed by DRIE process. The devices are unmounted by soaking in an acetone bath followed by isopropyl alcohol (IPA) and dried in air/hotplate. The fabrication process flow is summarized in fig. 2.9.

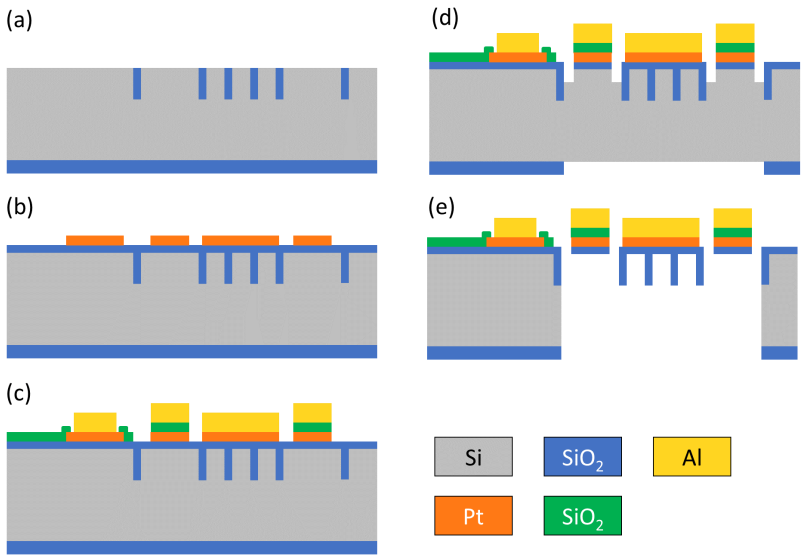

Figure 2.9: Fabrication process. (a) 2 µm wide, around 40 µm deep trenches made on single crystal Si wafer, refilled with SiO_2 by TEOS process and excess SiO_2 from top side removed by CMP. (b) 700 nm thick SiO_2 deposited using PECVD process followed by evaporation and lift-off of 150 nm thin Pt layer. (c) PECVD deposition of 100 nm thin SiO_2 insulation layer followed by sputtering and lift-off of 1 µm thick Al layer. (d) Mirror, actuator legs, and frame geometry patterned by RIE of SiO_2 followed by a shallow DRIE of Si. (e) Device is released by a backside DRIE of Si followed by cleaning in acetone, IPA bath and drying in air/hotplate.

2.4 Results

2.4.1 Mirror curvature measurement

The surface profile of the released device was measured using a non-contact optical 3D profiler (Zygo NewView 5000) at a frame rate of 120 Hz. The 3D profile of the device is shown in the inset of fig. 2.10. The mirror is supported by a honeycomb structure with hexagon side of 50 µm. A slice of the surface profile along the mirror's x-axis is plotted and the measured radius of curvature is $\rho = 29.35$ mm. The mirror bowed just 7.5 µm over the length of 1.2 mm validating the advantage of the support structure. Residual stress of -128 MPa in the aluminum layer was extracted using the FEA model by fitting the simulated curvature with the experimentally measured one. The extracted stress just provides a perspective assuming nominal properties in other layers and may not indicate actual stress distribution in the mirror platform.

2.4.2 Dynamic model and MEMS response

The dynamics of the electrothermal scanners are modeled using a first-order thermal system, and a second-order mechanical system consisting of a spring, mass, and

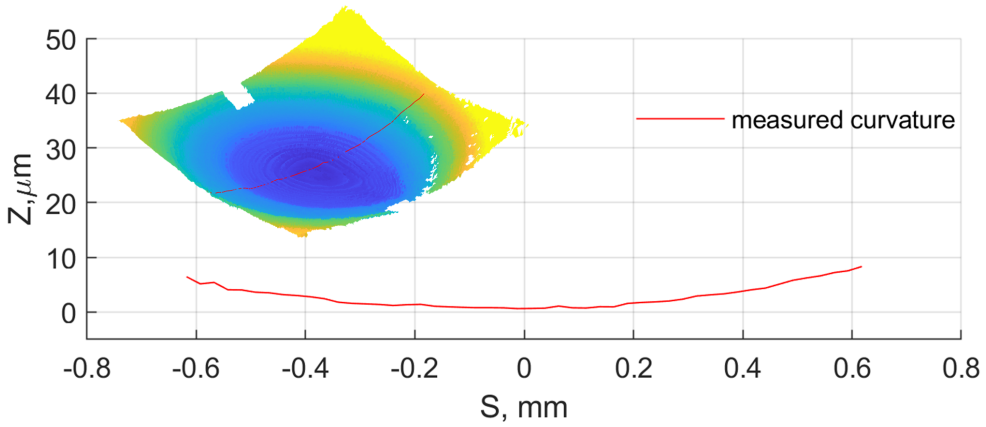

Figure 2.10: Surface profile of the released device measured along it's x-axis. Profile extracted from the 3D topography (inset) measured using an optical profiler.

Table 2.5: Comparison of static displacement/power, time constant, and mirror size with prior work

authors	static displacement/ power (µm/mW)	time constants (ms)	Si substrate thickness at leg (µm)	mirror (µm)	mirror size (mm^2)
A. Jain [53]	2.85	6.7*	0	40	0.19 x 0.19
L. Wu [32]	1.25	25	20	20	0.5 x 0.5
K. Jia [54]	1.03	4.54*	0	40	1.0 x 1.0
L. Liu [33]	N.R.	>250*	40	40	1.0 x 1.0
X. Zhang [42]	1.43	5.56	0	varies	0.9 x 0.9
F. Han [34]	N.R.	63.63*	40	40	1.2 x 1.3
C. Guo[55]	rotation only	0.25, 0.46**	0	N.R.	1.0 x 1.0
this work	2.08	3.42	0	0	1.36 x 1.44

* inferred from resonant behavior or transient response

** time constant without mirror assembly

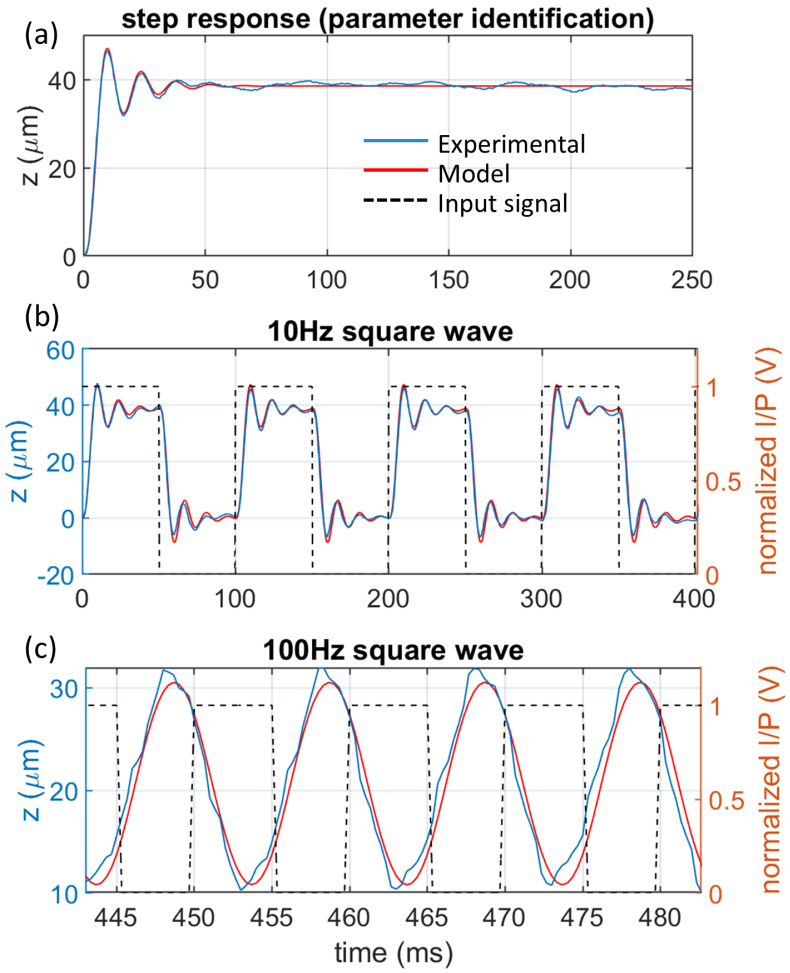

Figure 2.11: Experimentally measured displacement of a representative device at the center of the mirror for various input signal (a) step input, (b) and (c) square wave at 10 Hz and 100 Hz respectively.

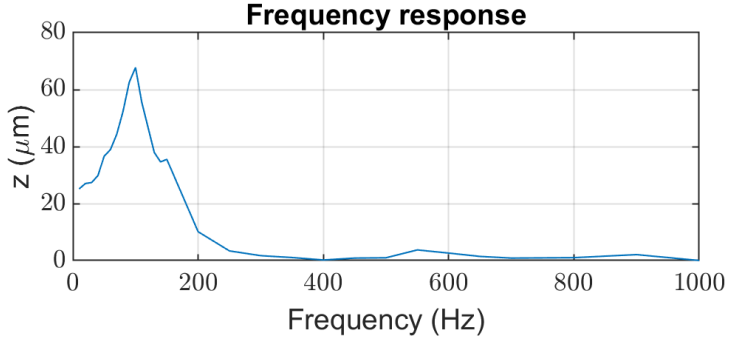

Figure 2.12: Experimentally measured frequency response of one of the representative electrothermal scanners with hexagon support structures.

a damper. The Laplace domain transfer function with zero initial condition for the mechanical and thermal system can be written as

$$G_m = \frac{Z(s)}{F(s)} = \frac{k_m}{s^2 + 2\zeta\omega_n s + \omega_n^2} \tag{2.3}$$

$$G_{th} = \frac{T(s)}{Q(s)} = \frac{k_{th}}{s + p_1}. \tag{2.4}$$

The deflection of the bimetal strip under uniform heating was derived by Timoshenko [56] under various ideal conditions. For the small curvature of strip bending it can be shown that the tip displacement is proportional to temperature change $\Delta z = k_b \Delta T$. The coupled dynamics of the system can be studied by converting the static tip displacement as an external equivalent force applied to the spring, mass, and damper system. The equivalent force then becomes $F_{eq} = k\Delta z = k(k_b \Delta T)$, where k is the spring constant in the mechanical model. The combined transfer function then becomes

$$G = \frac{Z(s)}{Q(s)} = \frac{K}{(s + p_1)(s^2 + 2\zeta\omega_n s + \omega_n^2)}, \tag{2.5}$$

where $K = k_m k_{th} k_b k$.

The parameters in the dynamic model mentioned above were extracted by fitting the theoretical response obtained by eq. (2.5) with the experimentally measured step response as shown in fig. 2.11(a). The scanner was actuated in piston motion by applying 5 V across adjacent legs, and the measured resistance of each leg at room temperature was around 1.3 kOhm. The parameters identified by fitting the model (2.5) are $K = 2325.5$ m/s^{3}W, $p_1 = 292.07$ rad/s, $\zeta = 0.1786$, $\omega_n = 454.23$ rad/s ($f_n = 72$ Hz). The time constant of the combined response of the system is dominated by thermal pole p_1 and has a value of $\tau = 3.42$ ms. With the total input power of 19.23 mW (9.62 mW for each pair of legs), the static displacement per unit power is estimated to be 2.08 µm/mW. The model was further validated by comparing the response predicated by the extracted parameters with the experimental response for a square wave input. The device response at a frequency below and above the first resonance frequency ($f_1 = 72$ Hz) of that device is shown in fig. 2.11(b), and (c). Figure 2.12 shows a typical frequency response of the scanner at 5.65 V peak-to-peak (2.82 V DC offset), with mechanical resonance near 100 Hz reached prior to the thermal time constant roll-off (devices used to generate the plot in fig. 2.11 and fig. 2.12 are different). This permits comparatively high-speed scanning of the mirror for rapid cross-sectional imaging of tissue.

A hysteresis plot of a scanner was obtained when driven in piston motion by

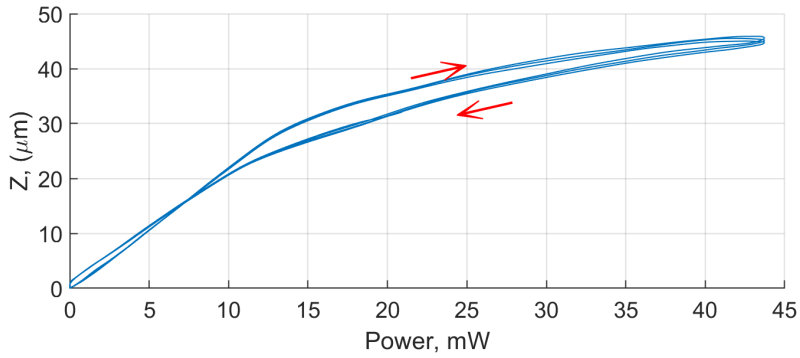

Figure 2.13: Experimental hysteresis curve of a piston motion plotted as a function of estimated input power.

applying modest voltage (V) at 1 Hz sine wave. The displacement is plotted as function of power input in fig. 2.13. Note that the plot does not represents the full range of motion that a scanner can achieve. The input power (P) in the plot was estimated by $P = V^2/R$, where the electrical resistance (R) is assumed to be constant. At lower input voltage the plot (fig. 2.13) is linear. As the voltage increases the constant R assumption breaks and resistance increases significantly. This decreases the slope of the plot at the high power as estimated power is more than the actual power seen by active section.

Table 2.5 provides the comparison of mirror size, time constant, and static displacement per unit input power for selected previously reported electrothermal scanners. Reducing the inertial and thermal mass at the actuator legs and mirror enabled us to achieve a very small overall time constant (τ) of the system. In spite of having a larger mirror surface we demonstrate a faster response with $\tau = 3.42$ ms compared to the majority of prior electrothermally-actuated scanners [32]–[34], [42], [54]. Another difference with prior works is extension of the pole from the thermal time constant into comparable frequency range as the resonance, permitting resonant excitation prior to thermal role-off. As a result, the mirror step response resembles an underdamped system (though strictly speaking third-order dynamics are significant). The scanner speed could be further improved by operation in closed-loop, which can be achieved with significantly less control effort due to approximately underdamped system. Additionally, the static response of 2.08 µm/mW is achieved because of improved thermal efficiency of our MEMS for the reasons discussed in section 2.2.5.

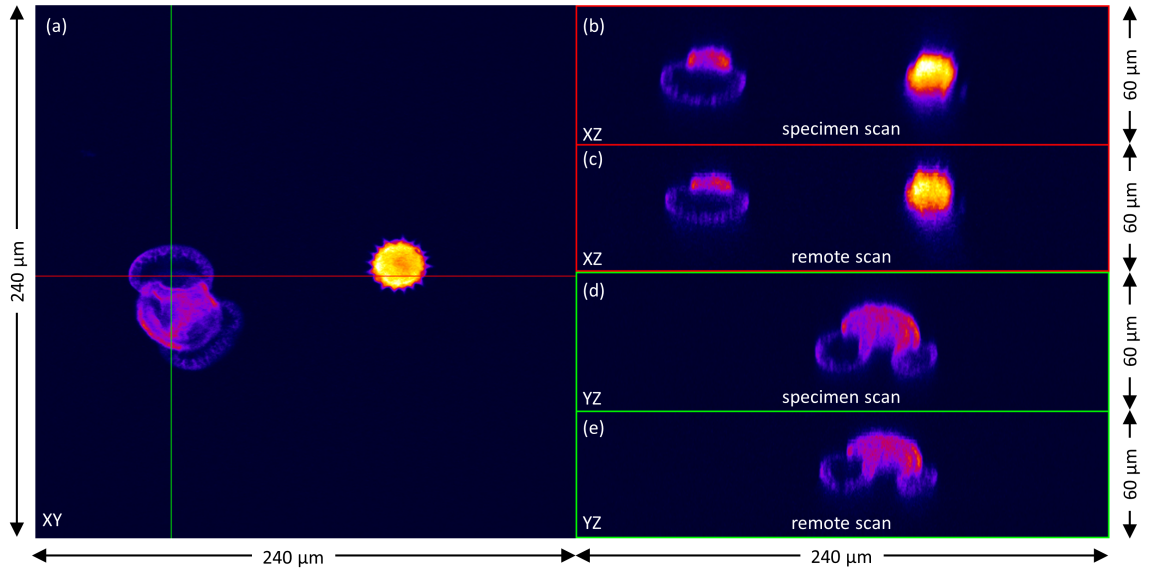

Figure 2.14: Sample multi-photon images of pollen grains (a) image in lateral (XY) plane captured by scanning mirror M1; image along vertical cross-section (XZ) and (YZ) marked with red and green lines in (a) reconstructed by capturing multiple lateral (XY) images at varying depths by (b) and (d) moving specimen, (c) and (e) scanning electrothermal scanner in axial direction.

2.4.3 Multi-photon 3D imaging

The imaging performance of the electrothermal actuators was tested using the benchtop testbed for multi-photon endomicroscopy as described in section 2.3.2. Sample multi-photon images of pollen grains (Carolina Biological Supply Inc) measuring 30-40 µm in diameter were captured in lateral (XY) plane over a FOV of 240 x 240 µm^2 at a frame rate of 5 Hz per slice. Vertical cross-sections (XZ and YZ) with FOV measuring 240 x 60 µm^2 were constructed using stacked lateral images collected at varying depths. Figure 2.14(a) shows an example of a lateral image at an intermediate depth. The electrothermal scanner's performance was assessed by comparing two sets of image stack collected by

(i) moving the mirror M2 in axial direction and holding the specimen stationary (remote scan), and

(ii) holding M2 stationary and moving the specimen vertically along the optical axis (specimen scan).

There is no visible difference between these two sets of images as evident from fig. 2.14(b)-(e). During imaging, it was observed that factors like the flatness and roughness of the mirror surface formed on the silicon dioxide lattice did affect the image quality.

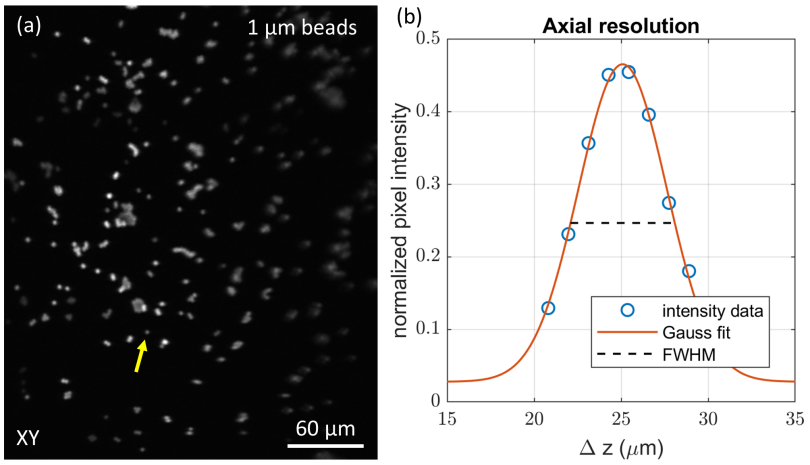

Figure 2.15: Estimation of axial resolution of a benchtop multi-photon system by imaging fluorescence beads of around 1 µm diameter shown in (a) at varying depth. (b) Intensity plot of arbitrarily chosen bead (arrow) at varying depths.

The axial resolution of the imaging system was estimated by taking images of 1 µm wide fluorescence pollen bead at varying depths. Then, the image intensity of an arbitrarily chosen isolated pollen grain is plotted as a function of the scanning depth and a Gaussian curve is fit as shown in the fig. 2.15. The axial resolution of 6 µm is calculated by measuring the full-width half maximum (FWHM) at the peak of the fitted Gaussian.

2.5 Discussion

In this work, we demonstrated a lightweight electrothermal MEMS actuator using a novel honeycomb-shaped support structure made up of silicon dioxide walls. The fabrication process starts by etching narrow trenches and refilling them using the TEOS process and polishing the top oxide layer as described above. Multiple rounds of TEOS and polishing are required to completely fill the trenches especially at the intersection of edges. One way to avoid this is by exploring intersection free geometry like concentric circles or squares at the cost of increased mirror curvature.

Electrothermal micro-mirrors are typically supported by bulk silicon measuring 20-40 µm to increase the rigidity and reduce the mirror curvature. However, this adds to the inertial and thermal mass of the system leading to slow dynamic response. We demonstrated a fast electrothermal scanner, particularly with respect to mirror size, having a time constant as small as 3.42 ms for the open-loop system. The lumped parameter model developed for our scanner shows good agreement with the experimental results. The response time could be further reduced by using the closed-

loop control system and appropriately placing poles and zeros. The enhanced thermal efficiency leads to a static response of 2.08 µm/mW. The efficiency could be further improved by restricting the heat generated to the actuator volume by adding thermal resistance at the junction of legs with the device frame, and mirror. A potential trade-off is reduced mechanical robustness, though mirror mechanical strength has not been quantitatively evaluated. The honeycomb structure also makes the complete mirror area usable which otherwise is not possible in devices that involve an isotropic Si etch step.

A star configuration was used for the electrical connection to reduced the number of independent inputs to four, and thereby reducing the footprint of the frame required for wiring. A criterion on the electrical resistance of the heating element was developed to achieve ideal decoupled piston motion. Five or eight input configuration can be used independently to actuate the mirror legs for an application having space flexibility.

We demonstrated multi-photon 3D imaging of pollen beads on the benchtop system at a frame rate of 5 Hz per slice. A high frame rate is desired to observed many biological processes that evolve in real-time. In our system, both lateral and axial scanning was done using the MEMS scanner at the proximal end which doesn't require moving objective or specimen. This is advantageous for miniaturization and paves way for space constraint applications like endomicroscopy. However, we note that management in endoscopes that involves electrothermal scanners is still an open question given potential effects on convection and conduction through air an enclosed space.

2.6 Conclusion

In this paper, MEMS-based multi-photon 3D imaging taken on a bench-top system that doesn't require movement of an objective or specimen for depth scanning was demonstrated. The lateral scanning was achieved using a parametrically-resonant electrostatic MEMS scanner while axial scanning by a novel electrothermal MEMS scanner. A honeycomb support structure for the electrothermal scanner's mirror mitigated bowing of the mirror under residual stress with small mass, also increasing thermal efficiency. Due to the low thermal and inertial mass we were able to scan the MEMS at more than 150 Hz with displacement comparable to static actuation. Multi-photon images captured by displacing the electrothermal MEMS scanner show no appreciable difference from those taken by moving the sample. Pollen grain images

were captured with an axial resolution of 6 µm. The beam scanning performed using remote MEMS scanners both in lateral and axial directions paves the way for miniaturization of the system in a handheld form-factor enabling real-time *in-vivo* studies in mouse models.

CHAPTER III

Piezoelectric Actuators

3.1 Introduction

As previously introduced, endomicroscopy is an emerging screening technique. Recently, researchers have developed a miniaturized probe that can fit inside the instrument channel of a conventional endoscope [6]. The ability to distinguish between pre-cancerous and benign lesions during an endoscopy procedure can revolutionize health care. Among different endomicroscopy techniques such as proximal or distal scanning, fiber scanning, [19], [20], fiber bundle, etc., image acquisition using MEMS scanners has demonstrated significant improvement in frame rate and field of view over other techniques [6], [16]. The development of miniaturized and custom MEMS to suit the optical design and packaging requirements plays a key role in the success of miniaturizing these imaging probes.

Among the four popular actuation techniques in MEMS scanner namely, electrothermal, electrostatic, electromagnetic, piezoelectric, the last one has some unique advantages over others. For instance, piezoelectric scanners can be actuated in a low frequency (or DC) to mid-frequency (kHz) range with relatively large displacement at comparatively low actuation voltage. The bandwidth from DC to kHz range is advantageous when collecting images using raster scanning. Meanwhile, a higher frame rate can be achieved by operating the device with a high input frequency. However, there are not currently scanners that can operate effectively in both DC and high-frequency modes. A carefully designed, multi-degree-of-freedom (DOF) scanner could randomly access a small section of an endoscope's FOV for repeated imaging at a potentially higher frame rate or for increased signal-to-noise ratio via averaging. This random access capability is important to observe biological processes which occur at various time scales.

The key requirements of a scanner in such applications are, first, multiple DOF as desired for 2D or 3D scanning; second, minimal coupling with other DOFs when

actuated along a particular DOF; third, a robust design that can tolerate asymmetric actuation due to variation in geometry and material properties. The displacement requirements are mostly dictated by the optical design. For multi-photon applications, piston motion of more than 200 µm in DC and in-plane angular rotation of more than 6° in DC are required.

In this work, we present the design of a piezoelectric scanner that satisfies the aforementioned requirements. The chapter is organized as follows: first, we discuss the linear piezoelectric constitutive relations and briefly described a piezoelectric material, lead zirconate titanate (PZT). We then present our MEMS scanner design that used an anti-roll bar and torsional spring to reduce coupling and increase robustness. The FEA simulations are used to assess the effectiveness of these structural members. A fabrication process is described that is used to realize the MEMS scanner.

3.2 Linear piezoelectric constitutive 3D equations

According to the standard adopted by IEEE the piezoelectric constitutive equations in tensor notation are given by

$$T_{ij} = c^E_{ijkl} S_{kl} - e_{kij} E_k \tag{3.1}$$

$$D_i = e_{ikl} S_{kl} + \epsilon^S_{ik} E_k \tag{3.2}$$

where T_{ij}, S_{kl}, D_i, and E_k are components of stress tensor $\mathbf{T}$, strain tensor $\mathbf{S}$, electric displacement vector $\mathbf{D}$, and electric field vector $\mathbf{E}$, respectively. c^E_{ijkl}, e_{ikl}, and ϵ^S_{ik} are the elastic, piezoelectric, and dielectric constants, respectively. The superscript ^{E} and ^{S} represents constants' value when electric field and strain is held constant, respectively. The tensor eqs. (3.1) and (3.2) can be written in a compact matrix notation by using a 2D matrix for elastic, piezoelectric, and dielectric constants c^E_{ijkl}, e_{ikl}, and ϵ^S_{ik}. We replace ij or kl by p or q, where i, j, k, l takes the values $1, 2, 3$ and p, q take the values $1, 2, 3, 4, 5, 6$. The compact constitutive relationships can be written as:

$$T_p = c^E_{pq} S_q - e_{kp} E_k \qquad \Longleftrightarrow \quad \{T\} = [c^E]\{S\} - [e]^T\{E\} \tag{3.3}$$

$$D_i = e_{iq} S_q + \epsilon^S_{ik} E_k \qquad \Longleftrightarrow \quad \{D\} = [e]\{S\} + [\epsilon^S]\{E\} \tag{3.4}$$

The components T_i and S_i of vectorized stress and strain tensor are defined as:

$$\begin{Bmatrix} T_1 \\ T_2 \\ T_3 \\ T_4 \\ T_5 \\ T_6 \end{Bmatrix} = \begin{Bmatrix} T_{11} \\ T_{22} \\ T_{33} \\ T_{23} \\ T_{13} \\ T_{12} \end{Bmatrix} \quad \begin{Bmatrix} S_1 \\ S_2 \\ S_3 \\ S_4 \\ S_5 \\ S_6 \end{Bmatrix} = \begin{Bmatrix} S_{11} \\ S_{22} \\ S_{33} \\ 2S_{23} \\ 2S_{13} \\ 2S_{12} \end{Bmatrix} \tag{3.5}$$

The form of constitutive laws described by eqs. (3.1) and (3.2) or eqs. (3.3) and (3.4) is known as stress-electric displacement. The other popular form is strain-electric displacement equations, in addition to two other less common forms. All four forms are summarized in table B.1

3.2.1 Simplified constitutive equations in Euler-Bernoulli beam

In a thin beam structure which can be modelled using Euler-Bernoulli's beam theory, only the axial stress along the length of the beam is significant and rest all stresses can be neglected. Additionally, for the piezoelectric material polled in z-direction (thickness) the electric field in other direction can be assumed to be zero. We make the following assumption:

$$\begin{aligned} T_2 = T_3 = T_4 = T_5 = T_6 = 0 \\ E_1 = E_2 = 0. \end{aligned}$$

The strain- and stress- displacement equations then becomes, respectively,

$$\begin{Bmatrix} S_1 \\ D_3 \end{Bmatrix} = \begin{bmatrix} s_{11}^E & d_{31} \\ d_{31} & \epsilon_{33}^T \end{bmatrix} \begin{Bmatrix} T_1 \\ E_3 \end{Bmatrix}, \text{ and } \begin{Bmatrix} T_1 \\ D_3 \end{Bmatrix} = \begin{bmatrix} \bar{c}_{11}^E & -\bar{e}_{31} \\ \bar{e}_{31} & \bar{\epsilon}_{33}^S \end{bmatrix} \begin{Bmatrix} S_1 \\ E_3 \end{Bmatrix}. \tag{3.6}$$

where,

$$\bar{c}_{11}^E = \frac{1}{s_{11}^E}, \quad \bar{e}_{31} = \frac{d_{31}}{s_{11}^E}, \quad \bar{\epsilon}_{33}^S = \epsilon_{33}^T - \frac{d_{31}^2}{s_{11}^E} \tag{3.7}$$

3.2.2 Simplified constitutive equations in Timoshenko beam

In a moderately thick beam structure which can be modelled using Timoshenko's beam theory, transverse shear stress (T_5) can not be neglected. Thus, all other stress component are much smaller that T_1 and T_5. Similar to constitutive equations in Euler-Bernoulli beam, we assumed the electric field components in lateral direction

to be zero. We make the following assumption:

$$T_2 = T_3 = T_4 = T_6 = 0$$
$$E_1 = E_2 = 0.$$

The strain- and stress- displacement equations for Timoshenko's beam are:

$$\begin{Bmatrix} S_1 \\ S_5 \\ D_3 \end{Bmatrix} = \begin{bmatrix} s_{11}^E & 0 & d_{31} \\ 0 & s_{55}^E & 0 \\ d_{31} & 0 & \epsilon_{33}^T \end{bmatrix} \begin{Bmatrix} T_1 \\ T_5 \\ E_3 \end{Bmatrix}, \text{ and } \begin{Bmatrix} T_1 \\ T_5 \\ D_3 \end{Bmatrix} = \begin{bmatrix} \bar{c}_{11}^E & 0 & -\bar{e}_{31} \\ 0 & \bar{c}_{55}^E & 0 \\ \bar{e}_{31} & 0 & \bar{\epsilon}_{33}^S \end{bmatrix} \begin{Bmatrix} S_1 \\ S_5 \\ E_3 \end{Bmatrix}. \quad (3.8)$$

where, $\bar{c}_{11}^E$, $\bar{e}_{31}$, and $\bar{\epsilon}_{33}^S$ are given by eq. (3.7) and

$$\bar{c}_{55}^E = \frac{1}{s_{55}^E}. \quad (3.9)$$

Along similar lines, we can also write simplified constitutive laws for Kirchhoff plate and moderately thick plate with the following assumptions:

$$T_3 = T_4 = T_5 = 0, \text{ and } E_1 = E_2 = 0 \qquad \text{(Kirchhoff plate)}$$
$$T_3 = 0, \text{ and } E_1 = E_2 = 0 \qquad \text{(moderately thick plate)}$$

3.3 PZT (Lead Zirconate Titanate)

Lead zirconate titanate a.k.a. lead zirconium titanate (PZT) is a piezoelectric material with the chemical formula $Pb[Zr_xTi_{1-x}]O_3$, where $0 \leq x \leq 1$. PZT is a ceramic having perovskite crystal structure. Perovskite compounds, named after Russian mineralogist L. A. Perovski (1792-1856), has a general chemical formula ABX_3, where 'A' and 'B' are two cations of very different sizes, and X is an anion that bonds to both. PZT when heated above the "Curie temperature (T_c)" exhibits simple cubic symmetric as shown in fig , however, at a temperature below T_c the crystal structure changes to tetragonal symmetry. An electric dipole is induced in each crystal structure due to displacement of cations Zr^{4+} and Ti^{4+} below T_c. Neighboring crystals may form a region of net dipole moment called "domain". However, the orientation of different domains in the PZT material are random and thus the bulk material has no net dipole moment. The individual domains can be aligned in same direction through a process called "pooling" when a strong DC field (less than dielectric breakdown) is applied at a temperature below T_c. The domains are locked in roughly same configuration

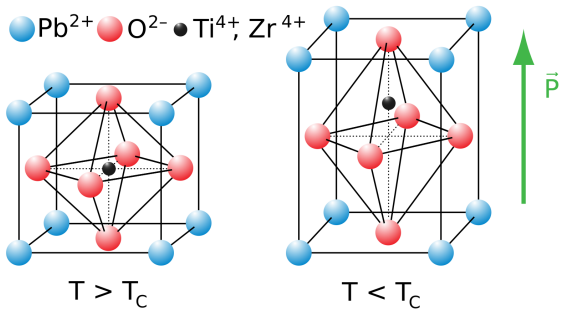

Figure 3.1: Tetragonal unit cell of lead zirconate titanate. Image credits: Pinin - Wikimedia Commons

when the electric filed is removed on cooling the material to room temperature. The pooling process induces both permanent polarization and elongation in PZT material.

3.4 MEMS scanner design

The thin film PZT MEMS scanner design is similar to the previously developed electrothermal scanner [57]. The scanner consists of four U-shaped outer legs placed at each corner of scanner frame. Inner legs are made by narrow similar U-shape legs placed perpendicular to outer legs. The outer legs on the right are connected with legs on the left by an anti-roll (AR) bar to suppress the coupling when actuated along multiple-axis. A torsional spring (TS) is connected with the AR bar and centrally located mirror. The TS is used to minimize the piston motion while driving the scanner in in-plane rotation (Y-roll). Each long beams, that makes U-shape leg, have bend-up and bend-down portion to enhance out-of-plane displacement of the leg tip. The bend-up section is a composite beam made from silicon-dioxide as a base structural layer, and a PZT stack consisting of thin film PZT layer sandwiched between top and bottom layer of Pt. The bend-down portion has additional layer of Al on top of PZT stack. The layers thickness are such that neutral axis for the composite beam lies below and above the mid plane of PZT layer for bend-up and bend-down section, respectively. A thin parylene layer may be used to encapsulate the edges of the beam structure to prevent delamination of top Pt layer. Bond pads are made at suitable location on the frame and wires are routed accordingly.

3.5 Finite element analysis and simulations

A static analysis and eigen frequency analysis were performed using Comsol to assess the qualitative performance of the PZT scanners. It is difficult to predict the

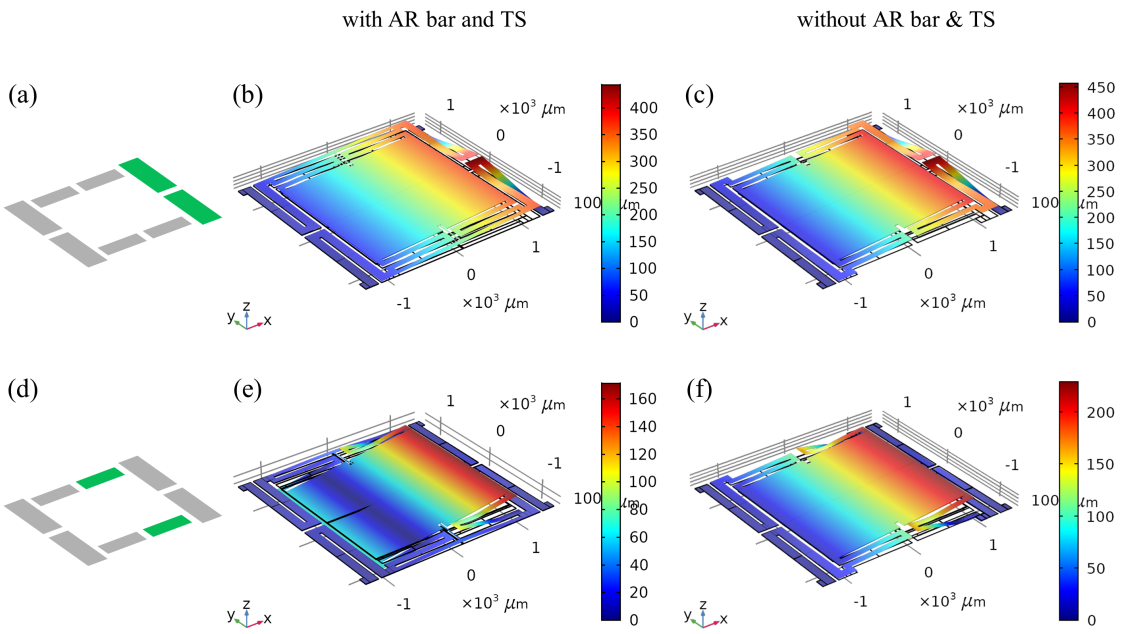

Figure 3.2: Comparison of displacement plots for scanner design with and without AR bar and TS. (a) and (d) cartoon depicting the actuated legs in green color, (b) and (c) right outer legs, (e) and (f) right inner legs.

quantitative behaviour of the actuators exactly as many parameters that are essential for accurately modeling of the device can not be measured/estimated. For instance, the effective coupling co-efficient (d_{31}) of the PZT is dependent on temperature cycling the PZT layer see during the complete fabrication process. Similarly, the residual stress and stress gradient are difficult to estimate.

3.5.1 Effect of anti-roll bar and torsional spring

The scanner domain is modeled by a coupled physics, solid mechanics and electrostatic, in Comsol. We used the coupling coefficient $d_{31} = 120$ pC/N for the thin film PZT layer, and isotropic materials models form Comsol library for other layers. First, we perform FEA simulations to check the effectiveness of the AR bar and TS in suppressing the cross-talk between the various degrees of freedom of the mirror platform. We evaluate the performance of scanners with and without AR bar and TS, keeping other geometry unchanged. The AR bar is expected to reduced the roll motion (Y-axis) when actuated asymmetrically about that axis. We apply 10 V to the top electrodes of the outer-right legs and ground all other legs. As seen from the fig. 3.2(b) and (c), the angular (roll) and translation (piston) displacement for the design with and without AR bar are 8.67° and 10.48°, 213 µm and 227 µm, respec-

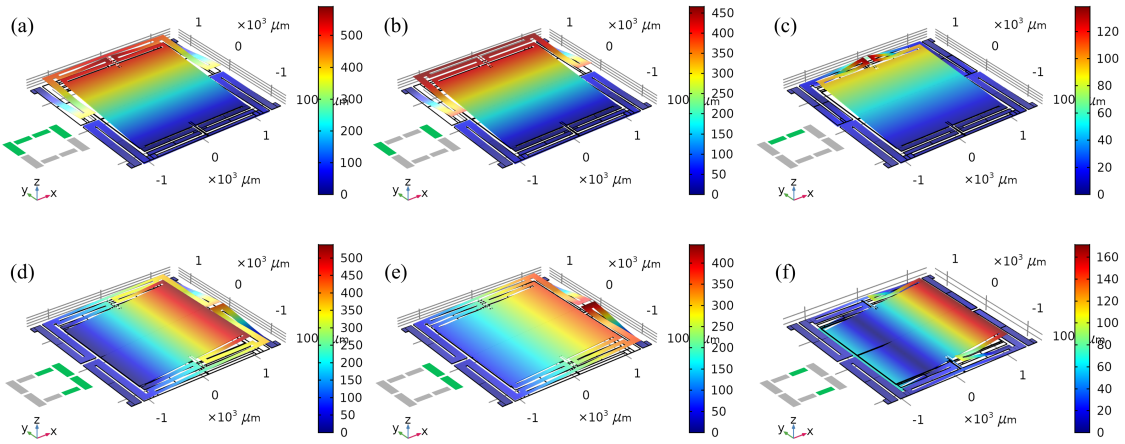

Figure 3.3: Total displacement profile of the scanner for various configurations of actuation. Pitch: (a) top inner and outer, (b) top outer, (c) top inner; Roll: (d) right inner and outer (e) right outer, (f) right inner.

tively. The AR bar reduced both roll motion by 17%, and coupling along Z-axis by 6%. The TS is introduced in the design to minimize the coupling in piston motion when driving the mirror in roll using inner legs. A voltage of 10 V was applied to the inner-right legs. The displacements along roll- and piston-axis for designs with and without TS are 6.9° and 6.16°, 50 µm and 122 µm, respectively. The TS increased roll motion by 12%, and reduced the coupling along Z-axis by 59%.

3.5.2 Static and Eigen frequency analysis

In the previous section we just saw that AR bar and TS spring were effective in reducing the coupling in along Z-axis when MEMS is driven in X-axis. We next perform static FEA simulations of our design. The same FEA model as described in previous section was used with actuation voltage of 10 V for the legs that were actuated. The total displacement of the scanner when various sets of legs are actuated is shown in fig. 3.3(a)-(f). The legs that are actuated are highlighted in green color in the inset of each figure. Comsol's default linear solver was used to perform the simulations. The angular displacements of 11.33°, and 2.57° in pitch; 8.67°, and 6.9° in roll are obtained when outer and inner legs are actuated, respectively. When both inner and outer legs are actuated simultaneously, the displacement is just a linear combination of individual cases.

An eigen frequency analysis was performed to check the modes of vibrations. The first three modes are shown in fig. 3.4(a)-(c). The piston, pitch and roll motions were observed at frequencies 70 Hz, 101 Hz, and 122 Hz, respectively. The relatively low

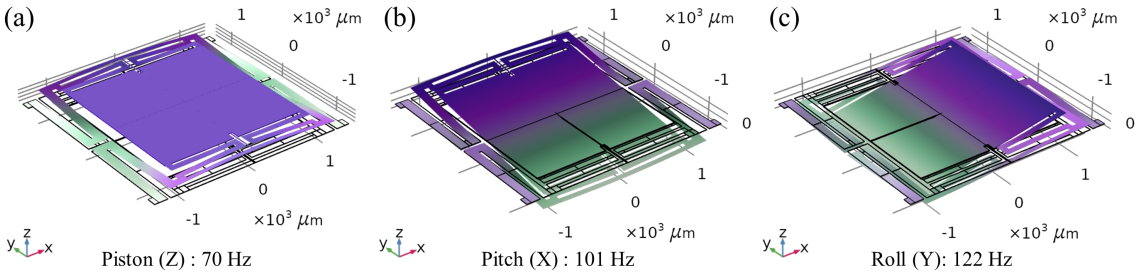

Figure 3.4: Eigen frequency analysis of the MEMS scanner showing first three vibration modes - piston, pitch and roll motion at 70 Hz, 101 Hz, and 122 Hz, respectively.

bandwidth of scanner is due to the larger mirror size that increases inertial mass. Higher order modes may be exploited for application requiring larger bandwidth.

3.6 Fabrication process

The MEMS device can be fabricated either on bare Si or SOI wafer. The SOI wafer, though expensive, gives more controlled backside etch. Here we describe fabrication process for silicon wafer, and same can be used for SOI wafer with slight modification. We start by ethching silicon dioxide trenches for the support structure framework into a silicon wafer using deep reactive-ion etching (DRIE). These high aspect-ratio trenches are filled by tetraethyl orthosilicate (TEOS) silicon dioxide and the top surface is planarized by chemical mechanical polishing (CMP). If required, the TEOS deposition and CMP are done repeatedly till the trenches are filled completely. A structural layer of 500 nm thick SiO_2 is deposited by a low-pressure chemical vapor deposition (LPCVD) process on both sides wafer and additional 1500 nm of PECVD oxide is deposited on the back side of the wafer. The wafer is then sent out to Radiant Inc., for PZT stack deposition. Radiant uses a 40 nm seed layer of titanium oxide to deposit 150 nm of PT to form bottom electrode (BE). Thin film PZT of 1 µm is deposited using sol-gel method followed by sputtering 150 nm of Pt for top electrode (TE).

After receiving the wafer from Radiant Inc., we pattern PZT stack using ion milling by three mask process.First, TE is patterned, followed by etching stack of PZT and BE, and finally by opening via in PZT layer to access BE. We can use an optional layer of 1 µm thick parylene to encapsulate the edges of the legs to avoid potential delamination of the TE Pt layer. We deposit 1 µm thick Al layer using physical vapor deposition (PVD), followed by lift-off, to form bend-down section on legs,bond pads and reflector surface. The mirror, actuator legs, and frame geometry are patterned by

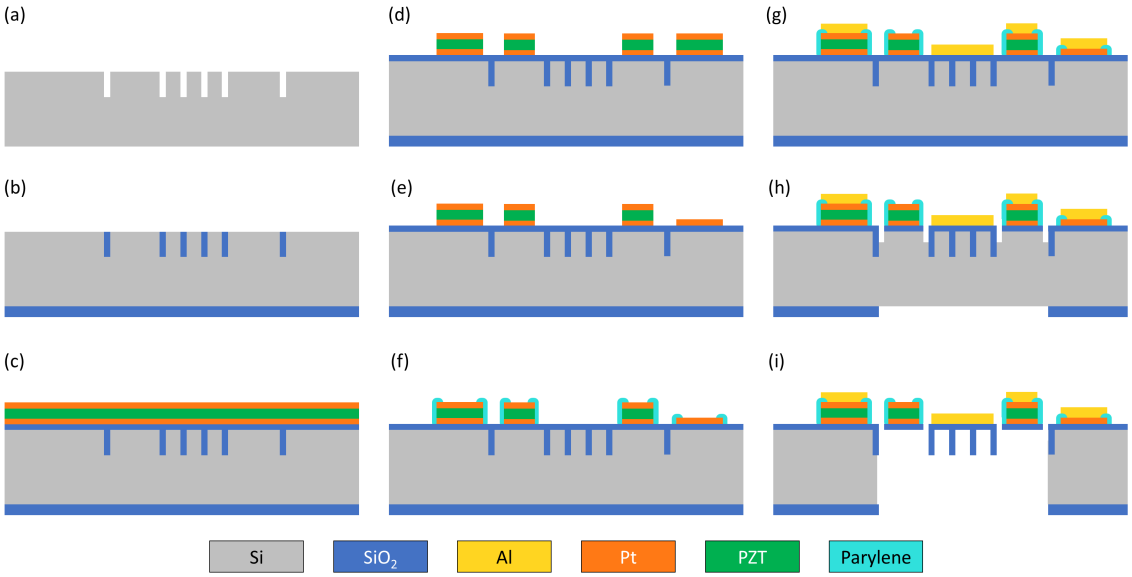

Figure 3.5: (a) 2 µm wide and 30-40 µm deep trenches made on single crystal Si wafer using DRIE, (b) Trenches are refilled with SiO_2 using TEOS process and excess SiO_2 from top side removed by CMP. (c) 500 nm thick SiO_2 is deposited using PECVD process followed by thin film PZT stack deposited consisting of 40 nm seed titanium oxide layer, 150 nm thick Pt bottom electrode (BE), 1 um PZT, and finally 150 nm thick Pt as a top electrode (TE). (d) Ion milling is used to pattern TE, and PZT and BE stack together using another lithography mask. (e) Via to BE is opened by etching PZT layer to form bottom bond pads. (f) The PZT stack on leg structure and top bond pad are encapsulated by depositing and patterning parylene. (g) 1 µm thick Al layer is deposited by lift-off process. (h) The top side SiO_2 layer is etched by RIE followed by short DRIE to go deeper in the Si layer. Another mask is used to pattern bottom SiO_2 for subsequent DIRE. (i) Device is released by a backside DRIE of Si followed by cleaning in acetone, IPA bath and drying in air/hotplate.

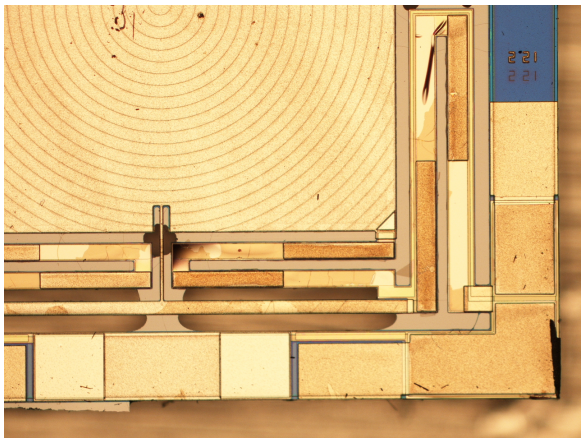

Figure 3.6: Image of a sample PZT device under fabrication

RIE of SiO_2 layer followed by a shallow DRIE of Si. Finally, the backside Si is etched by patterning oxide layer, which serves as a hard mask, followed by DRIE process. Figure 3.6 shows photograph of a sample PZT device almost completely etched from backside. The devices are unmounted by soaking in an acetone bath followed by isopropyl alcohol (IPA).

3.7 Conclusion

In this chapter, we proposed a novel thin film PZT MEMS scanner design with separate inner and outer actuation legs. The scanner is designed to minimize the coupling between various degrees of freedom it has. Simulations showed the AR bar was effective in minimizing the pitch motion on asymmetric actuation that could occur due intrinsic properties, fabrication tolerances, and residual stress in the material layers. The torsional spring reduced the displacement along Z-axis when scanner is driven in roll motion. The static displacement in piston, roll and pitch direction are sufficiently large for endomicroscopy application. The MEMS scanner can be used in both DC and resonant mode where bandwidth was observed to limited by the large mirror surface.

CHAPTER IV

Image Processing Metrics for Phase Identification in a Multi-axis MEMS Scanner

In this chapter, we apply image processing metrics to tracking of perturbations in mechanical phase delay in a multi-axis microelectromechanical system (MEMS) scanner. The compact mirror is designed to scan a laser beam in a Lissajous pattern during collection of endoscopic confocal fluorescence images, but environmental perturbations to the mirror dynamics can lead to image registration errors and blurry images. A binarized, threshold-based blur metric and variance-based sharpness metric are introduced for detecting scanner phase delay. Accuracy of local optima of the metric for identification of phase delay is examined, and relative advantages for processing accuracy and computational complexity are assessed. Image reconstruction is demonstrated using both generic images and sample tissue images, with significant improvement in image quality for tissue imaging. Implications of non-ideal Lissajous scan effects on phase detection and image reconstruction are discussed.

4.1 Introduction

Imaging by scanning a laser beam has many applications in biomedical imaging [58], scanning probe microscopy [59], 3D printing [60], single pixel cameras [36], scanning electron microscopy (SEM), laser scanning based projectors [61], and LiDAR (light detection and ranging). Various beam steering patterns, such as raster, spiral, and Lissajous, can be chosen depending on the application and scanning actuator capabilities. For instance, Lissajous scanning is obtained when both axes of motion are operated with constant sinusoidal inputs of differing frequency and phase [62]. The scan pattern has a direct effect on image resolution, field-of-view (FOV), and frame rate (FR). Lissajous scanning is a popular choice in imaging applications as it can be easily implemented using galvo mirrors or, especially, miniaturized MEMS (microelectromechanical system)-based scanners. For many scanning actuators, a large

FOV can be achieved by operating the scanner near resonant frequencies. Unlike raster scanning, Lissajous does not require the two operating frequencies to be widely separated, simplifying the MEMS design.

However, the effectiveness of a Lissajous scan and accuracy of image reconstruction is very sensitive to the phase of the axes. In miniaturized devices, such as MEMS mirrors, the resonant frequency of a scanner (i.e. resonant micro-mirror) can drift by several degrees of phase angle due to environmental perturbations. This drift, in turn, produces a change in phase delay between mirror motion and the periodic input driving signal. There has been limited analysis of phase compensation as a mechanical phenomena in Lissajous scanning, as distinct from other phase information that may be compensated during imaging, such as focal depth or wavefront geometry. Previous methods for compensating for mechanical phase shift in resonant devices include temperature-based calibration [63], on-chip capacitive sensing [64], and design to limit temperature sensitivity, but these suffer from poor repeatability, poor signal-to-noise ratios, and material limitations when using small MEMS devices in severely space-constrained applications such as endoscopy. Various feedback controllers have also been proposed [65]–[67], but these are also susceptible to sensing limitations in small, in vivo instruments and they increase system complexity. Most recently, information from the spatial Fourier transform of image information was proposed for MEMS mirror phase identification, but this requires substantial computation and tracked only small perturbations in phase [68].

This work proposes methods for high-accuracy mechanical phase detection using (i) an image sharpness-based variance metric, (ii) an image blur-based threshold metric; the latter metric relies on binary pixel counting from thresholded intensity data during Lissajous scanning. Sharpness-based metrics comparable to (i) are often used in other autofocus applications [69]. Blur-based algorithms similar to (ii) were first proposed as criteria during development of early autofocus techniques for microscopy [70]. However, we demonstrate the first application (to the best of the authors' knowledge) of these classes of criteria to the problem of mechanical phase tracking encountered by multi-axis MEMS scanners. Moreover, while the approach of thresholded pixel counting as in the blur metric has not been widely adopted as an autofocus criteria because the value for an optimal focusing parameter (i.e. focal depth) can vary with threshold level [71], we will show that it is much less sensitive to this limitation under the conditions of Lissajous scanning, with accompanying advantages for computation time.

In this research, we thus demonstrate that variance and thresholded pixel count

metrics are well-suited to the compensation of unknown phase perturbations in Lissajous scanning with MEMS mirrors, with some trade-offs between them for robustness of parameter selection versus computational efficiency. In addition, we will discuss how these phase detection algorithms interact with other potential limitations of Lissajous scan design, such as fill factor (FF) versus frame rate and non-uniform scan density, and will suggest practical approaches for managing these trade-offs for the MEMS scanner. Sample images from a fluorescent confocal endomicroscope using a 2-axis parametrically-resonant micro-mirror are presented.

4.2 Scanner model and phase drift

To begin, we examine the interaction of MEMS mirror dynamic perturbations with Lissajous-scan image reconstruction. The model for scanner dynamics in each axis of a two-axis parametrically-resonant MEMS scanner, such as shown in fig. 4.1(a), are described following [72] by

$$J_k\ddot{\theta}_k + c_k\dot{\theta}_k + K_k\theta_k = -\frac{d_k}{b_k}\theta_k e^{-\frac{\theta_k^2}{b_k}}V_k^2$$

where subscript k denotes parameters for a respective axis (x or y), J is rotational inertia, c is a damping constant, K is a torsional spring stiffness, V is input voltage, and d and b are parameters approximating roll-off of capacitance between electrostatic comb fingers that actuator mirror motion as an exponential decay. Let the scanner be driven into motion about an axis with a driving voltage given by

$$V_k(t) = A_k \sin(2\pi f_k t + \psi_k), \tag{4.1}$$

where A_k is input amplitude, f_k is the driving frequency close to resonance of the x or y axis, and ψ_k is the phase of the driving voltage applied to the electrodes of different axis. The angular motion of scanner along the respective axis, and the laser position (x, y) on the object plane can be closely approximated as

$$\theta_k(t) = D_k \sin(\pi f_k + \psi_k + \phi_k(t)), \tag{4.2}$$

$$(x(t), y(t)) = (L\theta_x(t), L\theta_y(t)). \tag{4.3}$$

Here, D_k is the peak amplitude of the mirror motion, $\phi_k(t)$ is the phase difference between scanner motion and input voltage at the current driving frequency, and L is

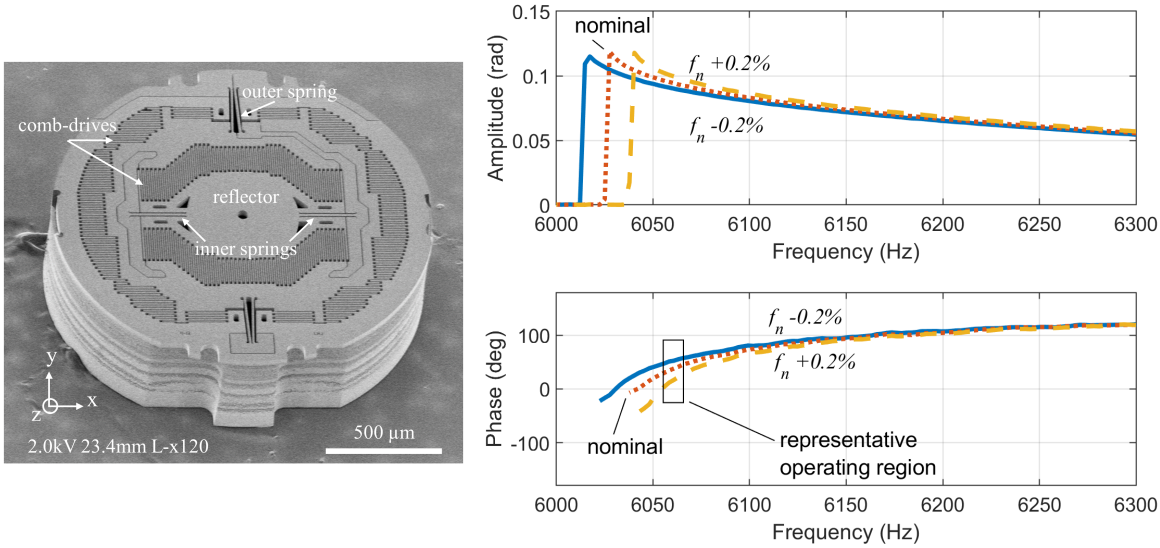

Figure 4.1: (a) A 2-axis electrostatic actuated parametrically-resonant MEMS scanner, (b, c) Phase delay variation near maximum amplitude scanning is substantial with small perturbations of natural frequency. Sample frequency response generated by methods from [72], [73], with nominal $J_x = 0.013$ mg-mm^2, $c_x = 0.003$ µN-mm-s/rad, $K_x = 4860$ µN-mm/rad, $b_x = 0.0006$ rad^2, $d_x = 0.003$ µN-mm-rad, and corresponding linear natural frequency, f_n, of 6405 Hz perturbed by adjusting K_x

the distance from the mirror to the focal point of the laser being scanned. Note that the scanner oscillates at half the frequency of the input voltage due to parametric resonance as described in [72].

In fluorescence endomicroscopy, the distance of an instrument from a tissue sample is not precisely controlled, and thus the exact FOV of the image, $(\pm LD_x, \pm LD_y)$ is neither expected to be exactly known, nor critical to producing a clear image, so long as the tissue surface is within the working distance of the instrument. Thus, perturbations to mirror dynamics affecting motion amplitude are of limited importance. However, perturbations to the mechanical phase difference between scanner input and motion output will rapidly degrade image quality if changes in delay cannot be identified.

To elaborate, an image can be reconstructed if one knows the trajectory of the laser beam on the object plane as a function of time. As described by eqs. (4.2) and (4.3), the beam motion depends on parameters f_k , ψ_k , $\phi_k(t)$, and $\frac{D_x}{D_y}$. In practice, f_k, and ψ_k are known, and as noted above $\frac{D_x}{D_y}$ has comparatively modest impact on image quality.

Phase information ϕ_k, however, can be a major contributor to image misregistration. Mechanical phase drifts in one or both axes can be attributed to numerous factors such as variation in environmental conditions including temperature, changes

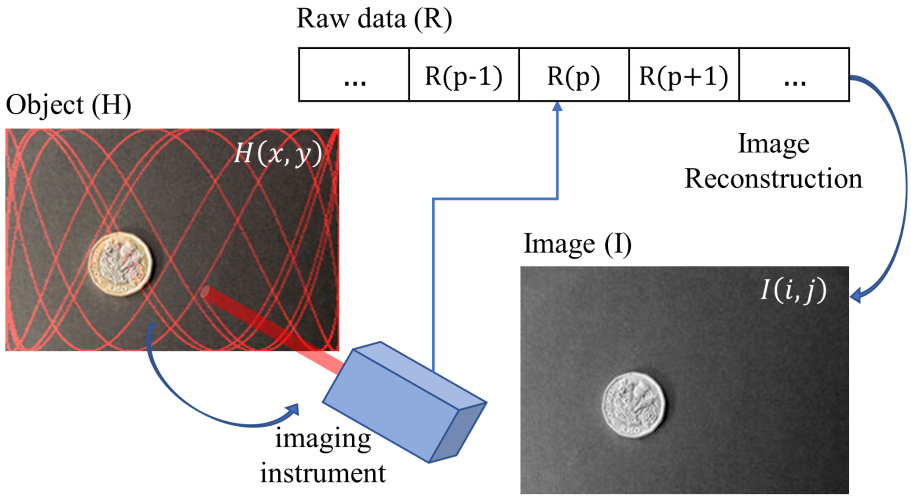

Figure 4.2: Schematic for image reconstruction in a single pixel scanning camera. (Image credits: ID 90250929 ©Jevanto | Dreamstime.com)

in material property over time, etc, with sample behavior shown in fig. 4.1(b, c). This makes the phase $\phi_k(t)$ a slow function of time and creates difficulty in image reconstruction. There is also the possibility of dynamic coupling of axes, but this can be mitigated in parametrically-resonant scanners by ensuring that the natural frequencies of the two axes are sufficiently far from an integer multiple of one another, as by design procedures discussed in [36]. The phase $\phi_k(t)$ can be experimentally determined in a controlled lab environment to reconstruct the image. However, in practical application, the phase determined in the lab will not remain constant indefinitely. It is sometimes possible to adjust the phase manually to compensate the drift for sparse images. However, this requires substantial user experience and it becomes almost impossible to adjust the phase for images of structures that are new to the user. Thus, there is a need to determine the correct phase at a regular interval of time with minimal disruption to the endoscopy procedure.

4.3 Lissajous scan image reconstruction

To generate a grey scale imaging via single point scanning, points $(x(t), y(t))$ on an object H are sequentially sampled at constant sampling frequency $f_s = \frac{1}{T}$ (T is sampling time). The intensity of light, $H\left(x(pT), y(pT)\right)$, from p^{th} point is stored as data sample $R(p)$. By this process, the 2D image of an object $H(x, y)$ is translated into 1D time series data $\boldsymbol{R}$, referred to as raw data henceforth. The sequence of sampled points (x, y) on the object plane H is determined by the Lissajous scanning

pattern given by eqs. (4.2) and (4.3), where $t = pT$, and $p \in N$. Image reconstruction becomes an inverse problem where one must map intensity values $R(p)$ to a 2D image space (discrete) $I(i, j)$, where $\boldsymbol{I}$ is a grey image ($M \times N$ matrix) of an object H. Thus, it is essential to know each ordered pair (i, j) as a function of p.

The mapping of $\boldsymbol{R}$ to $\boldsymbol{I}$ is many-to-one because of non-uniform scan density (the number of data points sampled per unit area) over the FOV and rounding of the location of sample instance to the nearest pixel location. One way to get a unique intensity value at a pixel (i, j) is to average all such values of $R(p)$'s that are mapped to that pixel. The schematic for the process of object scanning and image reconstruction is shown in fig. 4.2 and summarized by the calculations:

$$i = \lceil M\hat{x}(p) \rceil \tag{4.4}$$

$$j = \lceil N\hat{y}(p) \rceil. \tag{4.5}$$

Where $\lceil\ \rceil$ denotes a greatest integer function (ceiling), and $\hat{x}(p)$ and $\hat{y}(p) \in [0, 1]$ are the normalized co-ordinates given by

$$\hat{x}(p) = 0.5 \sin\left(\pi f_x pT + \psi_x + \phi_x(pT)\right) + 0.5 \tag{4.6}$$

$$\hat{y}(p) = 0.5 \sin\left(\pi f_y pT + \psi_y + \phi_y(pT)\right) + 0.5. \tag{4.7}$$

A key characteristic of the impact of drift on image reconstruction is duplicative appearance of features along each axis when pixels are misregistered due to erroneous phase used for reconstruction. As illustration, consider that a given $(\hat{x}, \hat{y})$ from eqs. (4.6) and (4.7) is also satisfied by

$$\hat{x}(p) = 0.5 \sin\left(\pi - \pi f_x pT - \psi_x - \phi_x(pT)\right) + 0.5 \tag{4.8}$$

$$\hat{y}(p) = 0.5 \sin\left(\pi - \pi f_y pT - \psi_y - \phi_y(pT)\right) + 0.5 \tag{4.9}$$

Under conditions of phase uncertainty, the phase $\phi_k(t)$ can be written as

$$\phi_k(t) = \phi_k^o + \Delta\phi_k(t), \tag{4.10}$$

where ϕ_k^o is a constant and $\Delta\phi_k(t)$ is phase drift. When $\Delta\phi_x = \Delta\phi_y = 0$, all intensities assigned to a pixel (i, j) are obtained from the same, correctly-registered, point in the FOV. However, non-zero phase drift assigns intensity measurements to either side of the nominal pixel location.

To demonstrate the resulting effect, we generate a set of raw data by sampling

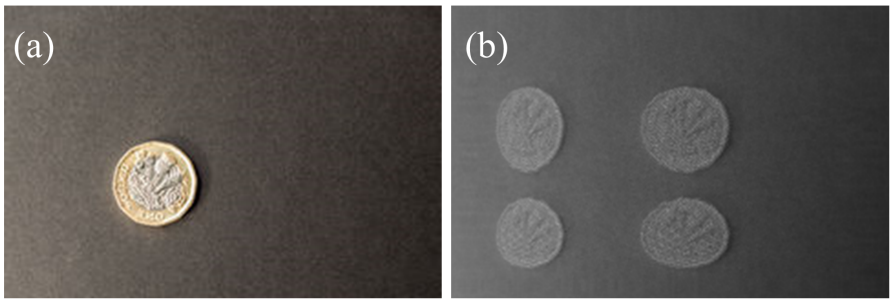

Figure 4.3: Impact of phase error on imaging. (a) Original image, (b) image reconstructed with phase error $\varphi_x = \varphi_y = \pi/8$ rad.

the demonstration image, shown in fig. 4.3(a), in Lissajous style. Arbitrary scanning frequencies and phases of $f_x = 19251$ Hz, $f_y = 3315$ Hz, and $\phi_x = 2.8456$ rad, $\phi_y = 0.3989$ rad were chosen to simulate the laser scan pattern. A total of 10^6 samples were recorded assuming a sampling rate of 10^7 samples/sec. The location of the simulated laser point at any sampling instance was rounded to the nearest pixel location.

If we introduce an exaggerated error or drift of $\frac{\pi}{8}$ rad for phases in both axes ($\Delta\phi_x$ and $\Delta\phi_y$), the reconstructed image will have four overlapping images as shown in fig. 4.3(b). As a consequence of eqs. (4.6) to (4.9), we can say the output image is an overlap of four original images offset by corresponding phase of $\Delta\phi_x$ and $\Delta\phi_y$ in each axis. Moreover, the offset between right and left scan images is not a linear function of $\Delta\phi$ as it is mapped via the sinusoidal functions above. This demonstration gives an exaggerated view of a problem, but even a small error in phase leads to a blurry image, significantly affecting image resolution. This puts a stringent requirement on the accuracy with which the phases should be predicted or detected.

4.4 Phase estimation using image-based metrics

Autofocusing techniques regularly rely on metrics drawn from image properties to perform an optimization on an autofocus parameter. A common example is metrics for sharpness, frequently defined based on pixel variance within an image [74]. Estimation of the phase delay ($\boldsymbol{\phi}^*$) under a metric is an optimization problem where the estimated value is the argument of a minimization or maximization problem, i.e.

$$\boldsymbol{\phi}^* = \arg \min_{(\phi_x, \phi_y)} g(\phi_x, \phi_y), \tag{4.11}$$

where, the objective function $g(\phi_x, \phi_y)$ can be any combination of metrics expected to improve the image quality upon optimization. As established in section 4.3, the phase error in each axis independently produces the effect of overlapping images. Thus, optimizing the objective function $g(\phi_x, \phi_y)$ with respect to two variables ϕ_x and ϕ_y simultaneously can be an overkill and computationally expensive. We simplify eq. (4.11) with the independent assumption and rewrite as

$$\boldsymbol{\phi}^* = \arg\min_{\phi_y} \min_{\phi_x} g(\phi_x, \phi_y), \tag{4.12}$$

and perform a sequential optimization starting arbitrarily with either ϕ_x or ϕ_y.

Conceptually a variety of autofocus-type algorithms could be applied to this problem, with most such algorithms depending on metrics such as intensity variance or properties of spatial Fourier transform. However, these are comparatively computationally expensive and can be implemented only after fully reconstructing the image for each candidate phase angle. Motivated by this characteristic impact of phase drift on Lissajous image reconstruction, we instead first describe our method for rapidly assessing image blur when using a MEMS micro-scanner. We will then introduce a variance-based approach in section 4.4.2 for comparison, which is more similar to widely-used autofocus metrics from other applications, though implemented in MEMS scanner phase tracking for the first time.

4.4.1 Threshold-based blur metric

We propose a threshold-based blur metric that functions as a "shorthand" method to signify the amount of repetition in the image with low computational complexity. In this method, a threshold (σ, constant for a given phase detection step) is used to convert the time series raw data $\boldsymbol{R}$ to a binary vector, $\boldsymbol{R}_\sigma = \{0, 1\}$. Then, all pixels within the image are assigned a binary value, $I_B(i, j)$, with value equal to one if entry in $\boldsymbol{R}_\sigma$ assigned to a pixel (i, j) under a candidate phase estimate is a one. This can also be written

$$\boldsymbol{I_B}(i,j) = \begin{cases} 0, \forall \lceil M\hat{x}(p) \rceil = i, \lceil N\hat{y}(p) \rceil = j : H(x,y) < \sigma \\ 1, \exists \lceil M\hat{x}(p) \rceil = i, \lceil N\hat{y}(p) \rceil = j : H(x,y) \geq \sigma \end{cases} \tag{4.13}$$

In other words, if at any instance during reconstruction a pixel is assigned an intensity greater than the threshold, it takes on a value of 1. The final normalized blur metric, B, is then defined as the total number of white pixels in the B/W image, (i.e. sum

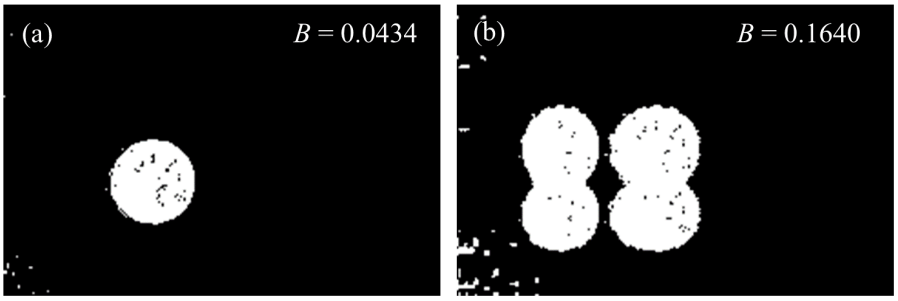

Figure 4.4: Demonstration of intuition behind threshold metric, the value of the threshold metric B (number of bright pixels) increases from 0.0434 to 0.1640 with increase in phase error from 0 to 0.075π for (a) and (b) respectively.

of all ones) divided by the total number of pixels

$$B = \frac{\sum_i \sum_j \boldsymbol{I_B}(i,j)}{NM} \tag{4.14}$$

Conceptually, the rationale behind eq. (4.14) is that when an inaccurate phase is used to generate the image, the information is spread across the image, and ones (or bright pixels) will be spread across the image and increase the value of B. An exaggerated phase error example is demonstrated in fig. 4.4. For B to serve as an indicator of phase, we desire B to be a minimum when $\Delta\phi_x = \Delta\phi_y = 0$. To do this, we assume that

(i) σ is selected according to

$$\min(\boldsymbol{R}) < \sigma < \max(\boldsymbol{R}) \tag{4.15}$$

(ii) there exist non-empty sets of pixels with $R(p) < \sigma$, and $R(\tilde{p}) > \sigma$ that are oversampled during the Lissajous scan period of interest.

Under these assumptions, if the image is correctly registered (i.e. $\Delta\phi_x = \Delta\phi_y = 0$), there will be finite numbers of both one and zero entries in $\boldsymbol{I_B}$, and associated boundaries between "black" and "white" regions in the binarized image. As phase error increases, the number of white pixels increases due to pixels in the black regions drawing samples from the white regions due to eqs. (4.6) to (4.9) and the asymmetric thresholding conditions of eq. (4.13). Critically, due to eqs. (4.6) to (4.9) and assumption (ii), the number of white pixels must increase for perturbations of $\Delta\phi_x$ and $\Delta\phi_y$ in either direction, and $\Delta\phi_x = \Delta\phi_y = 0$ will be at least a local minimum.

The critical result for this method is that the combination of, oversampling and

locally-symmetric misregistration characteristic of Lissajous scanning prevents the minimum value of B from being dependent on threshold value, so long as assumption (i) is satisfied. Thus, this approach is highly-suitable for phase correction in Lissajous scanning despite application to other autofocus scenarios being less effective. Furthermore, the approach requires less computational effort than more conventional autofocus techniques. While binarized pixels do need to be assigned to locations in image space based on candidate phase delays, minimal additional computation is required to calculate B, as opposed to full computation of reconstructed image properties by metrics such variance or spatial frequency calculations.

A limitation of the metric in eq. (4.14) is that a global search is not proven to be robust and not guaranteed to provide the correct optimum value for all possible selections of the threshold. However, as will be examined in the following section, we have observed to date that the blur metric is always at least locally minimized at ϕ_k^*, regardless of the choice of the threshold value.

4.4.2 Variance-based sharpness metric

In this method, a variance-based sharpness metric is used to predict the phase. This metric is inspired by other autofocus applications and adapted to MEMS scanner phase tracking as a comparison for the more specialized approach above. In a sharp image, the pixel intensity values are well separated and thereby increase the variance of pixel intensities. Thus, the variance of pixel intensities can be a sharpness metric, S, in this case using pixel intensity of an image reconstructed from a test phase delay,

$$S = \frac{1}{MN} \sum_{i}^{M} \sum_{j}^{N} \left(I(i,j) - I_{avg} \right)^2 \tag{4.16}$$

$$I_{avg} = \frac{1}{MN} \sum_{i}^{M} \sum_{j}^{N} I(i,j). \tag{4.17}$$

Such that optimal phase is selected based on eq. (4.12) with $g = -S$.

4.5 Results

In this section, we examine the results of the proposed phase detection algorithm through application to a set of test images and images acquired from in vivo endomicroscopy. We will compare effectiveness of both metrics proposed in section 4.4 in

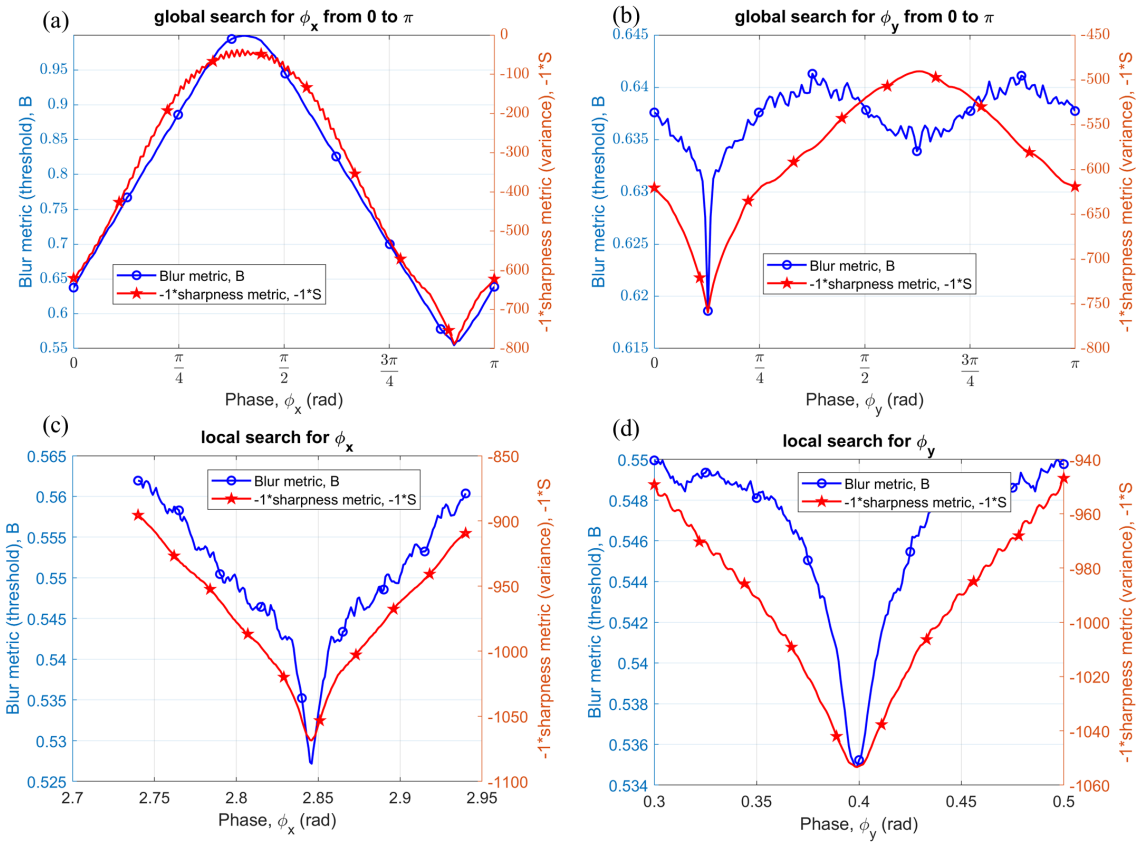

Figure 4.5: Plots of threshold and negative variance metric vs phase x and y; (a) and (b) global search from 0 to π, (c) and (d) local search around initial approximation given by global search.

Table 4.1: Sample image result comparison

	ϕ_x (rad)	$\delta\phi_x$ (mrad)	ϕ_y (rad)	$\delta\phi_y$ (mrad)
True phase	2.8456	0	0.3989	0
Estimated phase				
• threshold metric	2.8460	0.4	0.3980	-0.9
• variance metric	2.8460	0.4	0.3980	-0.9

estimating the phase. The effect of phase error on the image quality can be assessed by using a target error previously established [75]. Let the maximum uncertainty in intensity location that produces acceptable image quality be δr. Then, in an image size of $M \times N$, the error in estimation of a phase ($\delta\phi_k = \hat{\phi}_k - \phi_k$) along respective axes is upper bounded by,

$$|M\delta\phi_x| \leq |2\delta x|, \text{and } |N\delta\phi_y| \leq |2\delta y|. \tag{4.18}$$

Where the uncertainty in intensity location $\delta r^2 = \delta x^2 + \delta y^2$.

4.5.1 Phase correction implementation using global and local search

The simulated raw data described in section 4.3 is first used as a demonstration of the proposed blur versus sharpness-based phase prediction methods. A global search was made independently along x and y axes by evaluating either metrics at each candidate phase between $[0, \pi]$ incremented in step of 0.02 rad. In fig. 4.5(a)-(b) the global minimum can be seen at the true phase values. The results were fine-tuned by a local search where phase was incremented in steps of 1 mrad in the vicinity of the minimizer obtained from the global search. The results can be seen in fig. 4.5(c)-(d). The comparison of the predicted phase by both methods with the true phase is given in table 4.1.

4.5.2 Algorithm testing on simulated data using generic images

The effectiveness and versatility of the phase detection algorithm and proposed metrics is next evaluated by testing it on several images. For demonstration purpose, results for both biological images such as a widefield endoscopic image of human colon, confocal microscopic image of sessile serrated (SS) adenoma tissue and normal tissue from human colon, and couple of images commonly used in the image processing community like 'chemical plant', and 'lake', are shown in fig. 4.6. These images

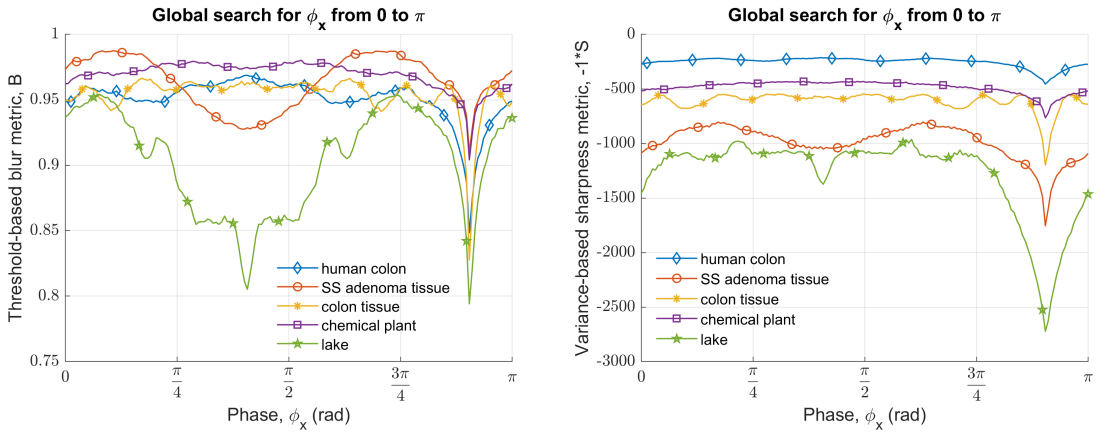

(a) blur metric

(b) negative sharpness metric

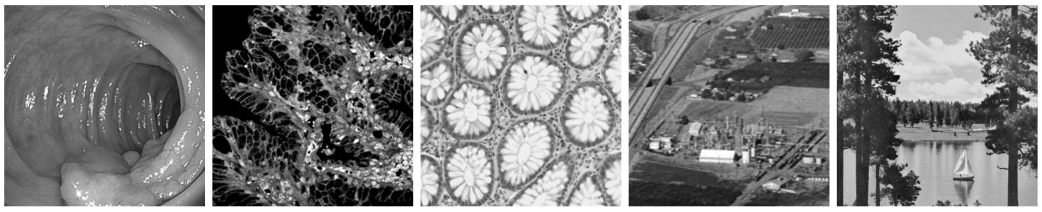

(c) (left to right) human colon, confocal microscopic image of sessile serrated (SS) adenoma tissue and normal tissue from human colon, chemical plant, and lake

Figure 4.6: Plots of global search sweep along x axis from 0 to π for standard test images

were first converted to grayscale and resize to 256x256 pixels. Raw data for each image was generated by simulating Lissajous scanning as described in section 4.3. For comparison, we used the same arbitrary scanning frequencies and phases of $f_x = 19251$ Hz, $f_y = 3315$ Hz, and $\phi_x = 2.8456$, $\phi_y = 0.3989$ rad to simulate the laser scan pattern for each image. Global and local search, as mentioned in section 4.5.1, were performed using Matlab to predict the phase value and results are shown in fig. 4.6 and summarized in table 4.2. As evident from the results, the algorithms successfully predict the phase value with maximum absolute error of 0.6 mrad. The accuracy could be further improved by reducing the step size of 1 mrad used during the local search. To put this error in a perspective, in view of eq. (4.18), for $M = N = 256$ pixels, $|\delta\phi| = 0.6$ mrad, the maximum possible pixel shift is $\delta r \approx \pm 0.1086$ pixel. In other words, the maximum error in the inferred location of an intensity value is less than 10.86% of a pixel dimension.

4.5.3 Tissue imaging demonstration

The effectiveness of the algorithm was applied to a two-axis MEMS scanner installed in a front-view single-axis confocal endomicroscope during *in-vivo* imaging [6]. The animal study was approved by the University Committee on the Use and Care

Table 4.2: Phase and error estimation in test images

	Threshold metric		Variance metric	
	$\delta\phi_x$ (mrad)	$\delta\phi_y$ (mrad)	$\delta\phi_x$ (mrad)	$\delta\phi_y$ (mrad)
Human colon	0.4	0.1	0.4	0.1
SS adenoma tissue	0.4	0.1	0.4	0.1
Colon tissue	0.4	0.1	0.4	0.1
Chemical plant	0.4	0.1	0.4	0.1
Lake	-0.6	0.1	0.4	0.1

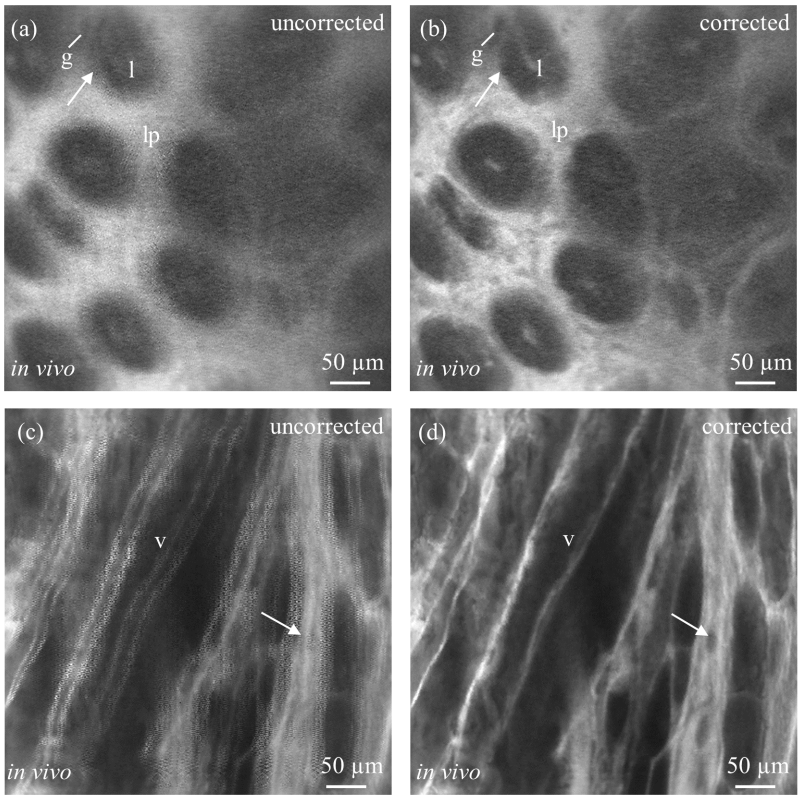

Figure 4.7: (a, b) Comparison of in vivo fluorescence images before and after phase correction. A normal colonic mucosa from a mouse was imaged. Individual crypts (arrow), including glands (g), lumen (l), and lamina propria (lp), could be identified in the corrected image. (c,d) A saphenous vein from the hind limb of a mouse was imaged. Individual vessels (v) and blood cells (arrow) could be identified in the corrected image. Contrast was provided by intravenous injection of fluorescein.

of Animals (UCUCA) at the University of Michigan. During imaging, the mouse was anesthetized with inhaled isoflurane. Fluorescein sodium at a concentration of 5%, 200 µL was administered intravenously into the tail vein of a nude mouse to generate contrast. Fluorescence images were collected at 10 and 25 fps from the mucosal surface of the colon and the hind limb, respectively (fig. 4.7). The probe was placed in

Table 4.3: Phase and error estimation for in-vivo images

	Mouse colon $f_x = 27680$ Hz, $f_y = 6540$ Hz			Mouse hind limb thigh $f_x = 24200$ Hz, $f_y = 5650$ Hz		
	Lab-setting	Threshold	Variance	Lab-setting	Threshold	Variance
$\hat{\phi}_x$ (deg)	17.143	19.710	19.824	9	11.516	11.459
$\Delta\hat{\phi}_x$ (deg)	–	2.567	2.681	–	2.516	2.459
$\hat{\phi}_y$ (deg)	11.543	12.834	12.949	1.8	1.375	1.490
$\Delta\hat{\phi}_y$ (deg)	–	1.291	1.406	–	-0.425	-0.310

contact with the tissue surface and was moved manually across the area of interest.

The scanner in the probe used for mouse colon imaging had parametric resonance at f_x= 27680 Hz, f_y= 6540 Hz. The phase of $\phi_x = 17.143$ deg, $\phi_y = 11.543$ deg were identified by using a generic fluorescence target before the *in-vivo* experiment. LabVIEW was used for real-time *in-vivo* imaging, and it is hypothesized that the MEMS scanner experienced phase shift due to environmental variation, producing blurred images shown in fig. 4.7(a). Environmental factors, such as temperature variations and mechanical stress were most likely to be the cause of phase perturbations. Phase correction was performed offline using LabVIEW and the estimated phase values are tabulated in table 4.3. The estimates by both the metrics agree with each other. During the implementation of algorithm the problem of missing pixels, as discussed in section 4.6.1, was tackled by reconstructing the image at reduced size during global search, however, for the local search full size image was used. Remaining missing pixels were filled using moving median with window size of 5 pixels.

Representative improvements in image quality after phase correction using threshold metric can be seen in fig. 4.7(b). The image produced using variance metric has no appreciable difference compared to fig. 4.7(b), and is not shown here in view of limited space. The fluorescence image of mouse hind limb thigh was taken at 25 fps using another probe with scanning parameters as mentioned in the table 4.3. The image (fig. 4.7(d)) after phase correction shows significant improvement in the image quality, for instance, blood cells (arrow) could be clearly identified. It can be concluded that the phase along the fast axis drifted by almost 2.5 deg for both the experiments, while the average phase drift along the slow axis is 1.345 deg and -0.367 deg in mouse colon and thigh imaging respectively. It should be noted that only these drifts in phase should correspond directly to changes in the underlying dynamics, while the absolute measures of phase may include additional delays due to data acquisition and pre-processing, unknown but considered fixed for a given hardware configuration.

4.6 Discussion

4.6.1 Effect of missing pixels

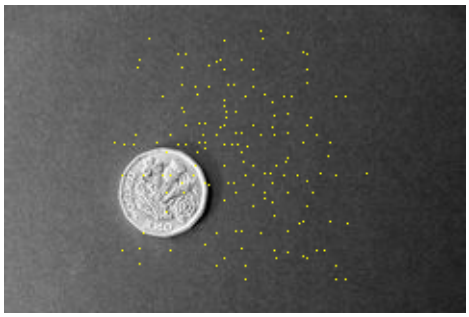

(a) High FR image with missing pixels

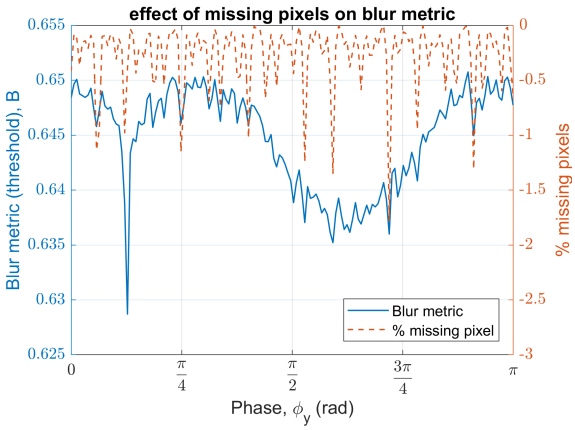

(b) threshold metric vs ϕ_y

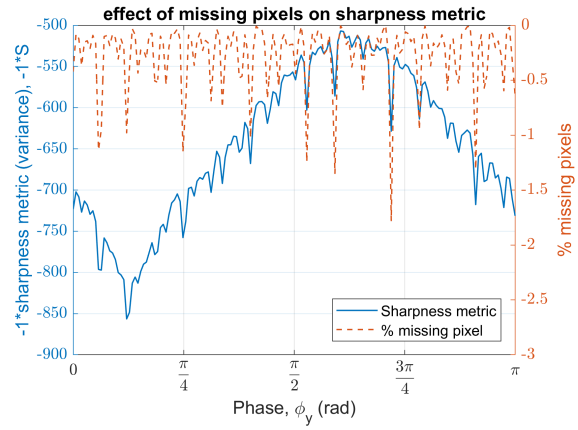

(c) variance metric vs ϕ_y

Figure 4.8: Demonstration of effect of missing pixels on the metrics.

We note that the Lissajous scan trajectory depends on driving frequencies and the relative phase difference between them. A repeating or non-repeating pattern is obtained depending on whether the ratio of driving frequencies, $\frac{f_x}{f_y}$, is a rational or irrational number, respectively. A non-repeating curve is often desired as different pixels are scanned in each cycle (i.e. one cycle of the lower frequency), thereby covering more area on the object plane and improving the fill factor (FF). FF can be defined as a ratio of the number of pixels scanned at least once to the total possible number of pixels in the image. In a high definition (HD) image, FF can be made sufficiently high by scanning for a long time, which results in lower frame rate. This leads to a trade-off between FR and FF; it is difficult to maximize both for an HD image. In a high FR application using Lissajous scan, it is inevitable to have some missing pixels in the reconstructed image. As a mitigating factor, various algorithms can be used to fill these missing pixels in a post-processing step after initial image

reconstruction, or an image with reduced size can be reconstructed. However, it is difficult to eliminate these missing pixels during the phase prediction as this step precedes all others.

As mentioned earlier a total of 10^6 samples were taken to simulate the raw data from the image in fig. 4.3(a), which is 26 times the total number of pixels in the image. These many samples were enough to reconstruct the image such that there are no missing pixels. However, to study the effect of missing pixels on blur and sharpness metric, we tested phase tracking using only quarter of total samples in the raw data i.e. the first 0.25 x 10^6 samples. The missing pixels are flagged by a separate color in the image reconstructed with true phase information as shown in fig. 4.8(a). The plot of the blur metric vs phase is shown in fig. 4.8(b) with a solid line. As compared to the fig. 4.5(b) this time the blur metric has more high frequency variation with respect to ϕ_y. The percentage of missing pixels in an image as a function of ϕ_y is plotted on the right y-axis of the plot given in fig. 4.8(b). As evident from the plot, the high frequency noise peaks in the blur metric match with the missing pixels. The sharpness-based phase prediction method will also suffer if the image has missing pixels as shown in fig. 4.8(c). In the extreme case, the phase prediction method may fail if the contribution of missing pixels to the sharpness metric exceeds the depth of the global minimum at the true phase.

4.6.2 Practical choice of threshold used for binarizing

As a practical matter, the algorithm works most effectively when the threshold (σ) is selected close to the mean of the raw data, i.e. when $\sigma = \bar{\boldsymbol{R}}$ because this approximately balances the count of zeroes and ones in binarized data. Selecting a smaller value for the threshold $\sigma \ll \bar{\boldsymbol{R}}$ increases the count of ones, and in the reconstructed image there will be some overlap of ones at all candidate phase. Thus, the sensitivity of the blur metric to the change in candidate phase is reduced. If ones are too sparse, i.e. $\sigma \gg \bar{\boldsymbol{R}}$, the blur metric is almost constant with respect to phase and has a very steep slope near the true phase value. As a result, true phase may be missed by discrete steps taken while sweeping candidate phase values.

4.6.3 Effect of binarizing before or after image reconstruction

In a threshold-based blur metric, there are two potential ways to binarize the data. First, the raw data $\boldsymbol{R}$ itself can be binarized to construct the B/W image using eq. (4.13) directly. Second, a grey image $\boldsymbol{I}$ can be made from raw data and

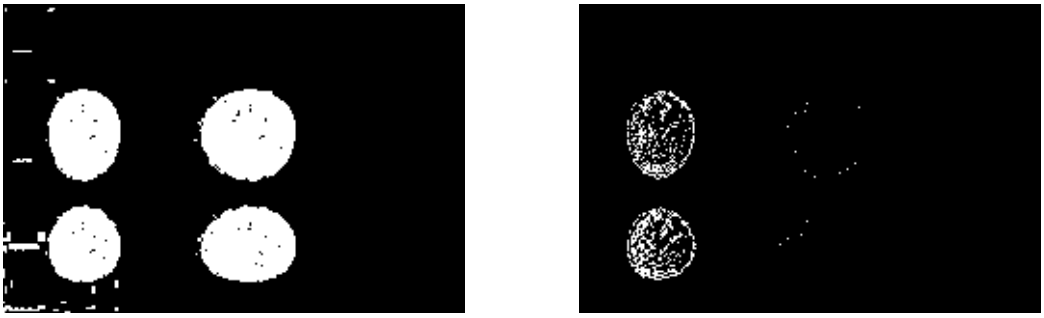

Figure 4.9: (a) A binary filter applied to raw data to obtain B/W image directly, (b) A binary filter applied to grey image constructed from raw data.

Table 4.4: Qualitative comparison of average computation time taken to evaluate a metric per test phase

	Threshold metric time (ms)	Variance metric time (ms)
Human colon	17.96	19.79
SS adenoma tissue	17.84	19.69
Colon tissue	17.29	19.21
Chemical plant	17.23	19.29
Lake	17.14	19.26
Mean	**17.49**	**19.45**

later binarized to a B/W image. In this section, we study the effect of binarizing the raw data $\boldsymbol{R}$ vs a grey image $\boldsymbol{I}$. fig. 4.9(a) represents the first case where raw data $\boldsymbol{R}$ is binarized using threshold values $\sigma = 1.6\bar{\boldsymbol{R}}$ and fig. 4.9(b) shows a grey image $\boldsymbol{I}$ binarized using threshold values $\sigma = 1.6\bar{\boldsymbol{I}}$. As seen from the fig. 4.9(a) all the pseudo images of the coin are preserved and remain evident on choosing an appropriate threshold value. While in case (b), some of the pseudo images of the coin are lost. Thus, it is important to binarize the raw data before the image is formed for better detection of phase with increased sensitivity.

4.6.4 Computation time comparison

In Lissajous scanning, to mitigate the missing pixels one need to oversample the object by an order of magnitude more compared to total number of pixels in the targeted image, as discussed in section 4.6.1. This poses a big challenge for phase prediction in real time imaging. The computation time to predict phase error using either sharpness or blur metric is dominated by the step in which enormous samples in a raw data $\boldsymbol{R}$ are mapped to respective pixel location for each test phase. As the memory location is not accessed sequentially due to Lissajous scanning, this becomes

the bottleneck in speeding up the algorithm. However, most operations in evaluating the blur metric are binary, because of eq. (4.13), making it faster compared to the sharpness metric in predicting the phase errors. We compared the time taken by both the methods in estimating the phase by performing a global search (158 test phases) on standard images with parameters same as described in sections 4.5.1 and 4.5.2. Matlab was used to run 12 iterations of the global search on a machine having 8GB RAM, Intel(R) Core(TM) i7-7700HQ CPU, 2.80GHz, on a single processor, and the average time taken for evaluating metrics per test phase is reported in table 4.4. The blur metric took on an average 17.49 ms compared to 19.45 ms by the sharpness metric. It should be noted that these figures represent qualitative performance of the metric. The code could be further optimized, or it could be implemented in a different coding language to increase speed.

4.6.5 Comparison between variance and threshold-based metrics

We have discussed particular cases of sharpness and blur metric application, i.e., variance and threshold-based metrics, respectively, that can determine the phase value for high quality image reconstruction of a Lissajous-scanned image. A summary of the strengths and weaknesses of the two methods are as follows: In the threshold-based blur metric the global phase search results may be sensitive to the value of threshold parameter σ. The optimum value of σ may be different for different images which make the implementation of threshold-based method less robust. The variance metric is threshold-free, making it very robust in predicting the phase. However, the computation time for the threshold metric is 10% less than the variance metric as the former involves working with binary variables. The faster method can be desirable in some real-time imaging applications such as endomicroscopy, especially if computational resources are limited. In addition, the threshold- based metric is also observed to provide a more prominent local minimum than the sharpness metric in all sample images.

4.7 Conclusion

In this paper, sharpness-based image processing metrics to correct for phase delay in a Lissajous-style MEMS scanner are introduced. A novel threshold-based blur metric is developed which binarizes the raw data to predict the phase error in the reconstructed image in a computationally efficient form. A variance-based sharpness metric is also implemented to able to successfully determine the true phase value. In

high FR imaging application, missing pixels being inevitable adversely affects both the metrics and may lead to error in results. It is observed that threshold metric is less robust compared to the variance metric in global search, however, the threshold metric is faster as it involves calculation with binary variables and is better suited to real-time phase correction. Both of these metrics have been experimentally demonstrated to be effective in compensating for phase error in practical implementation with a MEMS-based endomicroscope. Similar algorithms could be extended to other potential applications involving single pixel imaging or projection.

As future work, a variety of other image-based metrics inspired by autofocus and related algorithms could conceptually be adapted for use in MEMS scanner phase tracking. The proposed blur and sharpness metrics were selected based on potential for leveraging specific Lissajous properties versus correspondence to high-popularity approaches in other applications, respectively, but we acknowledge that this is not an exhaustive exploration of candidate criteria. Other potential improvements include dynamic thresholding of binary data and/or further analysis to reduce computation time, in order to further facilitate high-speed, real-time endoscopic imaging.

CHAPTER V

Two-photon Sideview 3D Imaging Instrument for Small Animals

This chapter describes the design and preliminary testing of a handheld multi-photon endomicroscope based on MEMS scanning mirrors. Optical design is done to optimize resolution when using a combination of Lissajous-pattern electrostatic mirror for lateral scanning and a axially-translating mirror (such as the electrothermal mirrors described previously) for axial scanning. Mechanical design for assembly is presented, followed by early benchtop images acquired with the assembled instrument.

5.1 Introduction

There has been growing interest in developing an in-vivo 3D-imaging endomicroscopy instrument for small animals. Imaging systems capable of longitudinal studies, without needing animal sacrifice, have many applications in assessing drug efficacy [7], studying transient effects due to drug-inducing agents [8], and observing disease progression. The images captured along a plane perpendicular to tissue surface (vertical plane) in hollow organs such as colon offer early insights into disease propagation. For example, a pre-malignant condition, dysplasia, can be observed before growing into malignant polyp by imaging either 3D volume or along vertical plane. In-vivo assessment of the targeted biomarkers expressed within a tissue plays a vital role in such studies. Imaging modalities capable of targeted imaging with sub-cellular resolution, such as confocal or multiphoton microscopy, are well suited for this application.

Two-photon microscopy (TPM) has several advantages over single-photon (or confocal) microscopy (SPM). In confocal microscopy, a focused beam excites a specimen in double-inverted cone shape, which requires a pinhole on the emission path. However, TPM is intrinsically confocal - meaning the excitation and emission occurs only at a small, typically femtoliter, focal volume. As a result, TPM doesn't require a pin-

hole, increasing collection efficiency, specially in thick specimen where fluorescence photons are scattered and most of them get rejected by the pinhole in SPM. Second, the excitation and collection wavelengths are widely spaced, making it easier to separate them and minimizing the loss of signal during filtering. Third, the higher excitation wavelengths used in TPM are significantly less absorbed in biological tissues compared to the shorter wavelengths in SPM, resulting in reduced photobleaching and photodamage. Lastly, deeper penetration can be obtained using TPM due to longer excitation wavelengths.

A variety of in-vivo two-photon 2D instruments have been developed by various researchers around the world [9]–[20] and summarized in table 1.3. Recently, attempts were also made to develop a 3D imaging prototype [45], [46]. For instance, Dilipkumar *et al.*'s system [45] is free space coupled and uses an electrically tunable lens (ETL) for achieving axial scanning. The imaging speed of their prototype is limited by the response of ETL and frame rate was less than 2 Hz. The overall prototype dimension are large due to a bulky coupling objective lens. On the other hand, a piezo stage was used for axial scanning in Ang Li *et al.*'s prototype [20], making the overall footprint of the handheld part even larger. These prototypes were arranged in front view configuration, however, sideview systems are often desired as it offers better contact with the tissue surface. Thus, there is a need to developed a fast and compact system capable of targeted 3D imaging with subcellular resolution, preferably in a sideview configuration.

In this chapter, we develop a miniature two-photon instrument with distal probe measuring less than 3.8 mm in diameter. The lateral scanning is performed by 2D MEMS located insde the distal probe tube. The axial scanning is done in the remote handheld part. We use abberation-free scanning technique previously proposed by [76], and demonstrate imaging on a benchtop system by [49], [57]. We use a side view configuration and couple the light into the instrument in freespace. The aim of the study is to demonstrate two-photon 3D scanning capability with a subcellular resolution, with FOV measuring more than 200µm in each direction captured at frame rate of more than 10 Hz for 2D, and 0.1 Hz for 3D.

5.2 Optical design

The optical design for a 3D, multi-photon imaging instrument is implemented using separate axial (Z) and lateral (2D-XY) scanning. A variety of ray-trace simulations were done using Zemax simulation software to achieve on-axis diffraction-limited

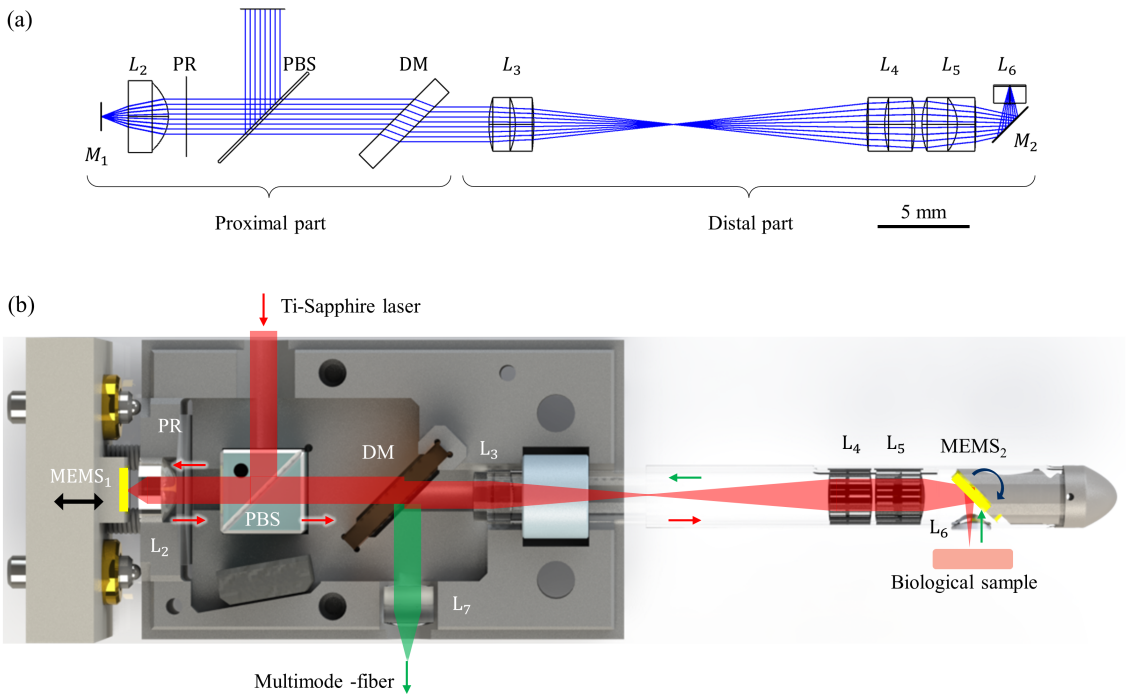

Figure 5.1: The two-photon 3D imaging instrument: (a) optical layout, (b) instrument design.

performance. The aim of the simulations was to optimize the system performance metrics, like lateral and axial resolution, 3D-FOV, working distance, off-axis aberration, etc., with the constraint of using only commercially available lenses. The goal was to maximize image space NA while maintaining the adequate FOV, and lateral and axial resolution.

The resulting instrument design consists of two primary sections, as handheld and distal sub-assemblies. The handheld assembly consists of relatively large optical elements like a polarization beam splitter, dichroic filter, etc. The distal optics, in contrast, are packaged in two small cascaded stainless steel tubes that can be inserted in the small animals for in-vivo imaging.

The optical designs starts with a collimated P-polarized light from a laser source. This light is reflected by a polarization beam splitter (PBS, PBS052, Thorlabs) and passed through a $\lambda/4$ phase retarder film (PR, WP140HE, Edmund Optics) before reaching an aspheric lens L_2 with $f = 2.75$ mm (355392-B, Thorlabs). The focused light from lens L_2 is normally incident on the axial MEMS scanner M_1. We use a lens L_2 with high NA 0.64 to achieve the focal point scanning magnification. Achromatic doublet lenses are better suited for femtoseconds laser to avoid pulse broadening, and efficient relay of emission signal. However, using the aspheric lenses for objective and

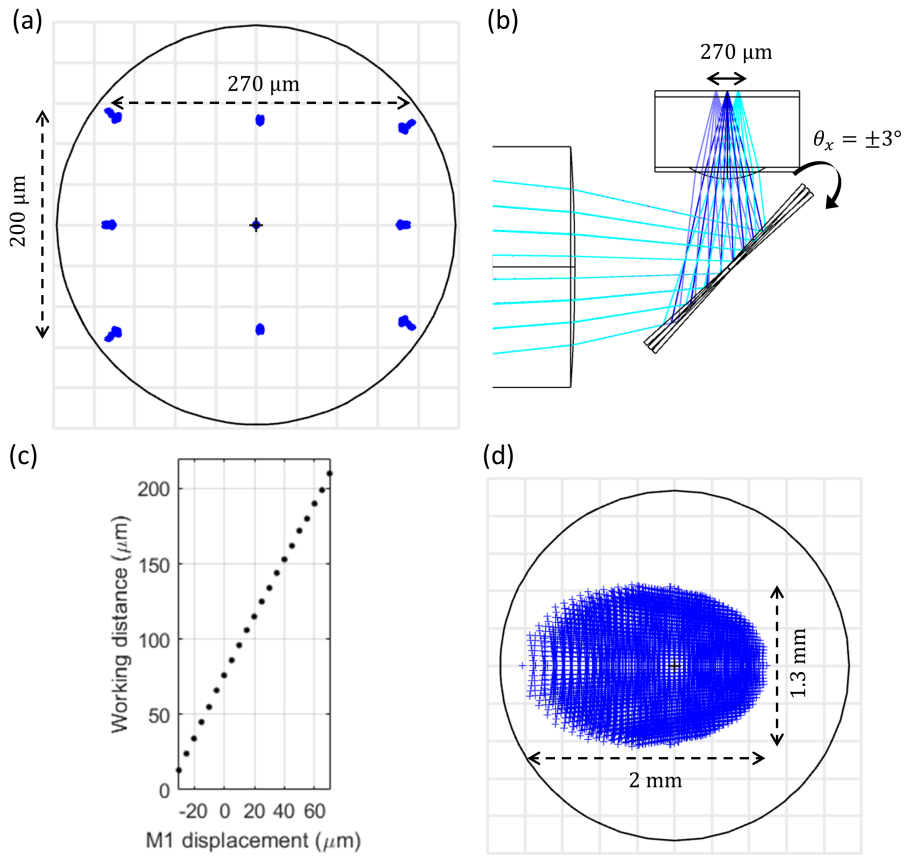

Figure 5.2: (a) Lateral (XY) FOV of the instrument generated by scan angles of $\theta_x = \theta_y = \pm 3°$. (b) Ray-trace for lateral (X) scanning. (c) Focal point displacement in the axial direction at the distal end as a function of M_1 displacement. (d) Laser light footprint on the mirror M_2 for all extreme scanning configuration.

L_2, provided smallest spot size during simulations. The fig. 5.2(c) shows the axial displacement of focal point at a distal end as a function of M_1 displacement.

The reflected light from M_1 is defocused by L_2. When the light passes again through a phase retarder film, it undergoes a net phase change of π making the light S-polarized and allowing it to pass through the PBS. A dichroic filter (FF605-Di02, Semrock) placed after PBS slightly shifts the optical axis. The beam then enters the distal subassembly and is expanded by a telescopic system formed by achromatic doublet lenses L_3 with $f = 9$ mm (45090, Edmund Optics) and L_4 with $f = 12$ mm (45262, Edmund Optics). L_3 and L_4 were chosen to make the distal part long enough for colon imaging in mice. During various experiments, it was observed that a probe can be inserted easily up to 40 mm deep inside the mouse. The light is then focused by pre-objective lens L_5 with $f = 6$ mm (45089, Edmund Optics) to (i) decrease the footprint on MEMS M_2, and (ii) increase the overall NA of the system. We used

a parametric resonant electrostatic MEMS M_2 similar to previously developed [36], and to those used in phase detection experiments. The mirror M_2 is used for lateral scanning (XY-plane) and steers the beam in a Lissajous pattern. The objective lens L_6 with $f = 1.45$ mm (354140-B, Thorlabs) focuses the light on the tissue sample. In the simulations, the space between the objective L_6 and the image plane is modeled as water to represent in-vivo conditions of objective lens being in contact with tissue.

The effective NA of the system is 0.47. The ray-trace simulations show a lateral FOV of 200 µm × 270 µm when the MEMS is scanned by $\theta_x = \pm 3°, \theta_y = \pm 3°$ as seen from fig. 5.2(a)-(b). In the simulations we achieved a diffraction-limited RMS spot size of 0.715 µm at the center, and as we scan off-axis it increases. The spot size at various locations in FOV is shown in the fig. 5.3. The footprint of the laser beam on the scanning mirror for all scanning configurations is shown in fig. 5.2(d). The footprint dictates the mirror size on the MEMS M_2. Dr. Haijun developed the MEMS M_2 used in the prototype instrument to meet specifications dictated by the optical design, in the form of scanning angles, mirror dimensions, and overall shape.

5.2.1 Emission signal ray-trace

Ray-trace simulations were performed to check the emission signal coupling with the multi-mode fiber. A nominal wavelength of 440 nm was used to represent the emission fluorescence signal in the Zemax simulations. The emission light was modeled as a point source coming from the focal point locations obtained from excitation simulations for different scanning configurations. A lens with f=4.5 mm (49270, Edmund optics) was used to focus the emission signal on the core of a multimode fiber. The spot size on the core of fiber was observed to be within a diameter of 300 µm for all extreme scanning configurations. The overall footprint changed negligibly when using different wavelengths between 400-500 nm. A multimode fiber core diameter of 400 µm (FT400UMT, Thorlabs) was chosen based on this simulation results.

5.3 Mechanical design and packaging

5.3.1 Distal assembly

The distal assembly consists of lens L_3 to L_6 and lateral scanner M_2. The lens L_3 to L_5 are housed in stainless steel (SS) tube-A having inner diameter (ID) 3.0 mm and outer diameter (OD) 3.4 mm (304H10X, Microgroup). Meanwhile, L_6, M_2, and a component referred to as a MEMS holder are packed in slightly larger SS tube-B

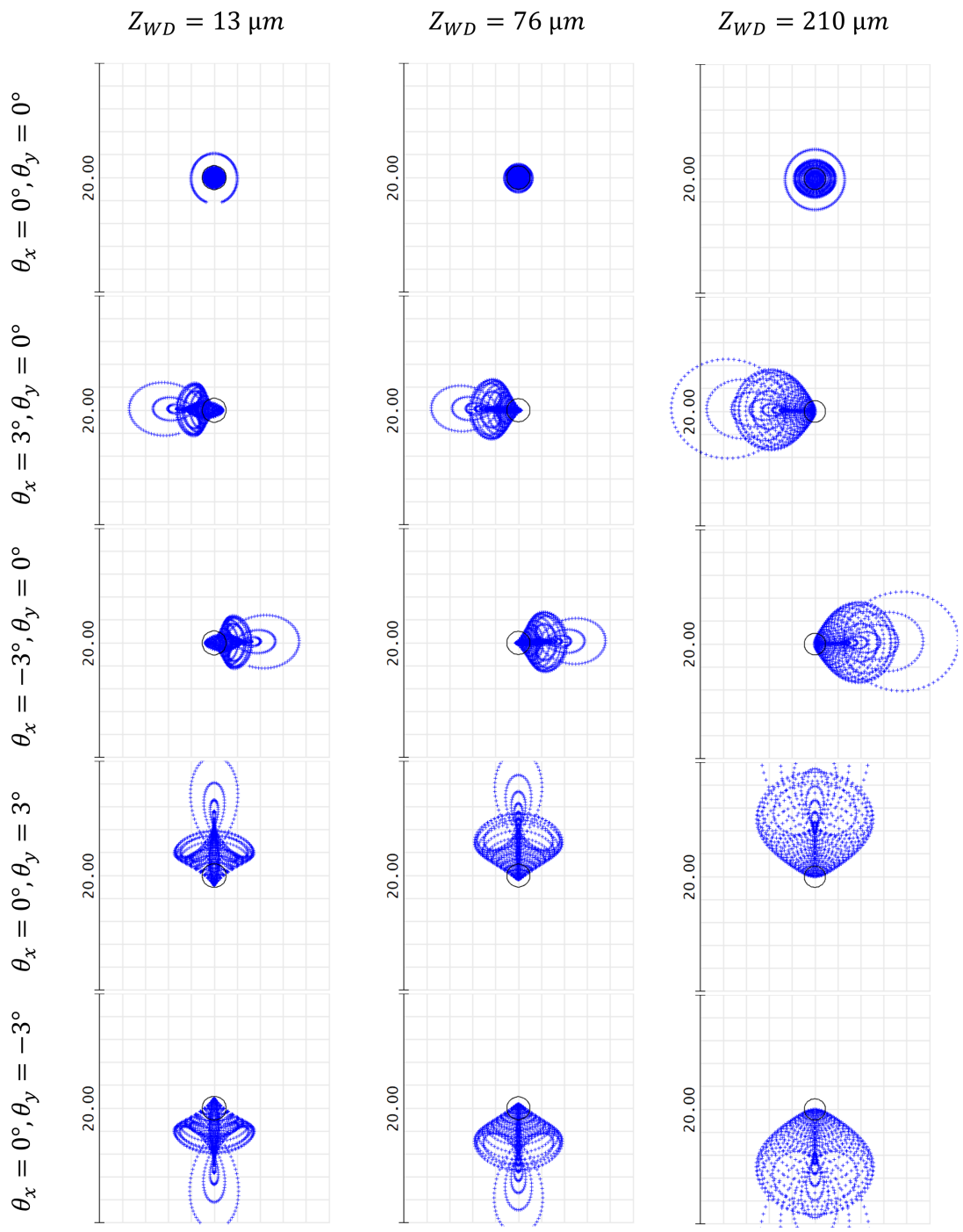

Figure 5.3: Spot diagram simulation for various scanning configurations. The focal depth changes across the columns in the figure.

of ID 3.4 mm, OD 3.7 mm (304H09XX, Microgroup). A separate and wider tube-B is used due to the large M_2 footprint shown in fig. 5.2(d), which gives very little room for designing the MEMS to meet other specification like θ_x, θ_y titling angles if restricted to a 3.0 mm ID.

We start with cutting the tubes slightly larger than the desired length. We then polish both the ends of the tube using a fixture to make ends (i) perpendicular to the tube's length, and (ii) achieve the desired lengths with a tolerance of +0 to -10 µm. Notches measuring 1 mm wide with desired lengths are cut by a CNC milling process along the tube to assist in packaging lenses during further steps. A hole is precisely machined on tube-B for L_6 maintaining a tight tolerance on the distance of the center of the hole from the tube-B's end. A brass fixture is machined in the same setting prior to making notches and holes in the tube. This allows us to achieve the highest precision in the fabricated part.

The telescopic system formed by L_3 and L_4 is realized by, first, placing L_4 at an approximate position inside tube-A and then gluing it using UV activated adhesive (3525, Loctite). The position of L_3 is adjusted to obtain collimated light out. L_3 is glued upon observing collimated light output over a length of 1 m using a beam profiler. Lens L_5 is then glued to the tube such that lens surface S1 is coincident with the end of the tube-A. This allows us to accurately control the distance between L_5 and L_6 by using the end of tube-A as a control surface.

The distance between the lens L_6 and the axis of tube-B is controlled using the high accuracy 3D printed fixture (obj-aligner, refer fig. 5.4(a)). We used Protolabs's MicroFine technology for 3D printing which offers the highest print resolution commercially available. The tip-tilt alignment of the L_6 was done using another 3D printed fixture which can be attached to the obj-aligner. After satisfactory alignment L_6 is glued to tube-B. The tube-A which now has L_3 to L_5 is inserted in tube-B till it touches the obj-aligner whose length is designed to maintain an accurate distance between L_5 and L_6. Both the tubes are glued at this position, while applying a slight force in the axial direction during the gluing process. The obj-aligner is replaced by M_2 which is mounted on a MEMS holder using wire-bonding free technology. The rotational degree of freedom is controlled by a notch on tube B and a matching fitment on the MEMS holder. A 3D printed bush is glued to the other end of tube-A to take any axial load during in-vivo experiments. This completes the packaging of the distal assembly.

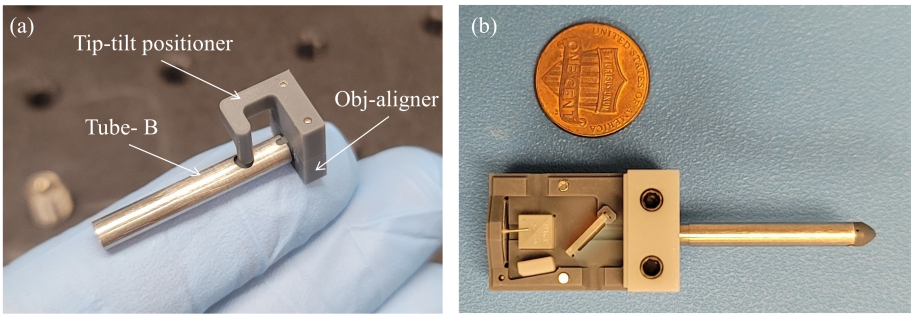

Figure 5.4: (a) 3D printed fixtures for aligning lens L_6 with tube-B, (b) Packages compact handheld instrument for two-photon imaging.

5.3.2 Handheld system assembly

The handheld system assembly is made from a high-resolution 3D printed base. We start by gluing the polarization beam splitter (PBS052), and dichroic filter. The fast (or slow) axis of the phase retarder film needs to be oriented at 45 deg to the light polarization. To do so, we use a 3D printed template to cut the film and hang it to the base as a pendulum using a pin. This allows us to do fine adjustments in angle before gluing the retarder film to the base. Finally, lens L_2 is glued. The overall dimension of the handheld part is 13x18x30 mm^3. The distal probe can be assembled now with the base to complete the packaging. Figure 5.4(b) shows the packaged instrument.

5.4 System architecture

To test the prototype instrument, it must be situated in a larger imaging system that provides illumination light and detects returning fluorescence. The system is summarized in fig. 5.5.

A Ti-sapphire laser (Mai Tai DeepSee HP DS, Spectra-Physics) in a mode-locked state is used to generate a short excitation pulse with a width of ∼100 fs and repetition rate of 80 MHz at 785 nm wavelength. The laser has a tunable spectral range of 690-1040 nm and comes with a dispersion compensation unit in-build to shorten the pulse width. The laser operates in a mode-locked state only at much higher power than required for imaging. We used a combination of a half-wave plate (HWP) and linear polarizer (LP) placed after the laser to control the power and polarization state of the laser beam.

The P-polarised output light is then fed into the instrument, where the PBS reflects it at 90 deg, and is focused onto the axial MEMS scanner by lens L_2. The normally incident light on M_1 gets reflected towards the PBS and undergoes a phase

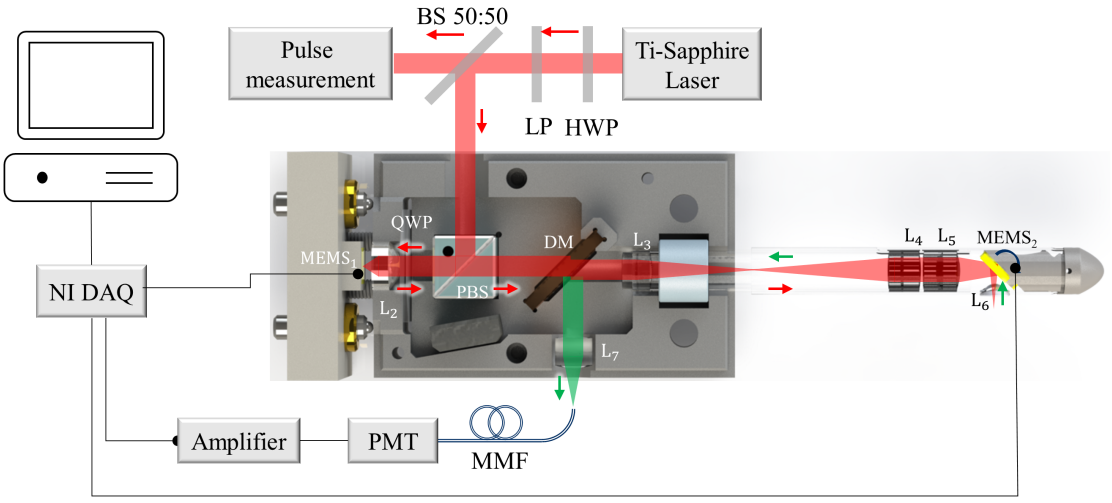

Figure 5.5: Handheld system architecture for 3D two-photon imaging in small animals

change of $\pi/2$ on passing twice through the retarder film. The S-polarized light passes through the PBS and DM and is coupled into the distal probe. After passing through the distal series of lenses, the light gets scanned using M_2 and focused on tissue samples or other targets by L_6 as explained in section 5.2. The high NA system excites a small focal volume of the tissue sample. When two photons of the longer wavelength (785 nm) get absorbed in the sample, a fluorescence signal at a shorter wavelength is generated and collected by the lens L_6. The emission signal is then de-scanned by the MEMS M_2 and returns by the same path until DM. That long-pass filter (DM), kept at 45 degrees to the optical axis, reflects the fluorescence signal by 90 degrees. The emission light is focused by lens L_7 onto a multimode fiber (MMF, FT400UMT, Thorlabs) which is connected to a photo-multiplier tube (PMT, H7422PA-40, Hamamatsu). A bandpass filter is placed before the MMF to filter out unwanted light.

The light is sensed by the PMT and its output is amplified using a high-speed low noise current amplifier (59178, Edmund Optics). The amplified signal is digitized by a high-speed National Instruments data acquisition board (NI, PCI-6115). The same NI board is used to actuate the MEMS scanner. A LabView program is developed to read the raw data, drive the scanner, and reconstruct the image from raw data.

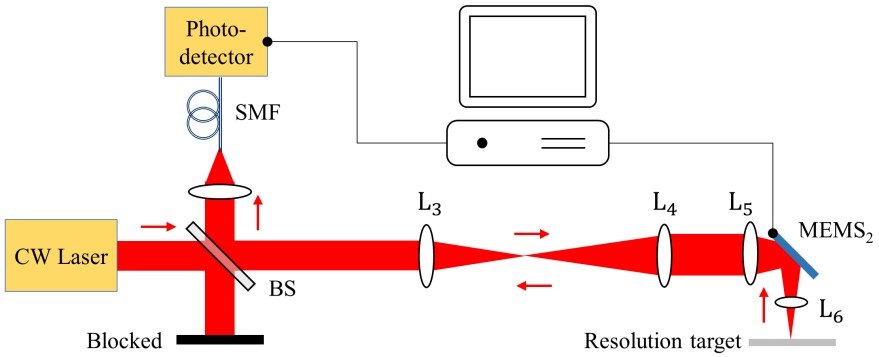

Figure 5.6: System architecture for confocal reflectance imaging

5.5 Results

5.5.1 Confocal reflectance imaging

Confocal reflectance images of a resolution target were collected to check the alignment of optical elements in the distal probe and test its scanning and optical performance. We use the same detachable distal probe from a 2-photon setup as described in section 5.3 with a modified handheld base to collect reflectance images. The system architecture for these experiments is shown in fig. 5.6. Light at 785 nm wavelength from a continuous wave (CW) laser (iBeam smart -785, Toptica photonics) is split by a 50:50 beam splitter (BS). One leg of light is fed into the distal probe and the other reflected leg is blocked. The light is scanned in a Lissajous pattern on reaching electrostatic parametric resonant mirror M_2. The light is then focused on the resolution target placed below the object lens. The reflected light from the resolution target is descanned by M_2 and comes back to BS after passing through L_5 to L_3. The 50% of light is coupled in the graded-index multimode fiber (MMF, GIF625, Thorlabs) using a lens and the other 50% is blocked. The light is detected by the photo-detector (2107-FC-M, Newport) connected to the computer. A LabView program is used to reconstruct the image.

The reflectance image of a USAF resolution target, group 07 taken using the probe is shown in fig. 5.7(a). The smallest element of group 07 i.e., element 06 has 228.1 line pairs/mm, which translates to 2.19 µm line width. As seen from the figure, the probe could clearly resolve the three horizontal and vertical lines of element 06. In addition, a knife-edge test was performed to measure the lateral resolution of the system. An edge of a large feature on the resolution target was selected to represent a knife-edge. The reflected power was measured by moving the edge, and plotted as

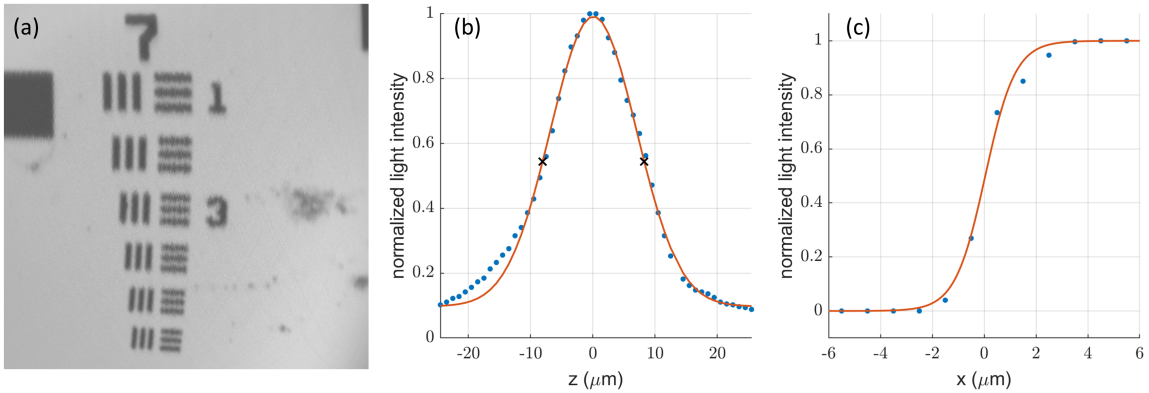

Figure 5.7: (a) Confocal reflectance image of USAF resolution target - Group 7. (b)-(c) Measured axial and lateral resolution of the reflectance image, respectively.

a function of x-displacement in fig. 5.7(c). The beam waist w_x at the focal point is given by the eq. (5.1), where, X_{10-90} is the distance between the points at which the power is 10% and 90% of maximum power.

$$X_{10-90} = 1.28 w_x \tag{5.1}$$

The measured data is too coarse for estimating the X_{10-90} value as the linear stage could only be moved in steps of 1 µm. A sigmoid function was fitted and X_{10-90} value of 2.55 µm was extracted. The lateral resolution (w_x) is estimated to be 2 µm using eq. (5.1). The theoretical Abbe diffraction limited resolution in the air is 1.1 µm.

The axial resolution was estimated by recording the reflected light power while moving the resolution target in axial direction (z). A large reflective surface on the target was chosen to perform this test. The normalized power is plotted as a function of z. A Gaussian is fitted to the measured data and FWHM of 16.3 µm is extracted, which represents the axial resolution. Both the axial and lateral resolution tests were performed in the air refractive index $n = 1$. However, the tissue sample will be placed in water ($n = 1.33$) when imaging in-vivo or ex-vivo using the two-photon system. The actual resolution may increase by up to 33% compared to reflectance imaging estimates.

5.5.2 Multi-photon imaging

Preliminary fluorescence imaging was performed using a Ti-sapphire laser. The light at 720 nm wavelength at 80 MHz repetition rate having pulse width of 400 fs was used to excite the fluorescent calibration target (DA113, Max Levy). The average power measured at the target surface was 100 mW. A grid pattern on the target with

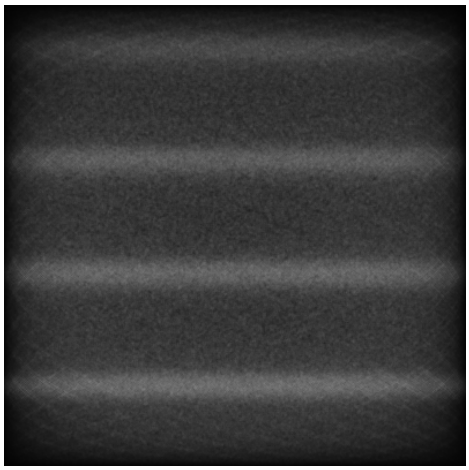

Figure 5.8: Preliminary two-photon 1D image of a grid pattern on fluorescent target

8 µm line width and 50 µm spacing was imaged. We performed 1D MEMS scanning as the other axis was not functioning as expected at the time of experiments. The image is shown in fig. 5.8 and SNR was increased by averaging frames for 60 seconds.

5.6 Future work

The major drawback of the optical schematic discussed in section 5.2 is the laser light is delivered into the system in freespace. A fiber-coupled system is necessary for broader use of the instrument. The PBS, which is required to implement aberration-free Z-scanning, is the bottleneck in using a fiber for light delivery. The PBS needs a fixed polarization at the input. A typical polarization-maintaining fiber's core is dispersive, which inevitably broadens the ultra-short femtoseconds light pulse. A hollow-core photonic bandgap fiber, suitable for delivering short pulse, currently is not available commercially in polarization-maintaining configuration. This section describes several options that can be explored to build a fiber-coupled two-photon 3D imaging instrument.

1. Polarization maintaining fiber with negative dispersion compensation.

2. Implementing a closed loop polarization compensation by using a HWP plate at the laser end and a power sensor in the handheld part.

One approach is to explore other mechanisms for achieving aberration-free scanning that don't require PBS. Previously, research has mounted a lens on the MEMS scanner , and displaced it in an axial direction to achieve focal point scanning. This kind of scanning suffers from low scanning bandwidth due to the relatively high weight

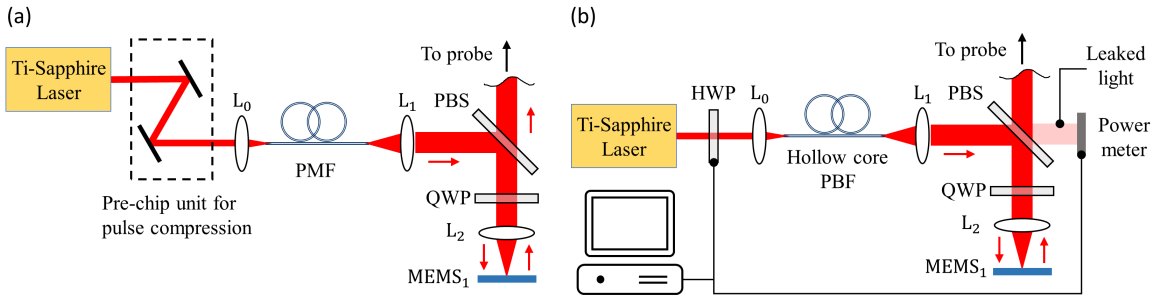

Figure 5.9: Optical schematics for fiber-coupled instruments based on aberration-free axial scanning implemented using (a) pre-chirp to compensate the pulse broadening in polarization maintaining fiber, (b) closed loop feedback system to correct change in polarization at the output of the hollow core fiber.

of the lens. Instead, a Fresnel zone plate can be designed on the MEMS reflector surface which serves as a lens.

Another option is to use a folded light path, where light is reflected between the fixed and a moving mirror. A similar arrangement has been demonstrated previously for lateral scanning [6], and this could be adopted for axial scanning. The optical design is shown in the fig. 5.10. A hollow-core fiber (HC-800-02, NKT Photonics) with an outer diameter of 220 $\mu m \pm 50$ passes through a 300 µm hole centrally made on the MEMS mirror. The fiber has NA=0.2 and diverging light coming out from the fiber is reflected by the mirror with OD = 350 µm placed in front of it. We can choose to make a circular mirror directly on the aspheric lens (L_2, 354350, Lightpath), using sputtering/evaporation, for compact packaging. Alternatively, a separate mirror can be used as well. The reflected light undergoes the second reflection from the MEMS scanner, and making the direction of propogation towards the distal probe. The light is almost collimated by lens L_2 and fed into the probe after passing through the dichroic mirror. From this point onward the working is the same as discussed in section 5.2.

5.7 Conclusion

In this work, we have demonstrated a concept for compact two-photon 3D imaging instrument capable of taking histology like images. The optics and MEMS scanner are packaged in a distal probe measuring just 3.7 mm outer diameter, and having a length of 30 mm to facilitate imaging at different location in mouse colon. The optical schematic was optimized using off-the-shelf optical elements for lowering the cost of prototyping. Simulations show a lateral (XY) FOV of 270 µm × 200 µm

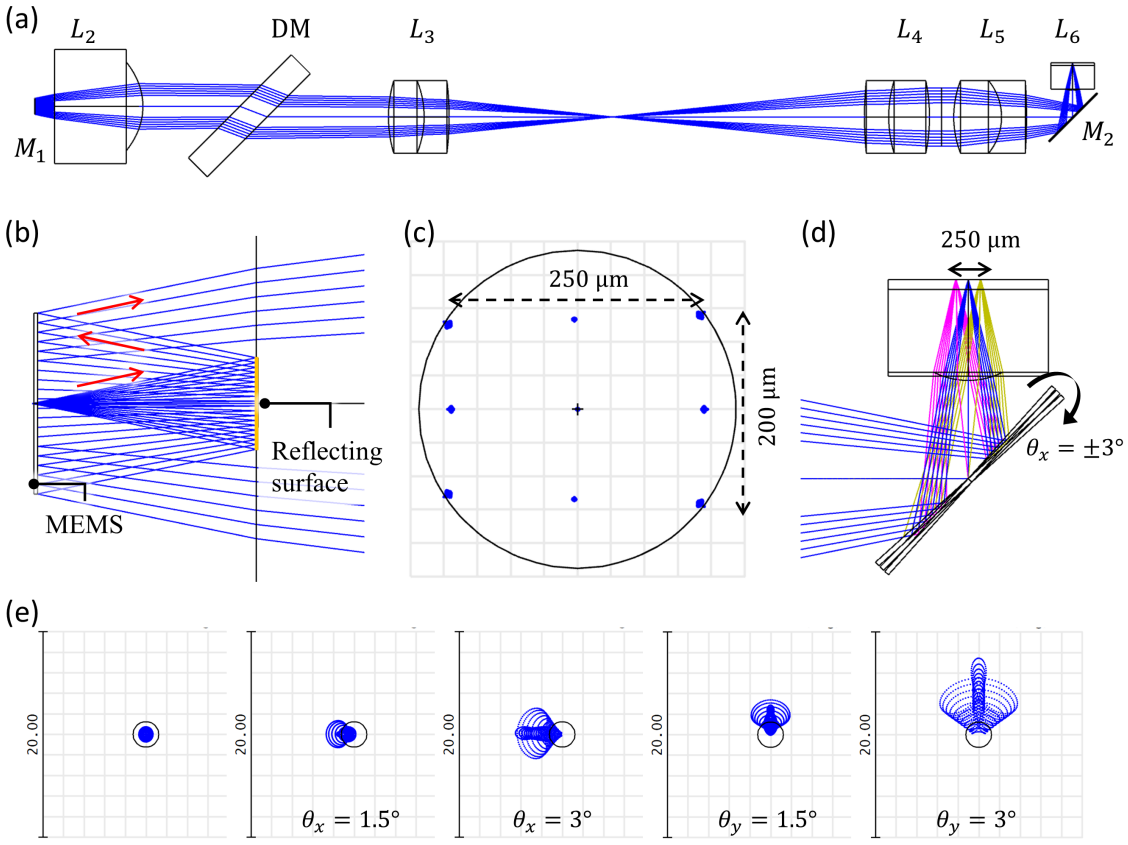

Figure 5.10: (a) Optical layout for folded path axial scanning for a fiber-coupled instrument, (b) working of folded path axial scanning using a MEMS scanner and a fixed reflector, (c) lateral FOV of the proposed system, (d) ray-trace for X scanning, (e) spot diagram for on axis, X, and Y scanning

when the MEMS is scanned by $\theta_x = \theta_y = \pm 3^\circ$. Amplification of 2x in the axial (Z) displacement of focal point was achieved, when scanned by Z-MEMS, using a high NA aspheric lens L_2.

On-axis diffraction limited performance of the instrument is confirmed by a confocal reflectance imaging setup, designed such that the same distal probe from the two-photon instrument can be interchangeably used. The lateral and axial resolutions in the confocal reflectance imaging experiments were estimated to be less than 2 µm and 16.3 µm, respectively. The smallest feature on the USAF resolution target i.e., group 07 element 06 can be clearly seen in the captured images. A preliminary 2D two-photon images of fluorescent target were captured using endomicroscopy probe. The imaging setup needs further alignment adjustments to enhance signal to noise ratio of the two-photon images. The scope of this work can be extended to develop a fiber coupled instrument by exploring the designs suggested in the section 5.6.

5.8 Acknowledgement

I thank Ahmad Shirazi for helping in machining the SS tubes and providing valuable suggestions for the packaging of the probe. I thank Miki Lee for customizing the LabView program and her support during imaging experiments and MEMS characterizations. I also thank Tayebeh Sahraebelverdi for giving valuable insights during the reflectance imaging test. I thank Dr. Haijun Li for developing a custom electrostatic MEMS scanner.

CHAPTER VI

Conclusion and Future Works

6.1 Summary

Motivated by frequent sources of image misregistration in endomicroscopy systems, We have developed an algorithm based on image feedback to correct the phase errors in a multi-axis MEMS scanner. These MEMS scanners are often used in a miniature endomicroscopy system designed as screening or scientific tools for the diagnosis, monitoring, and/or study of disease. We introduced threshold and variance metrics, as examples from a broader class of image quality metrics, to estimate the undesired phase delays during in-vivo imaging with MEMS scanners. We demonstrated a significant improvement in the image quality on correcting for phase predicted by the algorithm, enabling identification of key biological features. While the threshold metric takes less computation time compared to the sharpness metric, the former is less robust as the phase estimation is sensitive to the choice of the threshold parameter. Nevertheless, with the real-time mouse tissue imaging, we have shown either metrics are well suited for single-pixel imaging applications involving multi-axis MEMS scanner.

Motivated by a need to develop a 3D deep tissue imaging system, we use two separate MEMS scanner for lateral and axial scanning in realizing a 3D system. Among various transduction mechanisms, electrothermal scanners offer high displacement with relatively less fabrication complexity. However, electrothermal actuators traditionally suffer from slow time-response hindering real-time imaging. We developed a fast and efficient electrothermal actuator by reducing both thermal and inertial mass. A novel honeycomb-shaped support structure was shown to be effective in making the scanner fast without much increase in mirror curvature due to residual stress. The increased curvature did not adversely affect the image quality and achieved an axial resolution of 6 µm in a 3D 2-photon benchtop imaging system. With these promising results, we are now in the process of making compact handheld instruments capable

of 3D 2-photon imaging.

We developed a miniature handheld prototype to capture 3D two-photon in-vivo images in a sideview configuration. The two-photon imaging technique has various advantages over confocal microscopy such as reduced photobleach/photodamage, higher penetration depth, better signal collection efficiency. The optical schematic was optimized to increase the image space NA while maintaining adequate FOV, lateral and axial resolution, with a constrain of using off-the-shelf optical components. The mechanical design was laid out to accommodate the dimensional tolerance of optical elements, facilitate easy assembly, while restricting the overall dimension of the instrument. The probe's capability was demonstrated by installing the it in confocal reflectance setup where a lateral and axial resolution of 2 µm and 16.3 µm were achieved when imaging in the air. The resolution could increase in water which is an approximation of tissue's refractive index. A preliminary 2-photon image of a fluorescent target was captured. A further optimization is needed to increase signal to noise ratio of the imaging system.

6.2 Contributions

The main contribution of this dissertation are listed below:

1. Developed an algorithm to estimate phase delays in multi-axes MEMS scanners using image-based metrics.
2. Introduced a practical threshold metric for rapid phase delay assessment.
3. Introduced a robust variance metric for reliable phase estimation.
4. Developed a target for phase errors as a function of acceptable image quality.
5. Demonstrated estimation error less than 1 mrad using simulation.
6. Demonstrated significant improvement in the in-vivo image quality on phase correction.
7. Demonstrated a significant reduction in thermal and inertial mass of an electrothermal scanning mirror using novel honeycombed shaped support structure.
8. Developed a circuit model for performing fast thermal simulations.

9. Demonstrated an electrothermal scanner with thermal bandwidth more than 150 Hz, time thermal constant of 3.42 ms, and static displacement per unit input power = 2.08 µm/W.

10. Developed a benchtop 3D multi-photon imaging system with both lateral and axial scanning performed in remote location.

11. Obtained sample 3D images of pollen grains with a measured axial resolution of 6 µm.

12. Optimized the optical schematic for two-photon 3D imaging to by maximizing the image space NA while maintaining adequate FOV, lateral and axial resolution

13. Developed a mechanical design for easy assembly, and to limit the effect of dimensional tolerance of the optical elements

14. Demonstrated confocal reflectance images with a lateral and axial resolution of 2 µm and 16.3 µm

15. Capture a preliminary two-photon image of fluorescent target to demonstrate a proof-of-concept

6.2.1 Selected journal publications

1. **M. Birla**, M. Lee, T. Sahraebelverd, A. Shirazi, H. Li, T. Wang, and K. R. Oldham, "Compact side view two-photon 3D imaging instrument" (under preparation).

2. **M. Birla**, J. Zou, Z. Afkhami, X. Duan, H. Li, T. Wang, and K. R. Oldham, "Multi-photon 3D imaging with an electrothermal actuator with low thermal and inertial mass", *Sensors and Actuators A: Physical*, 329 (2021): 112791.

3. **M. Birla**, X. Duan, H. Li, M. Lee, G. Li, T. Wang, and K. Oldham, "Image processing metrics for phase identification of a multi-axis MEMS scanner used in single pixel imaging" *IEEE/ASME Transactions on Mechatronics*, 26.3 (2021).

4. Y. Zhu, **M. Birla**, K. R. Oldham, and E. T. Filipov, "Elastically and plastically foldable electrothermal micro-origami for controllable and rapid shape morphing", *Advanced functional materials*, p. 2003741, 2020.

5. Y. Chen, M. Lee, **M. Birla**, H. Li, G. Li, X. Duan, T. D. Wang, and K. R. Oldham, "Motion estimation for a compact electrostatic microscanner via shared driving and sensing electrodes in endomicroscopy," *IEEE/ASME Transactions on Mechatronics*, vol. 25, no. 2, pp. 661-672, 2020.

6. G. Li, X. Duan, M. Lee, **M. Birla**, J. Chen, K. R. Oldham, T. D. Wang, and H. Li, "Ultra-compact microsystems-based confocal endomicroscope," *IEEE Transactions on Medical Imaging*, vol. 39, no. 7, pp. 2406–2414, 2020.

7. J. Yu, **M. Birla**, M. Lee, G. Li, H. Li, T.D. Wang, and K.R. Oldham, "Estimating Perturbations to Laser Position on Tissue for Lissajous Scanning in Endomicroscopy", *IEEE/ASME International Conference on Advanced Intelligent Mechatronics (AIM)*, IEEE, 2020.

6.3 Future work

The promising 2-photon pollen images obtained using benchtop system and a free-space coupled instrument, development of phase correction algorithm to eliminated the phase delays in multi-axes scanner, development of axial electrothermal scanner, brings us one step closer in making robust handheld probe. The future direction of this research could be developing a fiber-coupled instrument providing more flexibility during the in-vivo imaging in small animals. A few options are briefly discussed in section 5.6. The design with folded beam path for Z-scanning can be implemented in relatively short time for testing, as similar design has been demonstrated for confocal microscopy [6].

APPENDICES

APPENDIX A

Ideal piston motion with star configuration

Let V_{ij} and I_{ij} represents the voltage and current across terminal i, j. We have,

$$V_{ij} = I_{ij}(R_i + R_j) \tag{A.1}$$

$$\begin{bmatrix} I_{12} & I_{12} & 0 & 0 \\ 0 & I_{23} & I_{23} & 0 \\ 0 & 0 & I_{34} & I_{34} \\ I_{14} & 0 & 0 & I_{14} \end{bmatrix} \begin{bmatrix} R_1 \\ R_2 \\ R_3 \\ R_4 \end{bmatrix} = \begin{bmatrix} V_{12} \\ V_{23} \\ V_{34} \\ V_{14} \end{bmatrix} \tag{A.2}$$

R_i's can be easily found out by solving the linear systems of equations. We use a small amplitude of AC voltage to measure the resistance.

Let the voltage at star junction to be V_5, which we will later arbitrarily choose it to be zero. As shown in the fig. 2.1, the current and voltage relation can be established as

$$I_i R_i = V_i - V_5 \tag{A.3}$$

where $i = 1, 2, 3, 4$, and

$$I_1 + I_2 + I_3 + I_4 = 0. \tag{A.4}$$

Assuming each leg is identical and there is no coupling between their displacements, an ideal piston motion can be achieved if each leg heats equally say $\dot{Q}$.

$$\dot{Q} = I_1^2 R_1 = I_2^2 R_2 = I_3^2 R_3 = I_4^2 R_4. \tag{A.5}$$

Clearly, multiple solution are possible as changing the current direction won't affect the heating. Lets assume all the current flows from left to right, and taking square

root of eq. (A.5),

$$I_1\sqrt{R_1} = I_4\sqrt{R_4} = -I_2\sqrt{R_2} = -I_3\sqrt{R_3}. \tag{A.6}$$

using eqs. (A.4) and (A.6)

$$I_1\sqrt{R_1}\left(\frac{1}{\sqrt{R_1}} - \frac{1}{\sqrt{R_2}} - \frac{1}{\sqrt{R_3}} + \frac{1}{\sqrt{R_4}}\right) = 0 \tag{A.7}$$

If the equivalent resistors on the mirror satisfies the condition in eq. (A.7), ideal piston motion can be achieved. If not, current in any two resistors could be made negative such that the term in the parenthesis is close to zero, since current in resistors R_2 and R_3 were arbitrarily made negative in derivation of eq. (A.7). Further the current values can be selected such that variance in the power generated in each leg is minimized.

$$\min_{I_i} \sum_{i=1}^{4} (I_i^2 R_i - \bar{\dot{Q}})^2 \tag{A.8}$$

subjected to:

$$I_1 + I_2 + I_3 + I_4 = 0$$
$$|I_i| > 0$$

where

$$\bar{\dot{Q}} = \frac{1}{4}\sum_{i=1}^{4} I_i^2 R_i.$$

APPENDIX B

Piezoelectric Constitutive Laws

Table B.1: Various forms of linear piezoelectric constitutive laws

Tensor notation	Compact tensor notation	Matrix notation
Stress-electric displacement form		
$T_{ij} = c^E_{ijkl} S_{kl} - e_{kij} E_k$	$T_p = c^E_{pq} S_q - e_{kp} E_k$	$\{T\} = [c^E]\{S\} - [e]^T\{E\}$
$D_i = e_{ikl} S_{kl} + \epsilon^S_{ik} E_k$	$D_i = e_{iq} S_q + \epsilon^S_{ik} E_k$	$\{D\} = [e]\{S\} + [\epsilon^S]\{E\}$
Strain-electric displacement form		
$S_{ij} = s^E_{ijkl} T_{kl} + d_{kij} E_k$	$S_p = s^E_{pq} T_q + d_{kp} E_k$	$\{S\} = [s^E]\{T\} + [d]^T\{E\}$
$D_i = d_{ikl} T_{kl} + \epsilon^T_{ik} E_k$	$D_i = d_{iq} T_q + \epsilon^T_{ik} E_k$	$\{D\} = [d]\{T\} + [\epsilon^T]\{E\}$
Other less common forms		
$S_{ij} = s^D_{ijkl} T_{kl} + g_{kij} D_k$	$S_p = s^D_{pq} T_q + g_{kp} D_k$	$\{S\} = [s^D]\{T\} + [g]^T\{D\}$
$E_i = -g_{ikl} T_{kl} + \beta^T_{ik} D_k$	$E_i = -g_{iq} T_q + \beta^T_{ik} D_k$	$\{E\} = -[g]\{T\} + [\beta^T]\{D\}$
$T_{ij} = c^D_{ijkl} S_{kl} - h_{kij} D_k$	$T_p = c^D_{pq} S_q - h_{kp} D_k$	$\{T\} = [c^D]\{S\} - [h]^T\{D\}$
$E_i = -h_{ikl} S_{kl} + \beta^S_{ik} D_k$	$E_i = -h_{iq} S_q + \beta^S_{ik} D_k$	$\{E\} = -[h]\{S\} + [\beta^S]\{D\}$

Note: $[\cdot]^T$ represents transpose operation, whereas,
$[\cdot^T]$ means constants' value when stress ($\mathbf{T}$) is held constant

The following relationship holds:

$$
\begin{aligned}
[c^D][s^D] = [c^E][s^E] &= I_6 \\
[\beta^S][\epsilon^S] = [\beta^T][\epsilon^T] &= I_3 \\
[c^D] &= [c^E] + [e]^T[h] \\
[s^D] &= [c^D] - [d]^T[g] \\
[\beta^S] &= [\beta^T] - [g]^T[h] \\
[\epsilon^S] &= [\epsilon^T] - [d][e]^T \\
[d] &= [\epsilon^T][g] \\
[e] &= [d][c^E] \\
[g] &= [h][s^D] \\
[h] &= [\epsilon^S][e]
\end{aligned}
$$

In the matrix form the linear stress-electric displacement equations is:

$$
\begin{Bmatrix} T_1 \\ T_2 \\ T_3 \\ T_4 \\ T_5 \\ T_6 \\ D_1 \\ D_2 \\ D_3 \end{Bmatrix} = \begin{bmatrix} c_{11}^E & c_{12}^E & c_{13}^E & 0 & 0 & 0 & 0 & 0 & -e_{31} \\ c_{12}^E & c_{22}^E & c_{23}^E & 0 & 0 & 0 & 0 & 0 & -e_{32} \\ c_{13}^E & c_{23}^E & c_{33}^E & 0 & 0 & 0 & 0 & 0 & -e_{33} \\ 0 & 0 & 0 & c_{44}^E & 0 & 0 & 0 & -e_{24} & 0 \\ 0 & 0 & 0 & 0 & c_{55}^E & 0 & -e_{15} & 0 & 0 \\ 0 & 0 & 0 & 0 & 0 & c_{66}^E & 0 & 0 & 0 \\ 0 & 0 & 0 & 0 & e_{15} & 0 & \epsilon_{11}^S & 0 & 0 \\ 0 & 0 & 0 & e_{24} & 0 & 0 & 0 & \epsilon_{22}^S & 0 \\ e_{31} & e_{32} & e_{33} & 0 & 0 & 0 & 0 & 0 & \epsilon_{33}^S \end{bmatrix} \begin{Bmatrix} S_1 \\ S_2 \\ S_3 \\ S_4 \\ S_5 \\ S_6 \\ E_1 \\ E_2 \\ E_3 \end{Bmatrix}. \tag{B.1}
$$

Similarly, the matrix form of strain-electric displacement equations is:

$$
\begin{Bmatrix} S_1 \\ S_2 \\ S_3 \\ S_4 \\ S_5 \\ S_6 \\ D_1 \\ D_2 \\ D_3 \end{Bmatrix} = \begin{bmatrix} s_{11}^E & s_{12}^E & s_{13}^E & 0 & 0 & 0 & 0 & 0 & d_{31} \\ s_{12}^E & s_{22}^E & s_{23}^E & 0 & 0 & 0 & 0 & 0 & d_{32} \\ s_{13}^E & s_{23}^E & s_{33}^E & 0 & 0 & 0 & 0 & 0 & d_{33} \\ 0 & 0 & 0 & s_{44}^E & 0 & 0 & 0 & d_{24} & 0 \\ 0 & 0 & 0 & 0 & s_{55}^E & 0 & d_{15} & 0 & 0 \\ 0 & 0 & 0 & 0 & 0 & s_{66}^E & 0 & 0 & 0 \\ 0 & 0 & 0 & 0 & d_{15} & 0 & \epsilon_{11}^T & 0 & 0 \\ 0 & 0 & 0 & d_{24} & 0 & 0 & 0 & \epsilon_{22}^T & 0 \\ d_{31} & d_{32} & d_{33} & 0 & 0 & 0 & 0 & 0 & \epsilon_{33}^T \end{bmatrix} \begin{Bmatrix} T_1 \\ T_2 \\ T_3 \\ T_4 \\ T_5 \\ T_6 \\ E_1 \\ E_2 \\ E_3 \end{Bmatrix}. \tag{B.2}
$$

Bibliography

[1] (), [Online]. Available: https://cancerstatisticscenter.cancer.org/#!/ (visited on 03/18/2020).

[2] A. G. Zauber, "The impact of screening on colorectal cancer mortality and incidence: Has it really made a difference?" *Digestive diseases and sciences*, vol. 60, no. 3, pp. 681–691, 2015.

[3] C. Lahiff and J. E. East, "Endoscopic approach to polyp recognition," *Frontline Gastroenterology*, vol. 8, no. 2, pp. 98–103, 2017.

[4] A. Lombardini, V. Mytskaniuk, S. Sivankutty, E. R. Andresen, X. Chen, J. Wenger, M. Fabert, N. Joly, F. Louradour, A. Kudlinski, *et al.*, "High-resolution multimodal flexible coherent raman endoscope," *Light: Science & Applications*, vol. 7, no. 1, pp. 1–8, 2018.

[5] F. Akhoundi, Y. Qin, N. Peyghambarian, J. K. Barton, and K. Kieu, "Compact fiber-based multi-photon endoscope working at 1700 nm," *Biomedical optics express*, vol. 9, no. 5, pp. 2326–2335, 2018.

[6] G. Li, X. Duan, M. Lee, M. Birla, J. Chen, K. R. Oldham, T. D. Wang, and H. Li, "Ultra-compact microsystems-based confocal endomicroscope," *IEEE Transactions on Medical Imaging*, vol. 39, no. 7, pp. 2406–2414, 2020.

[7] S. Gross and D. Piwnica-Worms, "Molecular imaging strategies for drug discovery and development," *Current opinion in chemical biology*, vol. 10, no. 4, pp. 334–342, 2006.

[8] L. Ritsma, S. I. Ellenbroek, A. Zomer, H. J. Snippert, F. J. de Sauvage, B. D. Simons, H. Clevers, and J. van Rheenen, "Intestinal crypt homeostasis revealed at single-stem-cell level by in vivo live imaging," *Nature*, vol. 507, no. 7492, pp. 362–365, 2014.

[9] Y. Zhao, H. Nakamura, and R. J. Gordon, "Development of a versatile two-photon endoscope for biological imaging," *Biomedical optics express*, vol. 1, no. 4, pp. 1159–1172, 2010.

[10] D. R. Rivera, C. M. Brown, D. G. Ouzounov, I. Pavlova, D. Kobat, W. W. Webb, and C. Xu, "Compact and flexible raster scanning multiphoton endoscope capable of imaging unstained tissue," *Proceedings of the National Academy of Sciences*, vol. 108, no. 43, pp. 17 598–17 603, 2011.

[11] C. L. Hoy, O. Ferhanoğlu, M. Yildirim, W. Piyawattanametha, H. Ra, O. Solgaard, and A. Ben-Yakar, "Optical design and imaging performance testing of a 9.6-mm diameter femtosecond laser microsurgery probe," *Optics Express*, vol. 19, no. 11, pp. 10 536–10 552, 2011.

[12] Y. Zhang, M. L. Akins, K. Murari, J. Xi, M.-J. Li, K. Luby-Phelps, M. Mahendroo, and X. Li, "A compact fiber-optic shg scanning endomicroscope and its application to visualize cervical remodeling during pregnancy," *Proceedings of the National Academy of Sciences*, vol. 109, no. 32, pp. 12 878–12 883, 2012.

[13] B. Smith, M. Naji, S. Murugkar, E. Alarcon, C. Brideau, P. Stys, and H. Anis, "Portable, miniaturized, fibre delivered, multimodal cars exoscope," *Optics express*, vol. 21, no. 14, pp. 17 161–17 175, 2013.

[14] H.-Y. Chung, W.-C. Kuo, Y.-H. Cheng, C.-H. Yu, S.-H. Chia, C.-Y. Lin, J.-S. Chen, H.-J. Tsai, A. B. Fedotov, A. A. Ivanov, *et al.*, "Blu-ray disk lens as the objective of a miniaturized two-photon fluorescence microscope," *Optics Express*, vol. 21, no. 25, pp. 31 604–31 614, 2013.

[15] D. Do, H. Yoo, and D.-G. Gweon, "Fiber-optic raster scanning two-photon endomicroscope using a tubular piezoelectric actuator," *Journal of biomedical optics*, vol. 19, no. 6, p. 066 010, 2014.

[16] X. Duan, H. Li, Z. Qiu, B. P. Joshi, A. Pant, A. Smith, K. Kurabayashi, K. R. Oldham, and T. D. Wang, "Mems-based multiphoton endomicroscope for repetitive imaging of mouse colon," *Biomedical optics express*, vol. 6, no. 8, pp. 3074–3083, 2015.

[17] G. Ducourthial, P. Leclerc, T. Mansuryan, M. Fabert, J. Brevier, R. Habert, F. Braud, R. Batrin, C. Vever-Bizet, G. Bourg-Heckly, *et al.*, "Development of a real-time flexible multiphoton microendoscope for label-free imaging in a live animal," *Scientific reports*, vol. 5, no. 1, pp. 1–9, 2015.

[18] L. Huang, A. K. Mills, Y. Zhao, D. J. Jones, and S. Tang, "Miniature fiber-optic multiphoton microscopy system using frequency-doubled femtosecond er-doped fiber laser," *Biomedical optics express*, vol. 7, no. 5, pp. 1948–1956, 2016.

[19] Y. Wang, Z. Li, X. Liang, and L. Fu, "Four-plate piezoelectric actuator driving a large-diameter special optical fiber for nonlinear optical microendoscopy," *Optics express*, vol. 24, no. 17, pp. 19 949–19 960, 2016.

[20] W. Liang, G. Hall, B. Messerschmidt, M.-J. Li, and X. Li, "Nonlinear optical endomicroscopy for label-free functional histology in vivo," *Light: Science & Applications*, vol. 6, no. 11, e17082–e17082, 2017.

[21] S. Yang, Z. Yang, K. Fischer, K. Zhong, J. Stadler, F. Godenschweger, J. Steiner, H.-J. Heinze, H.-G. Bernstein, B. Bogerts, *et al.*, "Integration of ultra-high field mri and histology for connectome based research of brain disorders," *Frontiers in neuroanatomy*, vol. 7, p. 31, 2013.

[22] K. Nieman, O. Gaemperli, P. Lancellotti, and S. Plein, *Advanced cardiac imaging*. Woodhead Publishing is an imprint of Elsevier, 2015.

[23] R. H. Silverman, "High-resolution ultrasound imaging of the eye–a review," *Clinical & experimental ophthalmology*, vol. 37, no. 1, pp. 54–67, 2009.

[24] S. Jeon, J. Kim, D. Lee, J. W. Baik, and C. Kim, "Review on practical photoacoustic microscopy," *Photoacoustics*, vol. 15, p. 100 141, 2019.

[25] L. Song, K. I. Maslov, K. K. Shung, and L. V. Wang, "Ultrasound-array-based real-time photoacoustic microscopy of human pulsatile dynamics in vivo," *Journal of biomedical optics*, vol. 15, no. 2, p. 021 303, 2010.

[26] L. Schermelleh, A. Ferrand, T. Huser, C. Eggeling, M. Sauer, O. Biehlmaier, and G. P. Drummen, "Super-resolution microscopy demystified," *Nature cell biology*, vol. 21, no. 1, pp. 72–84, 2019.

[27] E. Lin and A. Alessio, "What are the basic concepts of temporal, contrast, and spatial resolution in cardiac ct?" *Journal of cardiovascular computed tomography*, vol. 3, no. 6, pp. 403–408, 2009.

[28] F. Helmchen and W. Denk, "Deep tissue two-photon microscopy," *Nature methods*, vol. 2, no. 12, pp. 932–940, 2005.

[29] D. Kobat, N. G. Horton, and C. Xu, "In vivo two-photon microscopy to 1.6-mm depth in mouse cortex," *Journal of biomedical optics*, vol. 16, no. 10, p. 106 014, 2011.

[30] J. M. Schmitt, "Optical coherence tomography (oct): A review," *IEEE Journal of selected topics in quantum electronics*, vol. 5, no. 4, pp. 1205–1215, 1999.

[31] H.-C. Park, X. Zhang, W. Yuan, L. Zhou, H. Xie, and X. Li, "Ultralow-voltage electrothermal mems based fiber-optic scanning probe for forward-viewing endoscopic oct," *Optics letters*, vol. 44, no. 9, pp. 2232–2235, 2019.

[32] L. Wu and H. Xie, "A large vertical displacement electrothermal bimorph microactuator with very small lateral shift," *Sensors and Actuators A: Physical*, vol. 145, pp. 371–379, 2008.

[33] L. Liu, E. Wang, X. Zhang, W. Liang, X. Li, and H. Xie, "Mems-based 3d confocal scanning microendoscope using mems scanners for both lateral and axial scan," *Sensors and Actuators A: Physical*, vol. 215, pp. 89–95, 2014.

[34] F. Han, W. Wang, X. Zhang, and H. Xie, "Modeling and control of a large-stroke electrothermal mems mirror for fourier transform microspectrometers," *Journal of Microelectromechanical Systems*, vol. 25, no. 4, pp. 750–760, 2016.

[35] M. I. Younis, *MEMS linear and nonlinear statics and dynamics*. Springer Science & Business Media, 2011, vol. 20.

[36] H. Li, X. Duan, Z. Qiu, Q. Zhou, K. Kurabayashi, K. R. Oldham, and T. D. Wang, "Integrated monolithic 3d mems scanner for switchable real time vertical/horizontal cross-sectional imaging," *Optics express*, vol. 24, no. 3, pp. 2145–2155, 2016.

[37] H. Li, X. Duan, G. Li, K. R. Oldham, and T. D. Wang, "An electrostatic mems translational scanner with large out-of-plane stroke for remote axial-scanning in multi-photon microscopy," *Micromachines*, vol. 8, no. 5, p. 159, 2017.

[38] J. Curie and P. Curie, "Développement par compression de l'électricité polaire dans les cristaux hémièdres à faces inclinées," *Bulletin de minéralogie*, vol. 3, no. 4, pp. 90–93, 1880.

[39] G. Lippmann, "Principe de la conservation de l'électricité, ou second principe de la théorie des phénomènes électriques," *Journal de Physique Théorique et Appliquée*, vol. 10, no. 1, pp. 381–394, 1881.

[40] T. Naono, T. Fujii, M. Esashi, and S. Tanaka, "A large-scan-angle piezoelectric mems optical scanner actuated by a nb-doped pzt thin film," *Journal of Micromechanics and Microengineering*, vol. 24, no. 1, p. 015 010, 2013.

[41] J. Choi, Z. Qiu, C.-H. Rhee, T. Wang, and K. Oldham, "A three-degree-of-freedom thin-film pzt-actuated microactuator with large out-of-plane displacement," *Journal of Micromechanics and Microengineering*, vol. 24, no. 7, p. 075 017, 2014.

[42] X. Zhang, L. Zhou, and H. Xie, "A fast, large-stroke electrothermal mems mirror based on cu/w bimorph," *Micromachines*, vol. 6, no. 12, pp. 1876–1889, 2015.

[43] T. Mitsui, Y. Takahashi, and Y. Watanabe, "A 2-axis optical scanner driven nonresonantly by electromagnetic force for oct imaging," *Journal of Micromechanics and Microengineering*, vol. 16, no. 11, p. 2482, 2006.

[44] H. Zeng, M. Chiao, *et al.*, "Magnetically actuated mems microlens scanner for in vivo medical imaging," *Optics express*, vol. 15, no. 18, pp. 11 154–11 166, 2007.

[45] A. Dilipkumar, A. Al-Shemmary, L. Kreiß, K. Cvecek, B. Carlé, F. Knieling, J. Gonzales Menezes, O.-M. Thoma, M. Schmidt, M. F. Neurath, *et al.*, "Label-free multiphoton endomicroscopy for minimally invasive in vivo imaging," *Advanced Science*, vol. 6, no. 8, p. 1 801 735, 2019.

[46] A. Li, G. Hall, D. Chen, W. Liang, B. Ning, H. Guan, and X. Li, "A biopsy-needle compatible varifocal multiphoton rigid probe for depth-resolved optical biopsy," *Journal of biophotonics*, vol. 12, no. 1, e201800229, 2019.

[47] D. Y. Kim, K. Hwang, J. Ahn, Y.-H. Seo, J.-B. Kim, S. Lee, J.-H. Yoon, E. Kong, Y. Jeong, S. Jon, *et al.*, "Lissajous scanning two-photon endomicroscope for in vivo tissue imaging," *Scientific reports*, vol. 9, no. 1, pp. 1–8, 2019.

[48] W. Liang, H.-C. Park, K. Li, A. Li, D. Chen, H. Guan, Y. Yue, Y.-T. A. Gau, D. E. Bergles, M.-J. Li, *et al.*, "Throughput-speed product augmentation for scanning fiber-optic two-photon endomicroscopy," *IEEE Transactions on Medical Imaging*, 2020.

[49] X. Duan, H. Li, X. Li, K. R. Oldham, and T. D. Wang, "Axial beam scanning in multiphoton microscopy with mems-based actuator," *Optics express*, vol. 25, no. 3, pp. 2195–2205, 2017.

[50] J. A. Izatt, M. D. Kulkarni, H.-W. Wang, K. Kobayashi, and M. V. Sivak, "Optical coherence tomography and microscopy in gastrointestinal tissues," *IEEE Journal of Selected topics in quantum electronics*, vol. 2, no. 4, pp. 1017–1028, 1996.

[51] D. Kobat, M. E. Durst, N. Nishimura, A. W. Wong, C. B. Schaffer, and C. Xu, "Deep tissue multiphoton microscopy using longer wavelength excitation," *Optics express*, vol. 17, no. 16, pp. 13 354–13 364, 2009.

[52] X. Zhang, C. Duan, L. Liu, X. Li, and H. Xie, "A non-resonant fiber scanner based on an electrothermally-actuated mems stage," *Sensors and Actuators A: Physical*, vol. 233, pp. 239–245, 2015.

[53] A. Jain, H. Qu, S. Todd, and H. Xie, "A thermal bimorph micromirror with large bi-directional and vertical actuation," *Sensors and Actuators A: Physical*, vol. 122, no. 1, pp. 9–15, 2005.

[54] K. Jia, S. Pal, and H. Xie, "An electrothermal tip–tilt–piston micromirror based on folded dual s-shaped bimorphs," *Journal of Microelectromechanical systems*, vol. 18, no. 5, pp. 1004–1015, 2009.

[55] C. Guo and G. K. Fedder, "2-dof twisting electrothermal actuator for scanning laser rangefinder application," in *2011 IEEE 24th International Conference on Micro Electro Mechanical Systems*, IEEE, 2011, pp. 1205–1208.

[56] S. Timoshenko, "Analysis of bi-metal thermostats," *Josa*, vol. 11, no. 3, pp. 233–255, 1925.

[57] M. Birla, J. Zou, Z. Afkhami, X. Duan, H. Li, T. D. Wang, and K. R. Oldham, "Multi-photon 3d imaging with an electrothermal actuator with low thermal and inertial mass," *Sensors and Actuators A: Physical*, vol. 329, p. 112 791, 2021.

[58] X. Duan, H. Li, F. Wang, X. Li, K. R. Oldham, and T. D. Wang, "Three-dimensional side-view endomicroscope for tracking individual cells in vivo," *Biomedical optics express*, vol. 8, no. 12, pp. 5533–5545, 2017.

[59] S. M. Salapaka and M. V. Salapaka, "Scanning probe microscopy," *IEEE Control Systems Magazine*, vol. 28, no. 2, pp. 65–83, 2008.

[60] S.-H. Lee, J. J. Moon, and J. L. West, "Three-dimensional micropatterning of bioactive hydrogels via two-photon laser scanning photolithography for guided 3d cell migration," *Biomaterials*, vol. 29, no. 20, pp. 2962–2968, 2008.

[61] S. T. Holmström, U. Baran, and H. Urey, "Mems laser scanners: A review," *Journal of Microelectromechanical Systems*, vol. 23, no. 2, pp. 259–275, 2014.

[62] K. Hwang, Y.-H. Seo, J. Ahn, P. Kim, and K.-H. Jeong, "Frequency selection rule for high definition and high frame rate lissajous scanning," *Scientific reports*, vol. 7, no. 1, pp. 1–8, 2017.

[63] N. Ishikawa, K. Ikeda, and R. Sawada, "Temperature dependence of the scanning performance of an electrostatic microscanner," *Journal of Micromechanics and Microengineering*, vol. 26, no. 3, p. 035 002, 2016.

[64] E. Csencsics and G. Schitter, "Design of a phase-locked-loop-based control scheme for lissajous-trajectory scanning of fast steering mirrors," in *2017 American Control Conference (ACC)*, IEEE, 2017, pp. 1568–1573.

[65] S. Pannu, C. Chang, R. Muller, and A. Pisano, "Closed-loop feedback-control system for improved tracking in magnetically actuated micromirrors," in *2000 IEEE/LEOS International Conference on Optical MEMS (Cat. No. 00EX399)*, IEEE, 2000, pp. 107–108.

[66] E. Csencsics and G. Schitter, "System design and control of a resonant fast steering mirror for lissajous-based scanning," *IEEE/ASME Transactions on Mechatronics*, vol. 22, no. 5, pp. 1963–1972, 2017.

[67] J. Morrison, M. Imboden, and D. J. Bishop, "Tuning the resonance frequencies and mode shapes in a large range multi-degree of freedom micromirror," *Optics express*, vol. 25, no. 7, pp. 7895–7906, 2017.

[68] N. O. Loewke, Z. Qiu, M. J. Mandella, R. Ertsey, A. Loewke, L. A. Gunaydin, E. L. Rosenthal, C. H. Contag, and O. Solgaard, "Software-based phase control, video-rate imaging, and real-time mosaicing with a lissajous-scanned confocal microscope," *IEEE Transactions on Medical Imaging*, 2019.

[69] A. Santos, C. Ortiz de Solórzano, J. J. Vaquero, J. Pena, N. Malpica, and F. Del Pozo, "Evaluation of autofocus functions in molecular cytogenetic analysis," *Journal of microscopy*, vol. 188, no. 3, pp. 264–272, 1997.

[70] F. C. Groen, I. T. Young, and G. Ligthart, "A comparison of different focus functions for use in autofocus algorithms," *Cytometry: The Journal of the International Society for Analytical Cytology*, vol. 6, no. 2, pp. 81–91, 1985.

[71] M. L. Mendelsohn and B. H. Mayall, "Computer-oriented analysis of human chromosomes—iii. focus," *Computers in biology and medicine*, vol. 2, no. 2, pp. 137–150, 1972.

[72] W. Shahid, Z. Qiu, X. Duan, H. Li, T. D. Wang, and K. R. Oldham, "Modeling and simulation of a parametrically resonant micromirror with duty-cycled excitation," *Journal of Microelectromechanical Systems*, vol. 23, no. 6, pp. 1440–1453, 2014.

[73] H. Li, P. Barnes, E. Harding, X. Duan, T. D. Wang, and K. R. Oldham, "Large-displacement vertical electrostatic microactuator dynamics using duty-cycled softening/stiffening parametric resonance," *Journal of Microelectromechanical Systems*, vol. 28, no. 3, pp. 351–361, 2019.

[74] Y. Yao, B. Abidi, N. Doggaz, and M. Abidi, "Evaluation of sharpness measures and search algorithms for the auto-focusing of high-magnification images," in *Visual Information Processing XV*, International Society for Optics and Photonics, vol. 6246, 2006, 62460G.

[75] Y. Chen, M. Lee, M. B. Birla, H. Li, G. Li, X. Duan, T. D. Wang, and K. R. Oldham, "Motion estimation for a compact electrostatic microscanner via shared driving and sensing electrodes in endomicroscopy," *IEEE/ASME Transactions on Mechatronics*, vol. 25, no. 2, pp. 661–672, 2020.

[76] E. J. Botcherby, R. Juskaitis, M. J. Booth, and T. Wilson, "Aberration-free optical refocusing in high numerical aperture microscopy," *Optics letters*, vol. 32, no. 14, 2007.